REPORT DOCUMENTATION PAGE

Form Approved OMB NO. 0704-0188

The public reporting burden for this collection of information is estimated to average 1 hour per response, including the time for reviewing instructions, searching existing data sources, gathering and maintaining the data needed, and completing and reviewing the collection of information. Send comments regarding this burden estimate or any other aspect of this collection of information, including suggesstions for reducing this burden, to Washington Headquarters Services, Directorate for Information Operations and Reports, 1215 Jefferson Davis Highway, Suite 1204, Arlington VA, 22202-4302. Respondents should be aware that notwithstanding any other provision of law, no person shall be subject to any oenalty for failing to comply with a collection of information if it does not display a currently valid OMB control number.
PLEASE DO NOT RETURN YOUR FORM TO THE ABOVE ADDRESS.

1. REPORT DATE (DD-MM-YYYY)	2. REPORT TYPE	3. DATES COVERED (From - To)
21-09-2010	Final Report	1-Aug-2006 - 31-Jul-2009

4. TITLE AND SUBTITLE	5a. CONTRACT NUMBER
Dual Mode Thin Film Bulk Acoustic Resonators (FBARs) Based on AlN, ZnO and GaN Films with Tilted c-Axis Orientation	W911NF-06-1-0341
	5b. GRANT NUMBER
	5c. PROGRAM ELEMENT NUMBER
	611102

6. AUTHORS	5d. PROJECT NUMBER
Qing-Ming Wang	
	5e. TASK NUMBER
	5f. WORK UNIT NUMBER

7. PERFORMING ORGANIZATION NAMES AND ADDRESSES	8. PERFORMING ORGANIZATION REPORT NUMBER
University of Pittsburgh 123 University Place University Club Pittsburgh, PA 15213 -2303	

9. SPONSORING/MONITORING AGENCY NAME(S) AND ADDRESS(ES)	10. SPONSOR/MONITOR'S ACRONYM(S)
U.S. Army Research Office P.O. Box 12211 Research Triangle Park, NC 27709-2211	ARO
	11. SPONSOR/MONITOR'S REPORT NUMBER(S)
	49404-EG.3

12. DISTRIBUTION AVAILIBILITY STATEMENT

Approved for Public Release; Distribution Unlimited

13. SUPPLEMENTARY NOTES

The views, opinions and/or findings contained in this report are those of the author(s) and should not contrued as an official Department of the Army position, policy or decision, unless so designated by other documentation.

14. ABSTRACT

Thin film bulk acoustic wave resonators (FBAR) using piezoelectric AlN, ZnO and GaN thin films have attracted extensive research activities in the past years. Highly c-axis oriented (normal-plane orientation) binary semiconductor piezoelectric thin films are particularly investigated for resonators operating at the fundamental thickness longitudinal mode. Depending on the processing conditions, tilted polarization (c-axis off the normal direction to the substrate surface) is often found in the as-deposited piezoelectric thin films, which leads to the

15. SUBJECT TERMS

MEMS, acoustic wave devices, acoustic wave sensors

16. SECURITY CLASSIFICATION OF:			17. LIMITATION OF ABSTRACT	15. NUMBER OF PAGES	19a. NAME OF RESPONSIBLE PERSON
a. REPORT	b. ABSTRACT	c. THIS PAGE			Qing-Ming Wang
UU	UU	UU	UU		19b. TELEPHONE NUMBER
					412-624-4885

Standard Form 298 (Rev 8/98)
Prescribed by ANSI Std. Z39.18

Report Title

Dual Mode Thin Film Bulk Acoustic Resonators (FBARs) Based on AlN, ZnO and GaN Films with Tilted c-Axis Orientation

ABSTRACT

Thin film bulk acoustic wave resonators (FBAR) using piezoelectric AlN, ZnO and GaN thin films have attracted extensive research activities in the past years. Highly c-axis oriented (normal-plane orientation) binary semiconductor piezoelectric thin films are particularly investigated for resonators operating at the fundamental thickness longitudinal mode. Depending on the processing conditions, tilted polarization (c-axis off the normal direction to the substrate surface) is often found in the as-deposited piezoelectric thin films, which leads to the coexistence of thickness longitudinal mode and shear mode for the thin film resonators.

In this project, we intend to deposit AlN films with tilted polarization angles on Si substrate using a modified DC magnetron sputtering method. So far, AlN thin films with different tilted polarization angles have been achieved. High quality AlN thin films on other suitable single crystal substrate (such as sapphire) have also been deposited and characterized using a composite resonator approach. A theoretical model has been developed for composite thin film resonator, which can be applied to extract the electromechanical material properties of piezoelectric thin films. With AlN film deposited and patterned on sapphire substrate, a laser liftoff approach has been developed to transfer the thin film resonators to the receptor substrate (silicon) for ultimate on-chip integration.

We have also conducted analytical study of thin film bulk acoustic wave resonators (FBARs) using ZnO, AlN and GaN films with a c-axis tilt angle (off-normal) from 0 to 180 degree. The tilted c-axis orientation induces normal plane and in-plane polarizations, which leads to the coexistence of the longitudinal mode and shear mode in the resonator. Interestingly, it was found that for ZnO, AlN and GaN FBARs, special tilted angles were found for pseudo-shear and pseudo-longitudinal modes. This result opens new ways for FBARs design and fabrication.

List of papers submitted or published that acknowledge ARO support during this reporting period. List the papers, including journal references, in the following categories:

(a) Papers published in peer-reviewed journals (N/A for none)

1. Lifeng Qin, Qingming Chen, Hongbin Cheng, and Qing-Ming Wang "Analytical Study of Dual Mode Thin Film Bulk Acoustic Resonators (FBARs) Based on ZnO and AlN Films with Tilted c-Axis Orientation", IEEE Transactions on Ultrasonics, Ferroelectrics, and Frequency Control, vol. 57, no. 8, (2010)
2. Lifeng Qin, Qing-Ming Wang, "Analysis of dual-mode thin film bulk acoustic resonators (FBARs) based on polar c-axis tilted wurtzite gallium nitride", JOURNAL OF APPLIED PHYSICS, 107, 114102 (2010)
3. Lifeng Qin, Zijing Zeng, Hongbin Cheng, and Qing-Ming Wang, "Acoustic Wave Flow Sensor Using Quartz Thickness Shear Mode Resonator", IEEE Transactions on Ultrasonics, Ferroelectrics, and Frequency control, vol. 56, no. 9, pp. 1945-1954 (2009)
4. Zengtao Yang, Jiashi Yang, Yuantai Hu, Qing-Ming Wang, "Vibration Characteristics of a Circular Cylindrical Panel Piezoelectric Transducer", IEEE Transactions on Ultrasonics, Ferroelectrics, and Frequency control, vol. 55, no. 10, pp. 2327-2335 (2008)
5. Fang Li, James H.-C. Wang, Qing-Ming Wang, "Thickness Shear Mode Quartz Resonator Sensors for Characterizing Viscoelastic Properties of Cell Monolayer", Sensors & Actuators, B: Chemical, 128 (2008), pp.399-406
6. Fang Li, James H.-C. Wang, Qing-Ming Wang, "Thickness Shear Mode Quartz Resonator Sensors for Characterizing Viscoelastic Properties of Cell Monolayer", Sensors & Actuators, B: Chemical, 128 (2008), pp.399-406
7. Qingming Chen, Lifeng Qin, and Qing-Ming Wang, "Property characterization of AlN thin films in composite resonator structure", J. Appl. Phys. 101, 084103 (2007)
8. Huan Xue, Yuantai Hu, Qing-Ming Wang, and Jiashi Yang, "Analysis of Temperature Compensation in a Plate Thickness Mode Bulk Acoustic Wave Resonator", IEEE Transactions on Ultrasonics, Ferroelectrics, and Frequency control, 54 (9):1826-33 (2007)
9. Lifeng Qin, Hongbin Cheng, Jacob M. Li, Qing-Ming Wang, "Characterization of Polymer Nanocomposite Films Using Quartz Thickness Shear Mode (TSM) Acoustic Wave Sensor," Sensors and Actuators A: Physical, Volume 136, issue 1, pp. 111-117, 2007

Number of Papers published in peer-reviewed journals: 9.00

(b) Papers published in non-peer-reviewed journals or in conference proceedings (N/A for none)

Number of Papers published in non peer-reviewed journals: 0.00

(c) Presentations

1.Q.Wang, "Acoustic wave sensor research at the University of Pittsburgh", Peking University, June 29, 2010

2.Q.Wang, "High Temperature Piezoelectric Materials For Transducer Applications", 34rd International Conference and Exposition on Advanced Ceramics and Composites, Daytona, FL, January, 2010 (Invited)

3.Qing-Ming Wang, "Acoustic Wave Resonator Based Cell Sensor", Invited Seminar in Kunming University of Science and Technology, June 12, 2008

4.Qing-Ming Wang, Fang Li, James Wang: "Acoustic Wave Biosensors" Invited Seminar in Shanghai University, June 13, 2007

5.Fang Li, James H.-C. Wang, and Qing-Ming Wang, "Monitoring Cell Adhesion and Characterizing Cell Viscoelasticity by Using Thickness Shear Mode Acoustic Wave Sensors" The Fifth International Conference on Nonlinear Mechanics (ICNM-V), June 11-14, 2007, Shanghai

6.Qing-Ming Wang, "Integrated AlN Thin Film Bulk Acoustic Wave Resonator (FBAR)" Invited Seminar in Guilin University of Electronic Technology, June 6, 2007

7.Qing-Ming Wang, " Fabrication and Characterization of AlN Thin Film Bulk Acoustic Wave Resonator (FBAR)" Invited seminar in Tsinghua University, May 17, 2007

8.Qing-Ming Wang, " Fabrication and Characterization of AlN Thin Film Bulk Acoustic Wave Resonator (FBAR)" Invited seminar in Huazhong University of Science and Technology University, May 14, 2007

9.Qing-Ming Wang and Qingming Chen, "Property characterization of AlN thin films in composite resonator structure", 17TH US ARMY SYMPOSIUM ON SOLID MECHANICS, April 2-5, 2007, Renaissance Harborplace, 202 East Pratt Street, Baltimore, MD (Invited)

Number of Presentations: 9.00

Non Peer-Reviewed Conference Proceeding publications (other than abstracts):

Number of Non Peer-Reviewed Conference Proceeding publications (other than abstracts):   0

Peer-Reviewed Conference Proceeding publications (other than abstracts):

1.Dan Xiang, George Zhao and Fang Li, Qing-Ming Wang, "Self-Powered Wireless Acoustic Sensor System for Impact Detection and Evaluation", 56th International Instrumentation Symposium, Rochester, NY, 10-14 May 2010

2.Hongbin Cheng, Lifeng Qin, Qing-Ming Wang, "HIGH TEMPERATURE ACOUSTIC WAVE GAS SENSOR USING LANGASITE CRYSTAL RESONATOR" Proceeding of 34th International Conference on Advanced Ceramics & Composites (ICACC), Daytona, FL, January, 2010

3.Fang Li, James H.-C. Wang, and Qing-Ming Wang, "Monitoring Cell Adhesion and Characterizing Cell Viscoelasticity by Using Thickness Shear Mode (TSM) Resonate Sensor", Proceeding of the IEEE-2008 International Frequency Control Symposium, pp.360-365, Honolulu, Hawaii, USA May 18 - 21, 2008

4.Hongbin Cheng, Lifeng Qin, Fang Li, Qing-Ming Wang, "Ammonia Sensing Characteristics of Quartz Resonator Coated with ZnO Nanowires Sensitive Layer", Proceeding of the IEEE-2008 International Frequency Control Symposium, pp. 535-537, 2008

5.Qingming Chen, Fang Li, Hongbin Cheng, Qing-Ming Wang, "Characteristics of Dual Mode AlN Thin Film Bulk Acoustic Wave Resonators", Proceeding of the IEEE-2008 International Frequency Control Symposium, pp. 609-614, 2008

6.Hongbin cheng, Lifeng Qin, Qing-Ming Wang, "High temperature gas sensor using langasite acoustic wave resonator and nanostructured ZnO layer" Proceeding of the IEEE-2007International Ultrasonics Symposium, New York, New York, USA, October 28-31, 2007. pp. 1361-64

7.Fang Li, James. H.-C. Wang, Qing-mIng Wang, "Theoretical Analysis And Experimental Study Of Love Mode Surface Acoustic Wave Device As Cell-based Biosensor", Proceeding of the IEEE-2007International Ultrasonics Symposium, New York, New York, USA, October 28-31, 2007. pp. 2111-14

8.Fang Li, Qing-Ming Wang, and James H.-C. Wang, "An acoustic wave biosensor for probing the viscoelastic properties of living cells", Proceedings of SPIE -- Volume 6218, Chemical and Biological Sensing VII, Patrick J. Gardner, Augustus W. Fountain III, Editors, 62180N (May. 19, 2006)

9.Qingming Chen, Fang Li, Qing-Ming Wang, "Characterization of nanomechanical and piezoelectric properties of AlN thin film for thin film bulk acoustic wave resonators," Proc. SPIE Vol. 6223, 62230I, Micro (MEMS) and Nanotechnologies for Space Applications; Thomas George, Zhong-Yang Cheng; Eds. (May, 2006)

10.Fang Li, James H.-C. Wang and Qing-Ming Wang, "Thickness Shear Mode Resonator Biosensor to Monitor Extracellular Matrix (ECM) Produced by Fibroblasts in Culture" Proceedings of the 2006 IEEE International Frequency Control Symposium and Exposition, Miami, Florida, June 5-7, 2006. pp. 538-544

11.Qingming Chen, Qing-Ming Wang, "Characterization of Mechanical and Piezoelectric Properties of the AlN Thin Film in a Composite Resonator Structure", Proceedings of the 2006 IEEE International Frequency Control Symposium and Exposition, Miami, Florida, June 5-7, 2006. pp. 104-110

Number of Peer-Reviewed Conference Proceeding publications (other than abstracts):   11

(d) Manuscripts

1. Lifeng Qin and Qing-Ming Wang, "Mass sensitivity of thin film bulk acoustic resonator sensors based on polar c-axis tilted ZnO and AlN Thin Film" Accepted to JOURNAL OF APPLIED PHYSICS (2010)

Number of Manuscripts: 1.00

Patents Submitted

Patents Awarded

Graduate Students

NAME	PERCENT_SUPPORTED
Lifeng Qin	0.50
Fang Li	0.25
Qingming Chen	0.25
FTE Equivalent:	**1.00**
Total Number:	**3**

Names of Post Doctorates

NAME	PERCENT_SUPPORTED
Chengliang Sun	0.25
FTE Equivalent:	**0.25**
Total Number:	**1**

Names of Faculty Supported

NAME	PERCENT_SUPPORTED	National Academy Member
Qing-Ming Wang	0.10	No
FTE Equivalent:	**0.10**	
Total Number:	**1**	

Names of Under Graduate students supported

NAME	PERCENT_SUPPORTED
FTE Equivalent:	
Total Number:	

Student Metrics

This section only applies to graduating undergraduates supported by this agreement in this reporting period

The number of undergraduates funded by this agreement who graduated during this period: 0.00

The number of undergraduates funded by this agreement who graduated during this period with a degree in science, mathematics, engineering, or technology fields: 0.00

The number of undergraduates funded by your agreement who graduated during this period and will continue to pursue a graduate or Ph.D. degree in science, mathematics, engineering, or technology fields: 0.00

Number of graduating undergraduates who achieved a 3.5 GPA to 4.0 (4.0 max scale): 0.00

Number of graduating undergraduates funded by a DoD funded Center of Excellence grant for Education, Research and Engineering: 0.00

The number of undergraduates funded by your agreement who graduated during this period and intend to work for the Department of Defense 0.00

The number of undergraduates funded by your agreement who graduated during this period and will receive scholarships or fellowships for further studies in science, mathematics, engineering or technology fields: 0.00

Names of Personnel receiving masters degrees

NAME

Total Number:

Names of personnel receiving PHDs

NAME
Fang Li
Qingming Chen
Lifeng Qin

Total Number: 3

Names of other research staff

NAME   PERCENT SUPPORTED

FTE Equivalent:
Total Number:

Sub Contractors (DD882)

Inventions (DD882)

<u>Project Final Report</u>

Title: Integrated Multimode Thin Film Bulk Acoustic wave Resonators

(Project No. # 49404-EG)

Project Start Date: August 1, 2006
Final Report Date: September 21, 2010

Qing-Ming Wang, PhD
Associate Professor and William Kepler Whiteford Faculty Fellow
Department of Mechanical Engineering and Materials Science
University of Pittsburgh, Pittsburgh, PA 15261

1. Foreword

Thin film bulk acoustic wave resonators (FBAR) using piezoelectric AlN, ZnO and GaN thin films have attracted extensive research activities in the past years. Highly c-axis oriented (normal-plane orientation) binary semiconductor piezoelectric thin films are particularly investigated for resonators operating at the fundamental thickness longitudinal mode. Depending on the processing conditions, tilted polarization (c-axis off the normal direction to the substrate surface) is often found in the as-deposited piezoelectric thin films, which leads to the coexistence of thickness longitudinal mode and shear mode for the thin film resonators.

In this project, we intend to deposit AlN films with tilted polarization angles on Si substrate using a modified DC magnetron sputtering method. So far, AlN thin films with different tilted polarization angles have been achieved. High quality AlN thin films on other suitable single crystal substrate (such as sapphire) have also been deposited and characterized using a composite resonator approach. A theoretical model has been developed for composite thin film resonator, which can be applied to extract the electromechanical material properties of piezoelectric thin films. With AlN film deposited and patterned on sapphire substrate, a laser liftoff approach has been developed to transfer the thin film resonators to the receptor substrate (silicon) for ultimate on-chip integration.

We have also conducted analytical study of thin film bulk acoustic wave resonators (FBARs) using ZnO, AlN and GaN films with a c-axis tilt angle (off-normal) from 0^0 to 180^0. The tilted c-axis orientation induces normal plane and in-plane polarizations, which leads to the coexistence of the longitudinal mode and shear mode in the resonator. The equation for predicting electric impedance of FBARs was derived from the basic piezoelectric constitutive equations. Material properties including elastic, dielectric and piezoelectric coefficients, bulk wave properties including acoustic velocity and electromechanical coupling coefficient, and impedance of FBARs were calculated and showed strong dependence on the tilt angle. Interestingly, it was found that for ZnO FBAR, pure thickness longitudinal modes occur at 0^0 and 65.4^0, and pure thickness shear modes occur at 43^0 and 90^0. For AlN FBAR, pure longitudinal modes occur at 0^0 and 67.1^0, and pure shear modes occur at 46.1^0 and 90^0 for AlN. In other words, pure thickness longitudinal and shear modes exist in ZnO and AlN FBAR at specific tilted polarization angles. In addition, two peaks of shear mode electromechanical coefficient are found at 33.3^0 and 90^0 for ZnO, and

34.5^0 and 90^0 for AlN. Therefore, ZnO and AlN films with specific tilt angles may provide options in the design and fabrication of FBARs, considering their strong shear resonance with high electromechanical coefficients. The use of dual mode FBARs for mass sensor is also analyzed, the calculated large resonant frequency shift due to mass loading shows their good promising in sensor application with high sensitivity. The simulation results agreed well with the reported experiment results, and can be used for design and application of FBARs. GaN thin film with tilted polarization has also been considered for FBARs in this work. Similar results have been obtained, indicating that GaN is also a promising material for FBARs and sensor applications.

2. Table of Contents

    a. **Manuscript:** Lifeng Qin and Qing-Ming Wang, "Mass sensitivity of thin film bulk acoustic resonator sensors based on polar c-axis tilted ZnO and AlN Thin Film" Accepted to JOURNAL OF APPLIED PHYSICS (2010)

    b. Lifeng Qin, Qing-Ming Wang, "Analysis of dual-mode thin film bulk acoustic resonators (FBARs) based on polar c-axis tilted wurtzite gallium nitride", JOURNAL OF APPLIED PHYSICS, 107, 114102 (2010)

    c. Lifeng Qin, Qingming Chen, Hongbin Cheng, and Qing-Ming Wang "Analytical Study of Dual Mode Thin Film Bulk Acoustic Resonators (FBARs) Based on ZnO and AlN Films with Tilted c-Axis Orientation", IEEE Transactions on Ultrasonics, Ferroelectrics, and Frequency Control, vol. 57, no. 8, (2010)

    d. Lifeng Qin, Zijing Zeng, Hongbin Cheng, and Qing-Ming Wang, "Acoustic Wave Flow Sensor Using Quartz Thickness Shear Mode Resonator", IEEE Transactions on Ultrasonics, Ferroelectrics, and Frequency control, vol. 56, no. 9, pp. 1945-1954 (2009)

    e. Zengtao Yang, Jiashi Yang, Yuantai Hu, Qing-Ming Wang, "Vibration Characteristics of a Circular Cylindrical Panel Piezoelectric Transducer", IEEE Transactions on Ultrasonics, Ferroelectrics, and Frequency control, vol. 55, no. 10, pp. 2327-2335 (2008)

    f. Qingming Chen, Lifeng Qin, and Qing-Ming Wang, "Property characterization of AlN thin films in composite resonator structure", J. Appl. Phys. 101, 084103 (2007)

    g. Huan Xue, Yuantai Hu, Qing-Ming Wang, and Jiashi Yang, "Analysis of Temperature Compensation in a Plate Thickness Mode Bulk Acoustic Wave Resonator", IEEE Transactions on Ultrasonics, Ferroelectrics, and Frequency control, 54 (9):1826-33 (2007)

1) Statement of the problem studied

Development of advanced wireless communication technology has led to an explosive growth of emerging military and consumer applications of RF, microwave, and millimeter wave devices, circuits and systems. Handheld communication systems with desirable frequency control performance are highly desirable for US Army. Future personal and ground communication systems as well as communication satellites for US Army necessitate the use of miniaturized on-chip thin film resonators and filters, featuring small size, low weight, high performance and low cost, for precise frequency control applications. However, On-chip fabrication and integration of thin film RF microelectromechanical resonators has been recognized as a technological challenge in the current microelectronics and MEMS development. The currently used frequency control devices such as surface acoustic wave (SAW) and bulk acoustic wave (BAW) resonators or filters are in general off-chip devices with considerably large sizes. Thin film bulk acoustic wave resonators using piezoelectric AlN thin films have attracted extensive research activities in the past few years but with limited success. This is largely due to the processing difficulties in the direct deposition and integration of high quality thin films on Si substrate. So far, thin film resonators studied are usually composed of materials fabricated by methods that do not result in desirable crystal forms and orientations. Consequently the materials do not necessarily have properties that closely resemble bulk materials in magnitude or stability. The objectives of this project include: 1) fabrication of AlN thin film with tilted polarization (polarization direction off the normal of the thin film thickness direction) to enable the realization of dual mode thin film bulk acoustic wave resonators (FBARs); 3) theoretical and experimental studies of dual mode piezoelectric thin film resonators; 3) development of an on-chip integration technology of that can ultimately overcome the technological bottleneck in the miniaturization and integration of RF resonators and filters; 4) explore the use of FBARs for sensor applications.

2) Summary of the most important results

The novel dual mode thin film resonators we proposed to develop and studied in the past few years in this project are based on the deposition of AlN films with tilted polarizations, or various different film orientations, which may lead to a great opportunity for the design of high performance frequency control devices. Therefore, this project, targeting at the fundamental issues on the deposition of high quality AlN thin films with different orientations, and the fabrication and onchip integration of multimode thin film bulk acoustic wave resonators, intends to investigate a novel approach to facilitate the development of high performance onchip frequency control devices.

In the first half phase of this project, we intended to deposit AlN films with tilted polarization angles on Si substrate using a modified DC magnetron sputtering method. Through this ARO funding, AlN thin films with different tilted polarization angles have been achieved. High quality AlN thin films on other suitable single crystal substrate (such as sapphire) have also been deposited and characterized using a composite resonator approach. A theoretical model has been developed for composite thin film resonator, which can be applied to extract the electromechanical material properties of piezoelectric thin films. With AlN film deposited and patterned on sapphire substrate, a laser liftoff approach has been developed to transfer the thin

film resonators to the receptor substrate (silicon) for ultimate on-chip integration. More specifically, we have performed the following research tasks:

− Deposition of piezoelectric AlN films with various orientations on silicon and sapphire substrate by DC magnetron sputtering and MOCVD.
− Use of SEM and XRD to characterize the structural characteristics of the as-deposited films.
− Characterization of nanomechanical properties of the thin film materials
− Modeling of the electric impedance of three layer and four layer thin film composite resonators
− Development of application of a spectrum method for the modeling and characterization of composite thin film resonators
− Use of Laser interferometer technique to characterize the piezoelectric property of the AlN thin films
− Sacrificial layer GaN was used between the AlN thin film and the sapphire substrate to assist excimer laser liftoff and transfer of the thin film devices from sapphire substrate to receptor substrate (Si); and ultimate onchip integration of thin film resonators has been successfully demonstrated
− Characterization of frequency-temperature stability of thin film resonators

In the second phase of this project, we have conducted analytical study of thin film bulk acoustic wave resonators (FBARs) using ZnO, AlN and GaN films with a c-axis tilt angle (off-normal) from 0^0 to 180^0. The tilted c-axis orientation induces normal plane and in-plane polarizations, which leads to the coexistence of the longitudinal mode and shear mode in the resonator. The equation for predicting electric impedance of FBARs was derived from the basic piezoelectric constitutive equations. Material properties including elastic, dielectric and piezoelectric coefficients, bulk wave properties including acoustic velocity and electromechanical coupling coefficient, and impedance of FBARs were calculated and showed strong dependence on the tilt angle. Interestingly, it was found that for ZnO FBAR, pure thickness longitudinal modes occur at 0^0 and 65.4^0, and pure thickness shear modes occur at 43^0 and 90^0. For AlN FBAR, pure longitudinal modes occur at 0^0 and 67.1^0, and pure shear modes occur at 46.1^0 and 90^0 for AlN. In other words, pure thickness longitudinal and shear modes exist in ZnO and AlN FBAR at specific tilted polarization angles. In addition, two peaks of shear mode electromechanical coefficient are found at 33.3^0 and 90^0 for ZnO, and 34.5^0 and 90^0 for AlN. Therefore, ZnO and AlN films with specific tilt angles may provide options in the design and fabrication of FBARs, considering their strong shear resonance with high electromechanical coefficients. The use of dual mode FBARs for mass sensor is also analyzed; the calculated large resonant frequency shift due to mass loading shows their good promising in sensor application with high sensitivity. The simulation results agreed well with the reported experiment results, and can be used for design and application of FBARs. GaN thin film with tilted polarization has also been considered for FBARs in this work. Similar results have been obtained, indicating that GaN is also a promising material for FBARs and sensor applications.

Mass sensitivity of thin film bulk acoustic resonator sensors based on polar c-axis tilted ZnO and AlN Thin Film

Lifeng Qin and Qing-Ming Wang [a)]

Department of Mechanical Engineering and Materials Science, University of Pittsburgh, Pittsburgh, PA

15261, USA

The mass sensitivity of thin film bulk acoustic wave resonators (FBARs) using ZnO and AlN thin films with tilted polar c-axis has been theoretically investigated. The tilted c-axis orientation induces normal plane and in-plane polarizations, which leads to the coexistence of thickness longitudinal mode and thickness shear mode in the resonators. The equation for predicting electric impedance of FBARs with a mass loading layer was derived from the basic piezoelectric constitutive equations. The mass sensitivity of ZnO and AlN dual mode resonators was found by calculating the resonant frequency shifts of the thickness shear mode and thickness longitudinal mode due to thin film mass loading. In the calculation, ZnO and AlN thin film has a c-axis tilt angle from 0^0-90^0, 2μm thickness and 300μm by 300μm electrode area; four different materials (Al, SiO_2, Au and Pt) were considered as the thin film mass loading. It was found that both longitudinal resonance frequency and shear resonance frequency for different c-axis angle have a significant shift due to the mass loading; the mass sensitivities, defined as $\Delta f/(f\Delta m)$, of the longitudinal and shear mode for this four mass loading materials are very close, and do not change much with c-axis tile angle with a value rang around -900 cm^2/g for ZnO FBARs and -1550 cm^2/g for AlN FBARs. The results are applicable for design and application of ZnO or AlN FBARs.

KEYWORDS: tilted c-axis; thin film bulk acoustic resonator; acoustic wave sensor; mass sensitivity.

I. INTRODUCTION

Due to its high sensitivity, simple structure, and easy interconnection with electronic measurement systems, bulk acoustic wave (BAW) resonators have been studied for mummeries sensing applications in physical and chemical processes.[1] Meanwhile, with the improvement of device fabrication and material growth techniques, now the resonator can be made with very small size. Especially thin film bulk acoustic wave resonators (FBARs) based on ZnO and AlN can be achieved with thickness from several micrometers down to tenth of micrometers. It is well known that the resonant frequency is inversely proportional to the resonator thickness; hence, the resonant frequencies of this kind resonators can be very high, which usually has a range from hundreds of MHz to tens GHz. Commonly, a BAW resonator consists of one piezoelectric layer with two electrodes deposited on both sides. For mass sensor application, special material sensitive to target is coated on the resonator surface. Surface change due to physical/chemical adsorption and absorption will induce resonant frequency shift, and the absolute frequency shift is proportion to the square of the operating frequency (resonant frequency).[2, 3] In other words, the higher sensor sensitivity can be accomplished by increasing the resonator's resonant frequency. Therefore, adopting FBAR structures for mass sensor application, can greatly improve the sensor sensitivity considering their high resonant frequency. In fact, FBARs have been experimentally investigated as gas sensors for H_2, CO and ethanol,[4] chemical sensors for metal ion Hg+ detection in liquid environment,[5] and biosensors for DNA and protein molecules,[6, 7] which showed much higher sensitivity than quartz microbalance (QCM).

It should be noticed that ZnO and AlN thin film used for FBAR fabrication are usually with normal-plane *c*-axis orientation, which makes FBARs operated in thickness longitudinal mode. For sensor application in liquid, acoustic wave energy of longitudinal mode is radiated into liquid through compressional motion, inducing significant damping of resonators; while the damping of shear mode acoustic wave is not severe. Hence, FBARs operated in shear mode is very promising for liquid

application. Fortunately, it has shown that thickness shear mode can be excited besides longitudinal mode when AlN and ZnO thin films has a tilted c-axis orientation .[8-13]

However, the theoretical analysis of resonator based on c-axis tilted ZnO and AlN is less. To our knowledge, there has not been a throughout study on mass sensitivity of dual mode FBARs based on c-axis tilted ZnO and AlN. For this purpose, we derived the electric impedance expression of c-axis tilted ZnO and AlN FBARs with a mass loading layer by the basic piezoelectric equations, and examine the resonant frequency shift of longitudinal and shear mode for different mass loading; further the mass sensitivity of dual mode resonators will be calculated and discussed.

II. Theory

A. Dual mode ZnO and AlN FBARs with a mass loading layer

Fig. 1(a) shows schematic of normal c-axis ZnO or AlN FBARs with a mass loading layer, and (x_1, x_2, x_3) is the original material coordinate; Fig. 1(b) shows the schematic of c-axis tilted ZnO and AlN FBARs with a mass loading layer. Compared with piezoelectric layer and mass loading layer, the acoustic impedance of electrodes is very small, hence for simplifying the problem, the two electrodes are ignored. A rectangular Cartesian coordinate system $(x_1^{'}, x_2^{'}, x_3^{'})$ is chosen with top electrode on $x_3^{'} = h$ and bottom electrode on $x_3^{'} = 0$. ZnO or AlN thin film has a tilt angle θ with $x_3^{'}$ direction. As shown in Fig. 1(c), $(x_1^{'}, x_2^{'}, x_3^{'})$ can be treated as the result of rotation of (x_1, x_2, x_3) about x_2 with an angle θ. For the characterization of c-axis tilted ZnO and AlN FBARs, the material properties (dielectric permittivity, piezoelectric stress coefficient, elastic stiffness) or $(\varepsilon^{'}, e^{'}, c^{'})$ in $(x_1^{'}, x_2^{'}, x_3^{'})$, need to be known, and they can be computed through corresponding value (ε, e, c) in original coordinate system (x_1, x_2, x_3) with the aids of matrix algebra[14]:

$$\varepsilon^{'} = a\varepsilon a^{t}, \; e^{'} = aeM^{t}, \; c^{'} = McM^{t} \tag{1a}$$

3

$$a = \begin{bmatrix} a_{11} & a_{12} & a_{13} \\ a_{21} & a_{22} & a_{23} \\ a_{31} & a_{32} & a_{33} \end{bmatrix} = \begin{bmatrix} \cos(\theta) & 0 & \sin(\theta) \\ 0 & 1 & 0 \\ -\sin(\theta) & 0 & \cos(\theta) \end{bmatrix} \tag{1b}$$

$$M = \begin{bmatrix} a_{11}^2 & a_{12}^2 & a_{13}^2 & 2a_{12}a_{13} & 2a_{11}a_{13} & 2a_{11}a_{12} \\ a_{21}^2 & a_{22}^2 & a_{23}^2 & 2a_{22}a_{23} & 2a_{21}a_{23} & 2a_{21}a_{22} \\ a_{31}^2 & a_{32}^2 & a_{33}^2 & 2a_{32}a_{33} & 2a_{31}a_{33} & 2a_{31}a_{32} \\ a_{21}a_{31} & a_{22}a_{32} & a_{23}a_{33} & a_{22}a_{33} + a_{23}a_{32} & a_{21}a_{33} + a_{23}a_{31} & a_{21}a_{32} + a_{22}a_{31} \\ a_{11}a_{31} & a_{12}a_{32} & a_{13}a_{33} & a_{12}a_{33} + a_{13}a_{32} & a_{11}a_{33} + a_{13}a_{31} & a_{11}a_{32} + a_{12}a_{31} \\ a_{11}a_{21} & a_{12}a_{22} & a_{13}a_{23} & a_{12}a_{23} + a_{13}a_{22} & a_{11}a_{23} + a_{13}a_{21} & a_{11}a_{22} + a_{12}a_{21} \end{bmatrix} \tag{1c}$$

where θ is the tilt angle, a^t is the transpose of a, and M^t is the transpose of M.

B. Impedance equation of *c*-axis tilted ZnO and AlN FBARs with a mass loading layer

Following a similar procedure[15], the impedance equation for *c*-axis tilted ZnO and AlN FBARs with a mass loading layer is derived. In the coordinate system (x_1', x_2', x_3'), we have the following acoustic field equations and piezoelectric constitution equations[14]:

$$\frac{\partial T_1}{\partial x_1'} + \frac{\partial T_6}{\partial x_2'} + \frac{\partial T_5}{\partial x_3'} = \rho \frac{\partial^2 u_1}{\partial t^2}$$

$$\frac{\partial T_6}{\partial x_1'} + \frac{\partial T_2}{\partial x_2'} + \frac{\partial T_4}{\partial x_3'} = \rho \frac{\partial^2 u_2}{\partial t^2} \tag{2}$$

$$\frac{\partial T_5}{\partial x_1'} + \frac{\partial T_4}{\partial x_2'} + \frac{\partial T_3}{\partial x_3'} = \rho \frac{\partial^2 u_3}{\partial t^2}$$

$$S_1 = \frac{\partial u_1}{\partial x_1'}, S_2 = \frac{\partial u_2}{\partial x_2'}, S_3 = \frac{\partial u_3}{\partial x_3'}$$

$$S_4 = \frac{\partial u_3}{\partial x_2'} + \frac{\partial u_2}{\partial x_3'}$$

$$S_5 = \frac{\partial u_3}{\partial x_1'} + \frac{\partial u_1}{\partial x_3'} \tag{3}$$

$$S_6 = \frac{\partial u_2}{\partial x_1'} + \frac{\partial u_1}{\partial x_2'}$$

$$T_p = c_{pq}^{E}{}' S_q - e_{kp}' E_k \tag{4}$$

$$D_i = e'_{iq}S_q + \varepsilon^{S'}_{ik}E_k \tag{5}$$

where T_p, S_q, D_i and E_k are the components of stress, strain, electric displacement and electric field intensity, $c^{E'}_{pq}$ are the elastic stiffness constants under constant electric field intensity, e'_{kp} are the piezoelectric stress constants, $\varepsilon^{S'}_{ik}$ are the permittivity constants under constant strain, and u_i is the displacement in the direction of x'_i ($i, k = 1, 2, 3$ and $p, q = 1, 2, 3, 4, 5, 6$). The resonator vibration can be treated as one dimension problem considering its high ratio of lateral dimensions to thickness of resonator. Hence, we can assume:

$$\begin{aligned}
&\frac{\partial T_i}{\partial x'_1} = \frac{\partial T_i}{\partial x'_2} = 0 \\
&E_1 = E_2 = 0, E_3 \neq 0 \\
&\frac{\partial D_3}{\partial x'_3} = 0
\end{aligned} \tag{6}$$

For a sinusoidal excitation, the voltage V and current I across FBAR are expressed by

$$\begin{aligned}
&V = \int_0^h E_3 dx'_3 \\
&I = j\omega A D_3
\end{aligned} \tag{7}$$

where A is the area of the electrodes, ω is the angle frequency. For traction forces at the boundary ($x'_3 = 0, h$) we have:

$$T_5(0) = T_3(0) = 0 \tag{8a}$$

$$\begin{bmatrix} T_5(h) \\ T_3(h) \end{bmatrix} = \begin{bmatrix} -j\omega Z^S_{ml} & 0 \\ 0 & -j\omega Z^L_{ml} \end{bmatrix} \begin{bmatrix} u_1(h) \\ u_3(h) \end{bmatrix} \tag{8b}$$

Z_{ml}^L and Z_{ml}^S are the longitudinal and shear acoustic impedance of mass loading layer, which can be

expressed by

$$Z_{ml}^L = j\rho_{ml} v_{ml}^L \tan(\gamma_{ml}^L), Z_{ml}^S = j\rho_{ml} v_{ml}^S \tan(\gamma_{ml}^S) \tag{9a}$$

$$v_{ml}^L = \sqrt{\frac{c_{ml}^{33}}{\rho_{ml}}}, v_{ml}^S = \sqrt{\frac{c_{ml}^{55}}{\rho_{ml}}}, \gamma_{ml}^L = \frac{\omega v_{ml}^L}{l_{ml}}, \gamma_{ml}^S = \frac{\omega v_{ml}^S}{l_{ml}} \tag{9b}$$

where v_{ml}^L and v_{ml}^S are longitudinal and shear acoustic velocity of mass loading layer; γ_{ml}^L and γ_{ml}^s are

longitudinal and shear phase delay in mass loading layer; ρ_{ml} and l_{ml} are the density and thickness of

mass loading layer; c_{ml}^{33} and c_{ml}^{55} are the elastic constants of mass loading layer. Here, we assume the mass

loading layer is isotropic.

For any θ, It is found:

$$c_{34}^{E'} = c_{45}^{E'} = e_{34}' = 0 \tag{10}$$

From (1) to (10), the impedance of FBAR can be solved:

$$Z = \frac{1}{j\omega C_0} (1 - (k^L)^2 p^L \frac{\tan(\gamma_L/2)}{\gamma_L/2} - (k^S)^2 p^S \frac{\tan(\gamma_S/2)}{\gamma_S/2}) \tag{11a}$$

Where

$$C_0 = \frac{\varepsilon_{33}^{S'} A}{h} \tag{11b}$$

$$\gamma_L = \frac{\omega h}{v^{(L)}}, \ \gamma_S = \frac{\omega h}{v^{(S)}} \tag{11c}$$

$$v^{(L)} = \left[\frac{\overline{c_{33}^{E'}} + \overline{c_{55}^{E'}}}{2\rho} + \sqrt{\left(\frac{\overline{c_{33}^{E'}} - \overline{c_{55}^{E'}}}{2\rho}\right)^2 + \left(\frac{\overline{c_{35}^{E'}}}{\rho}\right)^2} \right]^{1/2} \tag{11d}$$

$$v^{(S)} = \left[\frac{\overline{c_{33}^{E'}} + \overline{c_{55}^{E'}}}{2\rho} - \sqrt{\left(\frac{\overline{c_{33}^{E'}} - \overline{c_{55}^{E'}}}{2\rho}\right)^2 + \left(\frac{\overline{c_{35}^{E'}}}{\rho}\right)^2} \right]^{1/2} \tag{11e}$$

$$\overline{c_{33}^{E'}} = c_{33}^{E'} + \frac{\left(e_{33}^{'}\right)^2}{\varepsilon_{33}^{S'}}, \quad \overline{c_{35}^{E'}} = c_{35}^{E'} + \frac{e_{33}^{'}e_{35}^{'}}{\varepsilon_{33}^{S'}}, \quad \overline{c_{55}^{E'}} = c_{55}^{E'} + \frac{\left(e_{35}^{'}\right)^2}{\varepsilon_{33}^{S'}} \tag{11f}$$

$$(k^L)^2 = \frac{(e_L)^2}{\varepsilon_{33}^{S'}\rho(v^L)^2}, \quad (k^S)^2 = \frac{(e_S)^2}{\varepsilon_{33}^{S'}\rho(v^S)^2} \tag{11g}$$

$$\begin{aligned} e_L &= e_{35}^{'}\sin(\alpha) + e_{33}^{'}\cos(\alpha) \\ e_S &= e_{35}^{'}\cos(\alpha) - e_{33}^{'}\sin(\alpha) \end{aligned} \tag{11h}$$

$$\alpha = \frac{1}{2}\arctan\left(\frac{2\overline{c_{35}^{E'}}}{\overline{c_{33}^{E'}} - \overline{c_{55}^{E'}}}\right) \tag{11i}$$

$$p^L = 1 + \frac{\left[e_L\sin^2(\frac{\gamma^L}{2})(\frac{Z_{ml}^L Z_{ml}^S}{Z_L Z_S}\cos(\gamma^s) + j\frac{Z_{ml}^{LL}}{Z_L}\sin(\gamma^S)) + je_S\sin^2(\frac{\gamma^S}{2})\frac{Z_{ml}^{SL}}{Z_S}\sin(\gamma^L)\right]}{e_L \times \left(\begin{array}{l} \frac{Z_{ml}^L Z_{ml}^S}{Z_L Z_S}\cos(\gamma^L)\cos(\gamma^S) - \sin(\gamma^L)\sin(\gamma^S) + \\ j\left(\frac{Z_{ml}^{LL}}{Z_L}\cos(\gamma^L)\sin(\gamma^S) + \frac{Z_{ml}^{SS}}{Z_S}\sin(\gamma^L)\cos(\gamma^S)\right) \end{array}\right)}$$

$$p^S = 1 + \frac{\left[e_S\sin^2(\frac{\gamma^S}{2})(\frac{Z_{ml}^L Z_{ml}^S}{Z_L Z_S}\cos(\gamma^L) + j\frac{Z_{ml}^{SS}}{Z_S}\sin(\gamma^L)) + je_L\sin^2(\frac{\gamma^L}{2})\frac{Z_{ml}^{SL}}{Z_L}\sin(\gamma^S)\right]}{e_S \times \left(\begin{array}{l} \frac{Z_{ml}^L Z_{ml}^S}{Z_L Z_S}\cos(\gamma^L)\cos(\gamma^S) - \sin(\gamma^L)\sin(\gamma^S) + \\ j\left(\frac{Z_{ml}^{LL}}{Z_L}\cos(\gamma^L)\sin(\gamma^S) + \frac{Z_{ml}^{SS}}{Z_S}\sin(\gamma^L)\cos(\gamma^S)\right) \end{array}\right)} \tag{11j}$$

$$\begin{aligned} Z_L &= \rho v^{(L)}, \ Z_S = \rho v^{(S)} \\ Z_{ml}^{LL} &= Z_{ml}^L\cos^2(\alpha) + Z_{ml}^S\sin^2(\alpha) \\ Z_{ml}^{SS} &= Z_{ml}^S\cos^2(\alpha) + Z_{ml}^L\sin^2(\alpha) \\ Z_{ml}^{SL} &= (Z_{ml}^S - Z_{ml}^L)\sin(\alpha)\cos(\alpha) \end{aligned} \tag{11k}$$

Here, f is frequency, $v^{(L)}$ and $v^{(S)}$ are the acoustic velocities for longitudinal mode and shear mode, k_L^2 and k_S^2 are defined as the electromechanical coupling coefficient of longitudinal and shear mode, respectively.

III. RESULTS AND DISCUSSION

A. Material properties of c-axis tilted ZnO and AlN

Based on Eq. (1) and material property values of ZnO[16,17] and AlN[18] in (x_1, x_2, x_3) shown in Fig 1(d) and (e), the material properties of c-axis tilted ZnO and AlN in ($x_1^{'}$, $x_2^{'}$, $x_3^{'}$) can been calculated. Fig. 2 and 3 shows the nonzero components of elastic constants $c^{E'}$ and $c^{D'}$, where $c^{E'}$ is the elastic stiffness constant under constant electric field intensity, and $c^{D'}$ is the elastic stiffness constant under constant electric displacement. For $0^0 \leq \theta \leq 180^0$, both $c^{E'}$ and $c^{D'}$ are found to be symmetric as 6x6 matrixes with

$$c_{14}^{E'} = c_{24}^{E'} = c_{34}^{E'} = c_{16}^{E'} = c_{26}^{E'} = c_{36}^{E'} = c_{56}^{E'} = c_{45}^{E'} = 0 \text{ and } c_{14}^{D'} = c_{24}^{D'} = c_{34}^{D'} = c_{16}^{D'} = c_{26}^{D'} = c_{36}^{D'} = c_{56}^{D'} = c_{45}^{D'} = 0 .$$

As shown in Fig. 2 and 3, the most nonzero elastic constants are strongly dependant on the tilt angle. However $c_{22}^{E'}$ and $c_{22}^{D'}$ do not change with the tilt angle, which is due to the fact that x_2 and $x_2^{'}$ are the same axis.

Fig. 4 and 5 plot the nonzero components of dielectric constant under constant strain ($\varepsilon^{S'}$) and dielectric constant under constant stress ($\varepsilon^{T'}$), which both keep symmetric as 3 x 3 matrixes when θ changes from 0^0 to 180^0. As same as dielectric constants, $\varepsilon_{22}^{S'}$ and $\varepsilon_{22}^{T'}$ keep constant because $x_2^{'}$ does not change with θ; the other dielectric constants show great dependency on c-axis tilt angle. For example, the change of $\varepsilon_{11}^{S'}$ or $\varepsilon_{11}^{T'}$ with θ has an opposite trend with $\varepsilon_{33}^{S'}$ or $\varepsilon_{33}^{T'}$; at $\theta=90^0$ $\varepsilon_{11}^{S'}$ or $\varepsilon_{11}^{T'}$ has a maximum value ,and $\varepsilon_{33}^{S'}$ or $\varepsilon_{33}^{T'}$ has a minimum value ; while, at $\theta=0^0$, $\varepsilon_{33}^{S'}$ or $\varepsilon_{33}^{T'}$ reaches maximum, and $\varepsilon_{11}^{S'}$ or $\varepsilon_{11}^{T'}$ reaches minimum, which can be explained by the fact that $x_1^{'}$ and $x_3^{'}$ coincide with x_1 and x_3 respectively when θ is 0^0, and $x_1^{'}$ becomes x_3 and $x_3^{'}$ coincides with negative x_1 when θ is 90^0.

The strong *c*-axis tile angle dependency of material properties also can be seen in piezoelectric strain constant $d^{'}$ (3 x 6 matrix) and piezoelectric stress constant $e^{'}$ (3 x 6 matrix), and their non-zero constants are shown in Fig. 6 and 7.

B Simulation of impedance spectra of *c*-axis tilted ZnO and AlN FBARs with a mass loading layer

Using the impedance expression of FBAR and the calculated material properties including elastic, dielectric and piezoelectric coefficients, the resonator spectrum with mass loading can be simulated. The parameters used in the simulation are listed in Table I. The calculated impedance spectra of FBARs with different mass loading are shown in Fig. 8 and 9. For most angles, it can be seen that there are two resonance peaks. The first peak is shear resonance with resonant frequency around 0.7 GHz for ZnO FBAR and 1.5 GHz for AlN FBAR, and the second one is longitudinal resonance with resonant frequency around 1.5GHz for ZnO FBAR and 2.7 GHz for AlN FBAR. While For some specific angles, there is only one peak in the spectrum. This is because the resonator could be operated in a single mode when a tilt angle makes $k_L^2 = 0$ (pure shear mode) or $k_S^2 = 0$ (pure longitudinal mode) according to the impedance expression of FBAR. Through solving $k_L^2 = 0$ and $k_S^2 = 0$, it is found that pure longitudinal mode occurs at 0^0 and 65.4^0, and pure shear mode occurs at 43^0 and 90^0 for ZnO FBAR; pure longitudinal mode occurs at 0^0 and 67.1^0, and pure shear mode occurs at 46.1^0 and 90^0 for AlN FBAR. As mentioned before, the appearance of strong shear resonance for some certain tilt angles makes ZnO or AlN FBARs desirable for sensor application in liquid.

C. Mass sensitivity of *c*-axis tilted ZnO and AlN FBARs

From Fig. 8 and 9, we can see that both longitudinal peak and shear peak shift from right to left due to the mass loading. To have an overall understanding of dual mode FBAR as mass sensor, we gradually increase the mass loading by increase the thickness of mass loading layer, and examine the change of the resonant frequency f_s. f_s is the frequency corresponding to the maximum conductance of

resonator, which is preferred as sensor output. For a FBAR based on AlN or ZnO with c-axis tilt angle θ, we adopt $f_{sL}(\theta)$ and $f_{sS}(\theta)$ to express the longitudinal and shear resonant frequency, respectively.

Fig. 10 and 11 shows the change of $\dfrac{f_{sL}(\theta)}{\Delta f_{sL}(\theta)}$ and $\dfrac{f_{sS}(\theta)}{\Delta f_{sS}(\theta)}$ with the thickness of mass loading layer for some specific c-axis tilt angles, where the materials for mass loading layer are Al, SiO$_2$, Au and Pt with thickness from 0 to 500nm, and the material parameters for simulation are shown in Table I. It can be seen from Fig. 10 and 11 that both $\dfrac{f_{sL}(\theta)}{\Delta f_{sL}(\theta)}$ and $\dfrac{f_{sS}(\theta)}{\Delta f_{sS}(\theta)}$ are linearly proportional to the thickness of mass loading layer when the thickness is small. However, with further increased thickness, the decrease of $\dfrac{f_{sL}(\theta)}{\Delta f_{sL}(\theta)}$ and $\dfrac{f_{sS}(\theta)}{\Delta f_{sS}(\theta)}$ become fast for low acoustic impedance (lower than piezoelectric layer ZnO or AlN) mass loading material Al and SiO$_2$, and slowly for high acoustic impedance (higher than piezoelectric layer ZnO or AlN) mass loading material Au and Pt, which is believed to be due to the mismatch of acoustic impedance between mass loading layer and piezoelectric layer[20]. In addition we can easily find that the resonant frequency shift for Au and Pt is higher than Al and SiO$_2$, and this can be well explained by that Au and Pt have higher acoustic loading because of higher densities.

Following the mass sensitivity definition of sing mode FBARs[19], the mass sensitivity of dual mode resonator is defined as below:

$$S_L(\theta) = \frac{\Delta f_{sL}(\theta)/f_{sL}(\theta)}{\Delta m}, \ S_S(\theta) = \frac{\Delta f_{sS}(\theta)/f_{sS}(\theta)}{\Delta m} \tag{12}$$

where $S_L(\theta)$ is the longitudinal mode mass sensitivity of ZnO or AlN FBAR with c-axis tilt angle θ, and $S_S(\theta)$ is the shear mode mass sensitivity; $\Delta f_{sL}(\theta)$ and $\Delta f_{sS}(\theta)$ are resonant frequency shift for mass loading $\Delta m = \rho_m t_m$; ρ_m and t_m are the density and thickness of mass loading layer.

Using (12), the mass sensitivity of unload FBARs is calculated through measuring resonant frequency shift for 1nm mass loading. Table II and III list the mass sensitivity of FBAR based on 2μm

ZnO or AlN FBARs with *c*-axis tilt angle in the range of 0^0-90^0. Form Table II and III, we can see that both $S_L(\theta)$ and $S_S(\theta)$ are almost same for different mass loading material, and their minor difference can be understood since the piezoelectric layer and mass loading layer is not completely non lossy in our simulation.; we also can see that $S_L(\theta)$ has similar value with $S_S(\theta)$, and they do not change much with tilt angle: $S_L(\theta)$ and $S_S(\theta)$ of ZnO FBAR are around -900(cm^2/g), and $S_L(\theta)$ and $S_S(\theta)$ of AlN FBAR are around -1550(cm^2/g). The reason is shown below, according to (11), the longitudinal and shear mode vibration are found to interact each other through parameter α; for any θ, $c_{35}^{E'}$ is very small compared with $c_{33}^{E'}$ and $c_{55}^{E'}$ (shown in Fig. 2 and 3), which induces small α less than 5^0. Hence the coupling between longitudinal and shear mode is thought to be weak, and the resonator can be approximate to a simple combination of two single mode. The mass sensitivity (S_m) of single mode resonator is found only dependant on the density (ρ_p) and thickness (d_p) of the piezoelectric layer[19].

$$S_m = \frac{-1}{\rho_p d_p} \tag{37}$$

Hence, for ZnO or AlN dual mode FBARs, $S_L(\theta)$ and $S_S(\theta)$ are close, and do not change much with tilt angle although the material properties are greatly affected by the *c*-axis tilt angle.

It should be pointed out that the mass sensitivity (shown in Table II and III) with -876 (cm^2/g) to -925 (cm^2/g) for 2μm ZnO FBAR and -1534 (cm^2/g) to -1571 (cm^2/g) for 2μm AlN FBAR, are pretty high compared with the mass sensitivity of a 6M QCM, -14(cm^2/g) [19]. This high mass sensitivity with the existence of pure shear mode makes ZnO and AlN FBARs promising for sensor application in liquid.

IV. CONCLUSIONS

In summary, mass sensitivity of FBARs based on *c*-axis tilted ZnO and AlN thin films have been theoretically studied. It is found that the material properties and impedance spectra of FBARs are greatly dependant on the *c*-axis orientation. Pure shear resonant peak is found at 43^0 and 90^0 for ZnO, and 46.1^0

and 90^0 for AlN. The mass sensitivity of longitudinal and shear mode for 2µm ZnO or AlN FBAR is very close, and do not change much with c-axis tile angle with a value rang around -900 cm^2/g for ZnO and -1550 cm^2/g for AlN. This high mass sensitivity and the existence of pure shear mode make ZnO and AlN FBARs desirable for sensor application in liquid.

ACKNOWLEDGMENTS

[1]D. S. Ballantine, Jr., R. M. White, S. J. Martin, A. J. Ricco, G. C. Frye, E. T. Zellars, H. Wohltjen, *Acoustic wave sensors: Theory , Design, and physic-Chemical Applications* (Academic Press ,San Diego, 1997).

[2]J. W. Grate, S. J. Martin, and R. M. White, Anal. Chem. **65**, 940 (1993).

[3]J. W. Grate, S. J. Martin, and R. M. White, Anal. Chem. **65**, 987 (1993).

[4]M. Benetti, D. Cannatà, and F. Di Pietrantonio, Appl. Phys. Lett. **87**, 173504 (2005)

[5]H. Zhang, M. S Marma, E. S. Kim, C. E McKenna, and M. E Thompson, J. Micromech. Microeng., **15**, 1911 (2005).

[6]R. Gabl, H. -D. Feucht, H. Zeininger, G. Eckstein, M. Schreiter, R. Primig, D. Pitzer, and W. Wersing, Biosensors and Bioelectronics, **19**, 615 (2004).

[7]. Y. Chen, P. I. Reyes, Z. Duan, G. Saraf, R. Wittstruck, Y. Lu, O. Taratula and E. Galoppini, Journal of ELECTRONIC MATERIALS, **38**, 1605 (2009).

[8]G. Wingqvist, J. Bjurström, L. Liljeholm, I. Katardjiev, and A. L. SpetZ, IEEE Sensor Proceedings, 492 (2005).

[9]J. Bjurström, G. Wingqvist, and I. Katardjiev, IEEE Trans. Ultrason., Ferroelect., Freq. Control **53**, 2095 (2006).

[10]G. Wingqvist, J. Bjurström, L. Liljeholm, V. Yantchev, and I. Katardjiev, Sensors and Actuator B **123**, 466 (2007).

[11]F. Martin, M.-E. Jan, S. Rey-Mermet, B. Belgacem, D. Su, M. Cantoni, and P. Muralt, IEEE Trans. Ultrason., Ferroelect., Freq. Control **53**, 1339 (2006).

[12]F. Martin, M.-E. Jan, B. Belgacem, M.-A. Dubois, P. Muralt, Thin Solid Films **514**, 341 (2006).

[13]C. Chung, Y. Chen, C. Cheng, and K. Kao, IEEE Trans. Ultrason., Ferroelect., Freq. Control **55**, 857 (2008).

[14]H. F. Tiersten, *Linear Piezoelectric Plates Vibrations* (Plenum Press, New York, 1969).

[15]N. F. Foster, G. A. Coquin, G. A. Rozgonyi and F.A.Vannatta, IEEE Transactions on Sonics and Ultrasonics **15**, 28 (1968).

[16]G. Carlotti, G. Socino, A. Petri, and E. Verona, IEEE Ultrasonic Symposium, 295 (1987).

[17]J. F. Rosenbaum, *Bulk Acoustic Waves Theory and Devices*, (Artech House, boston,1988).

[18]K. Tsubouchi, K. Sugai, N. Mikoshiba, IEEE Ultrasonic Symposium, 375 (1981).

[19]R. P. O'Toole, S. G. Burns, G. J. Bastiaans and M. D. Porter, Anal. Chem., **64**, 1289 (1992).

[20] G. Wingqvist, V. Yantchev, J. Bjurstrom and I. Katardjiev, Proc. IEEE FCS, 581 (2007)

Caption of Tables and Figures:

TABLE I. Materials properties and data used in theoretical calculation

TABLE II. Mass sensitivity of FBAR based on c-axis tilted ZnO

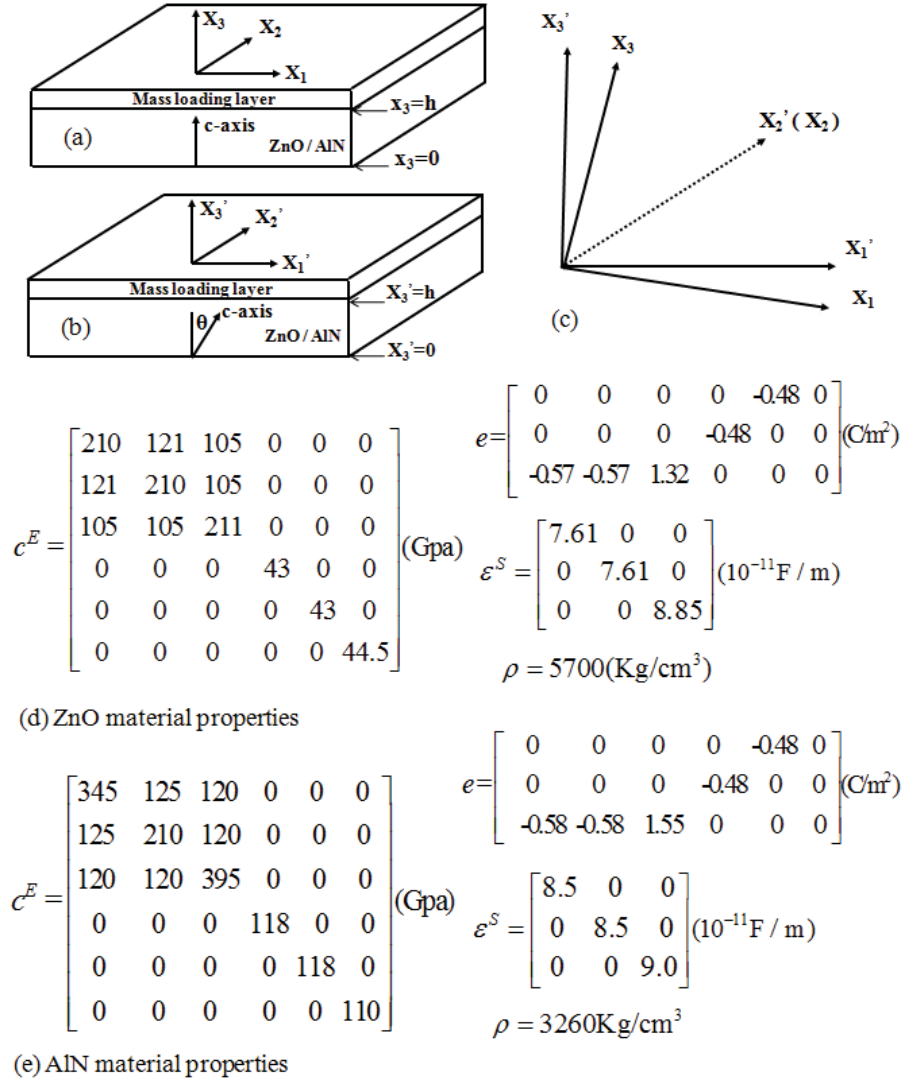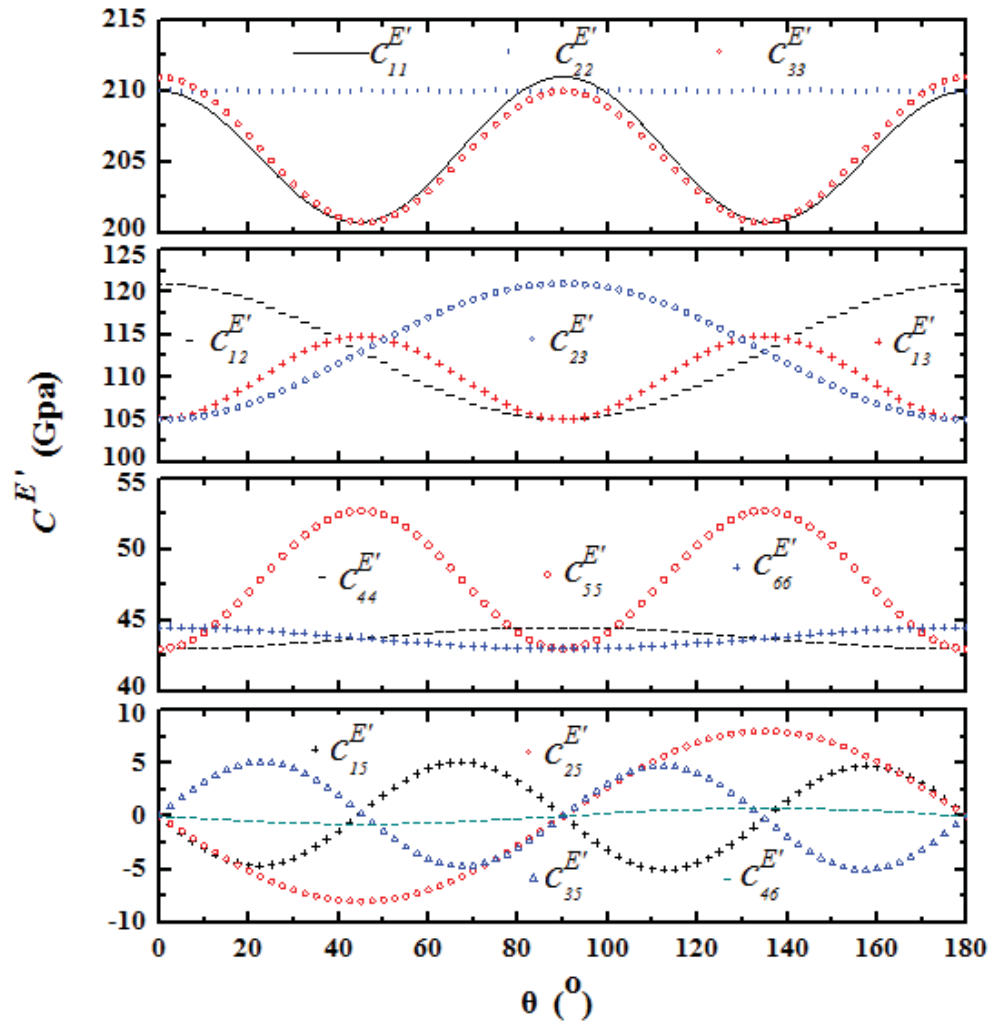TABLE II. Mass sensitivity of FBAR based on c-axis tilted AlN

FIG. 1. The schematic of FBARs based on c-axis tilted ZnO or AlN thin film and coordinate systems: (a) FBAR based on ZnO or AlN thin film with normal c-axis and coordinate system (X_1, X_2, X_3), (b) FBAR based on ZnO or AlN thin film with tilted c-axis and coordinate system $(X_1^{'}, X_2^{'}, X_3^{'})$, (c) the relation of (X_1, X_2, X_3) and $(X_1^{'}, X_2^{'}, X_3^{'})$, (d) ZnO material properties in (X_1, X_2, X_3), and (e) AlN material properties in (X_1, X_2, X_3).
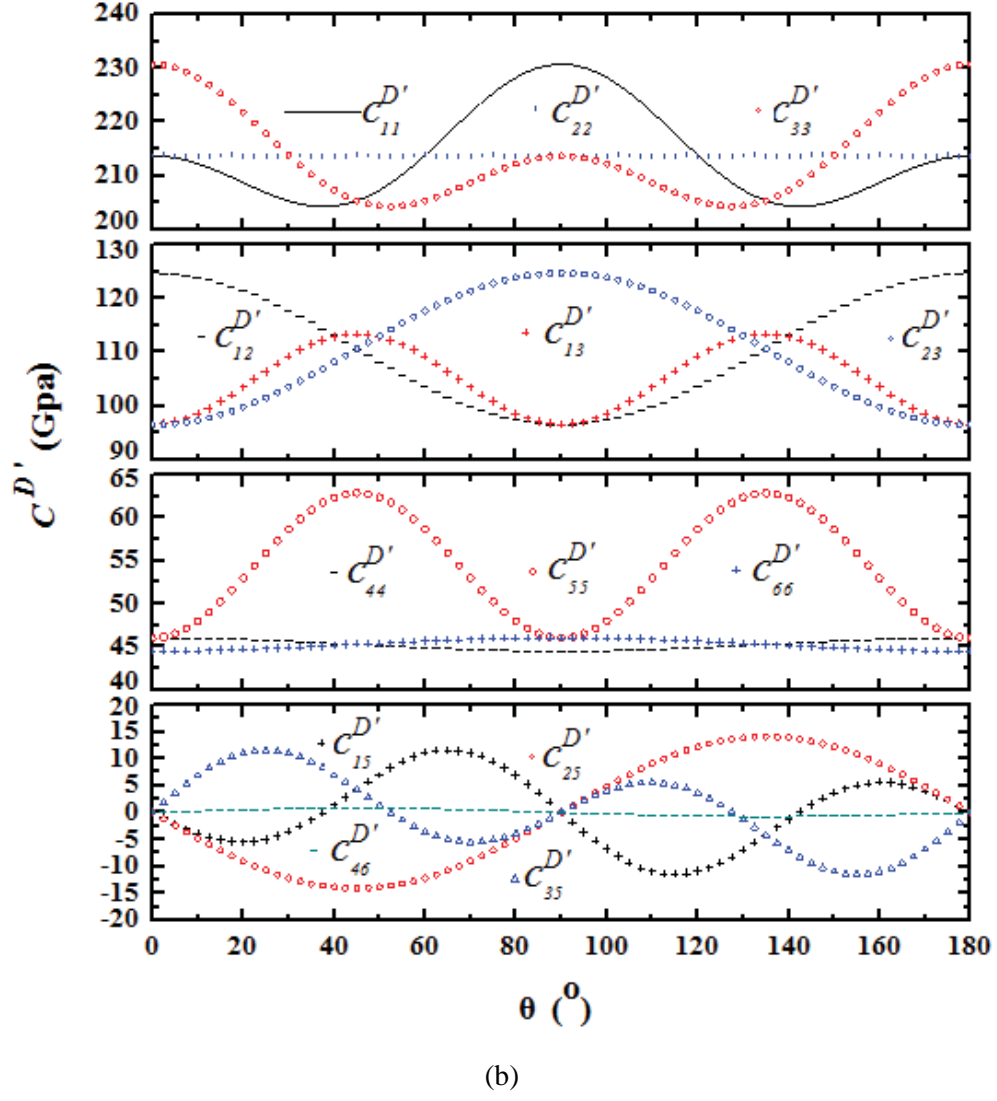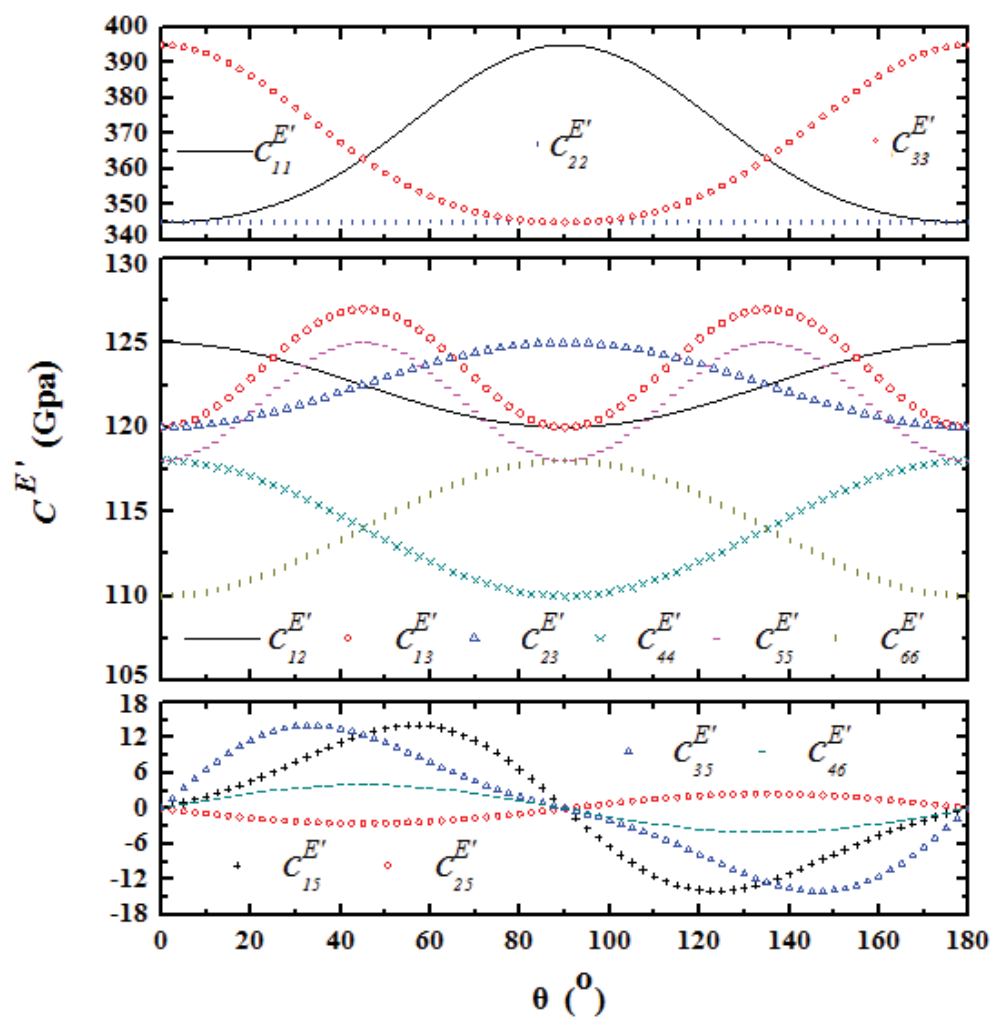
FIG. 2. The elastic constants of ZnO thin film as a function of tilt angle: (a) $c^{E'}$, (b) $c^{D'}$

FIG. 3. The elastic constants of AlN thin film as a function of tilt angle: (a) $c^{E'}$, (b) $c^{D'}$

FIG. 4. The dielectric constants of ZnO thin film as a function of tilt angle: $\varepsilon_{33}^{S'}$, $\varepsilon_{33}^{T'}$

FIG. 5. The dielectric constants of AlN thin film as a function of tilt angle: $\varepsilon_{33}^{S'}$, $\varepsilon_{33}^{T'}$

FIG. 6. The piezoelectric constants of ZnO thin film as a function of tilt angle: (a) $e^{'}$, (b) $d^{'}$.

FIG. 7. The piezoelectric constants of AlN thin film as a function of tilt angle: (a) $e^{'}$, (b) $d^{'}$.

FIG. 8. Simulation of impedance spectrum of FBAR based on c-axis tilted ZnO thin film(S: Shear mode, L: Longitudinal Mode).

FIG. 9. Simulation of impedance spectrum of FBAR based on c-axis tilted AlN thin film(S: Shear mode, L: Longitudinal Mode).

FIG. 10. Resonant frequency shift of FBAR based on c-axis tilted ZnO film with different mass loading.

FIG. 11. Resonant frequency shift of FBAR based on c-axis tilted AlN film with different mass loading.

TABLE I. Materials properties and data used in theoretical calculation

Piezoelectric layer	Density (kg/m^3)	Thickness (μm)	Electrode area (μm×μm)		Mechanical quality factor of longitudinal mode	Mechanical quality factor of Shear mode
ZnO	5700	2	300×300		350	400
AlN	3260				350	400

Mass loading layer	Density (kg/m^3)	Thickness (nm)	Young's modulus (GPa)	Poisson's ratio	Mechanical quality factor of longitudinal mode	Mechanical quality factor of Shear mode
SiO$_2$	2200	0-500	70	0.17	1000	1000
Al	2700		70	0.35		
Au	19300		79	0.44		
Pt	21450		168	0.38		

TABLE **II**. Mass sensitivity of FBAR based on *c*-axis tilted ZnO

c-axis θ (^{0})	$S_L(\theta)$ (cm^2/g)				$S_S(\theta)$ (cm^2/g)			
	SiO$_2$	Al	Au	Pt	SiO$_2$	Al	Au	Pt
0	-908	-908	-907	-904				
15	-899	-899	-896	-895	-900	-900	-896	-900
30	-883	-883	-881	-881	-925	-925	-922	-923
43					-915	-915	-912	-914
60	-881	-881	-881	-881	-880	-880	-881	-876
65.4	-881	-881	-881	-881				
75	-880	-880	-876	-876	-885	-885	-886	-886
90					-901	-901	-902	-900

TABLE III. Mass sensitivity of FBAR based on c-axis tilted AlN

c-axis	$S_L(\theta)$ (cm²/g)				$S_S(\theta)$ (cm²/g)			
$\theta\,(^0)$	SiO_2	Al	Au	Pt	SiO_2	Al	Au	Pt
0	-1571	-1571	-1565	-1566				
15	-1561	-1561	-1554	-1557	-1551	-1550	-1544	-1543
30	-1542	-1542	-1539	-1539	-1573	-1573	-1570	-1566
46.1	-1562	-1562	-1560	-1557				
60	-1537	-1537	-1534	-1534	-1548	-1548	-1544	-1543
67.1	-1536	-1536	-1534	-1534				
75	-1537	-1537	-1534	-1534	-1536	-1536	-1534	-1529
90					-1537	-1537	-1534	-1534

FIG. 1. The schematic of FBARs based on *c*-axis tilted ZnO or AlN thin film and coordinate systems: (a) FBAR based on ZnO or AlN thin film with normal *c*-axis and coordinate system (X_1, X_2, X_3), (b) FBAR based on ZnO or AlN thin film with tilted *c*-axis and coordinate system ($X_1^{'}$, $X_2^{'}$, $X_3^{'}$), (c) the relation of (X_1, X_2, X_3) and ($X_1^{'}$, $X_2^{'}$, $X_3^{'}$), (d) ZnO material properties in (X_1, X_2, X_3), and (e) AlN material properties in (X_1, X_2, X_3).

(a)

FIG. 2. The elastic constants of ZnO thin film as a function of tilt angle: (a) $c^{E'}$, (b) $c^{D'}$

(a)
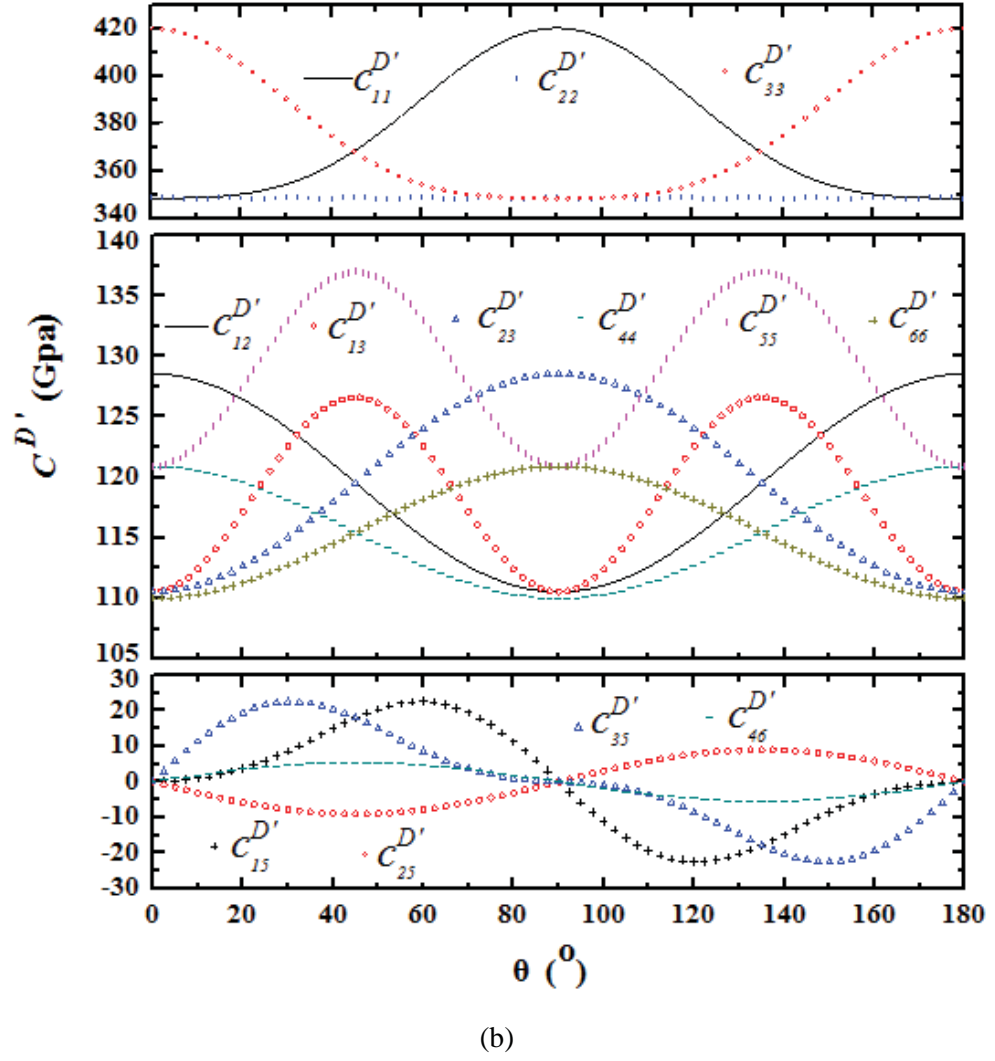
(b)

FIG. 3. The elastic constants of AlN thin film as a function of tilt angle: (a) $c^{E'}$, (b) $c^{D'}$
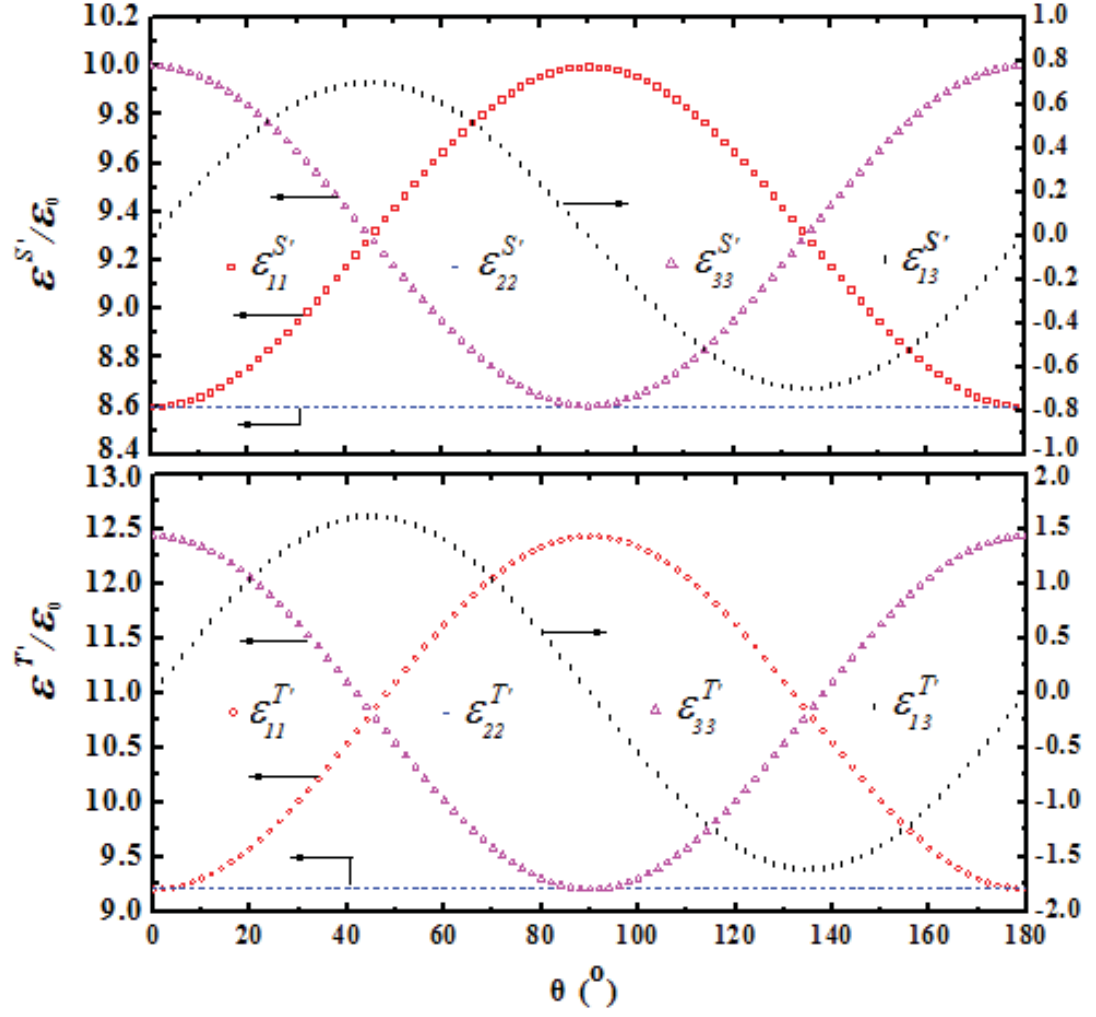
FIG. 4. The dielectric constants of ZnO thin film as a function of tilt angle: $\varepsilon_{33}^{S'}$, $\varepsilon_{33}^{T'}$
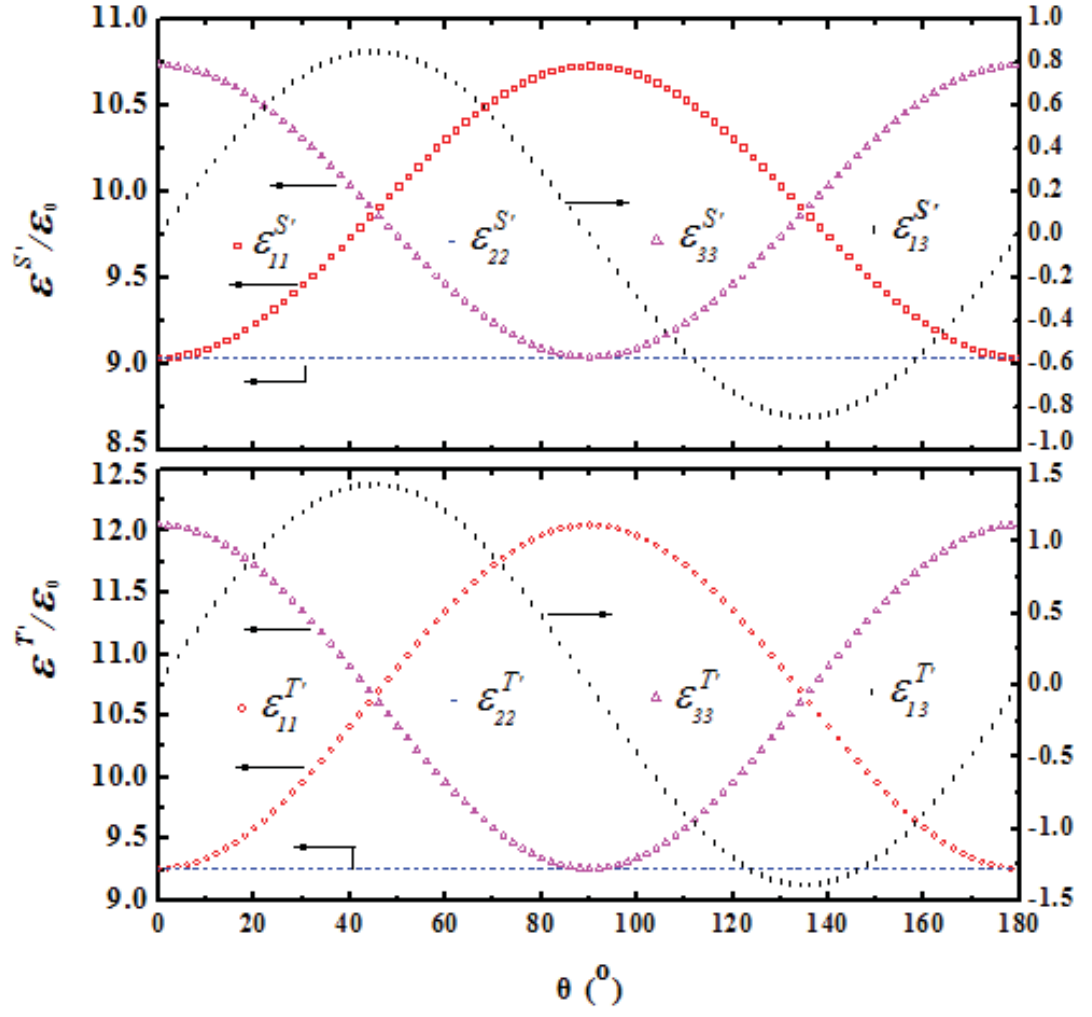
FIG. 5. The dielectric constants of AlN thin film as a function of tilt angle: $\varepsilon_{33}^{S'}$, $\varepsilon_{33}^{T'}$
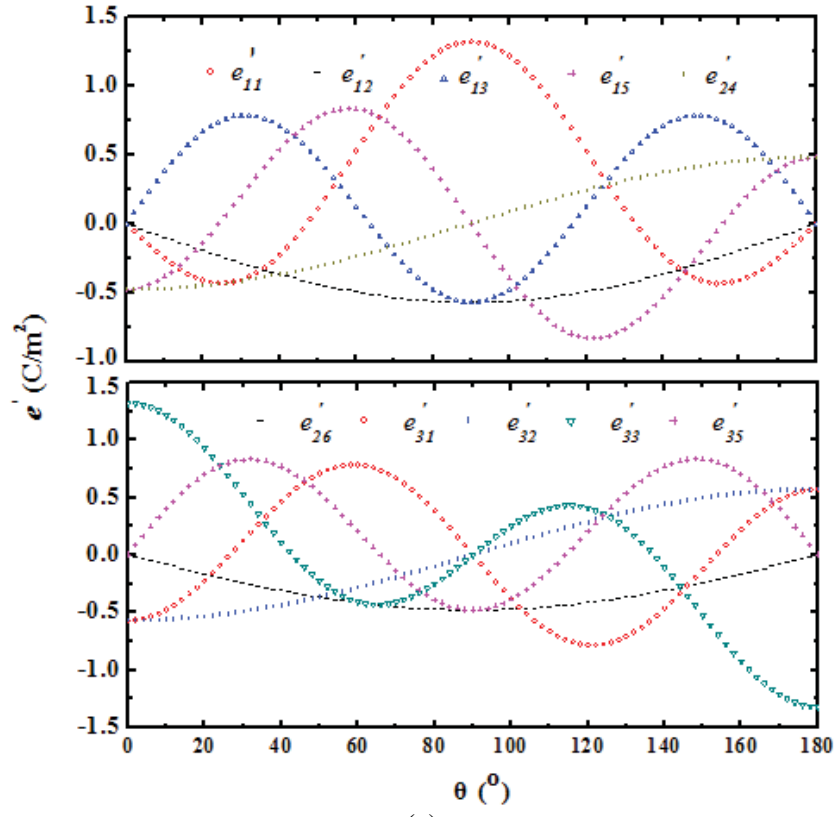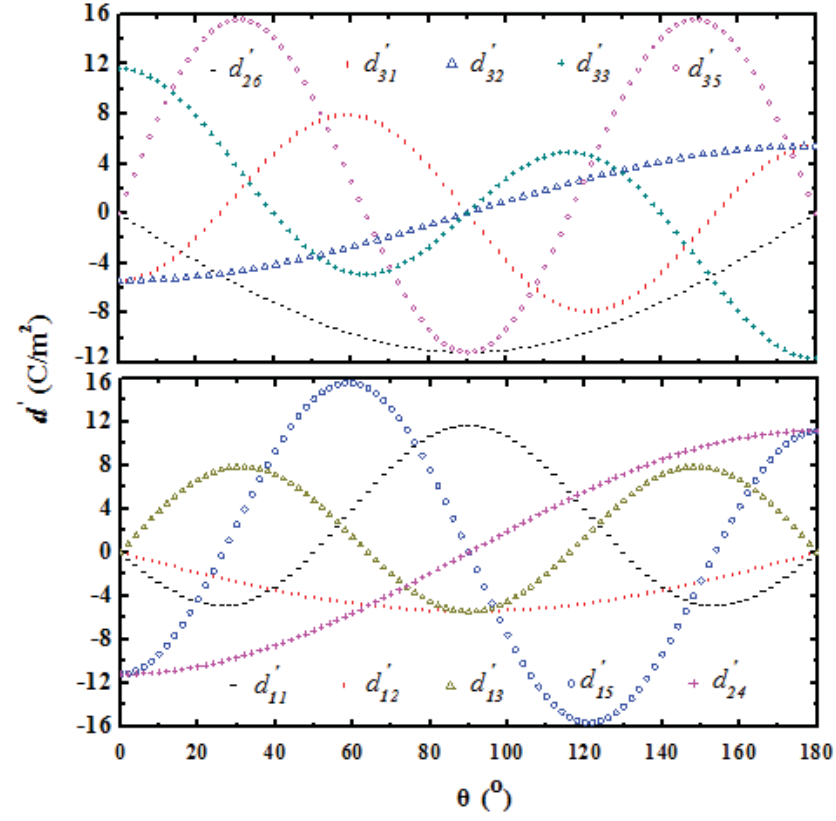
FIG. 6. The piezoelectric constants of ZnO thin film as a function of tilt angle: (a) e', (b) d'
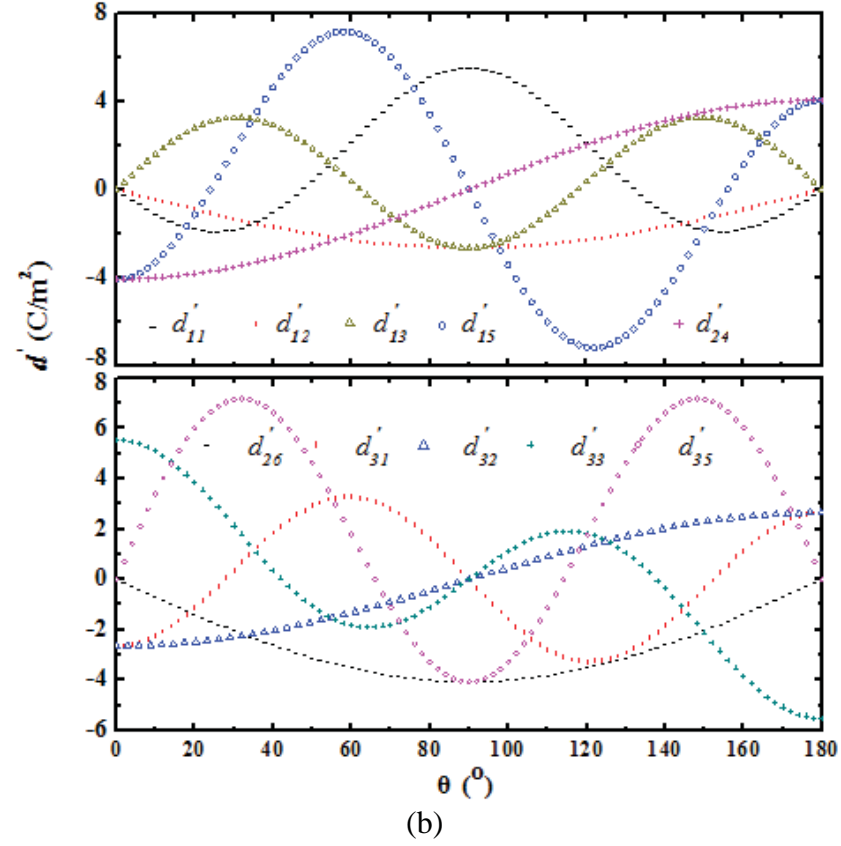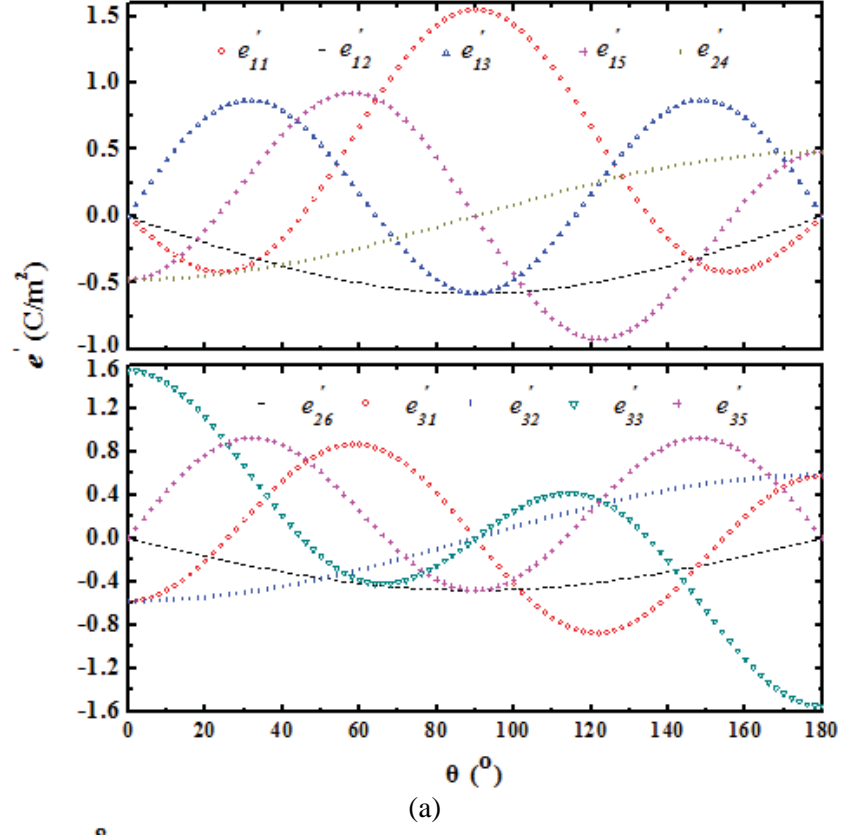
FIG. 7. The piezoelectric constants of AlN thin film as a function of tilt angle: (a) $e^{'}$, (b) $d^{'}$

(a)

FIG. 8. Simulation of impedance spectrum of FBAR based on *c*-axis tilted ZnO thin film(S: Shear mode, L: Longitudinal Mode).
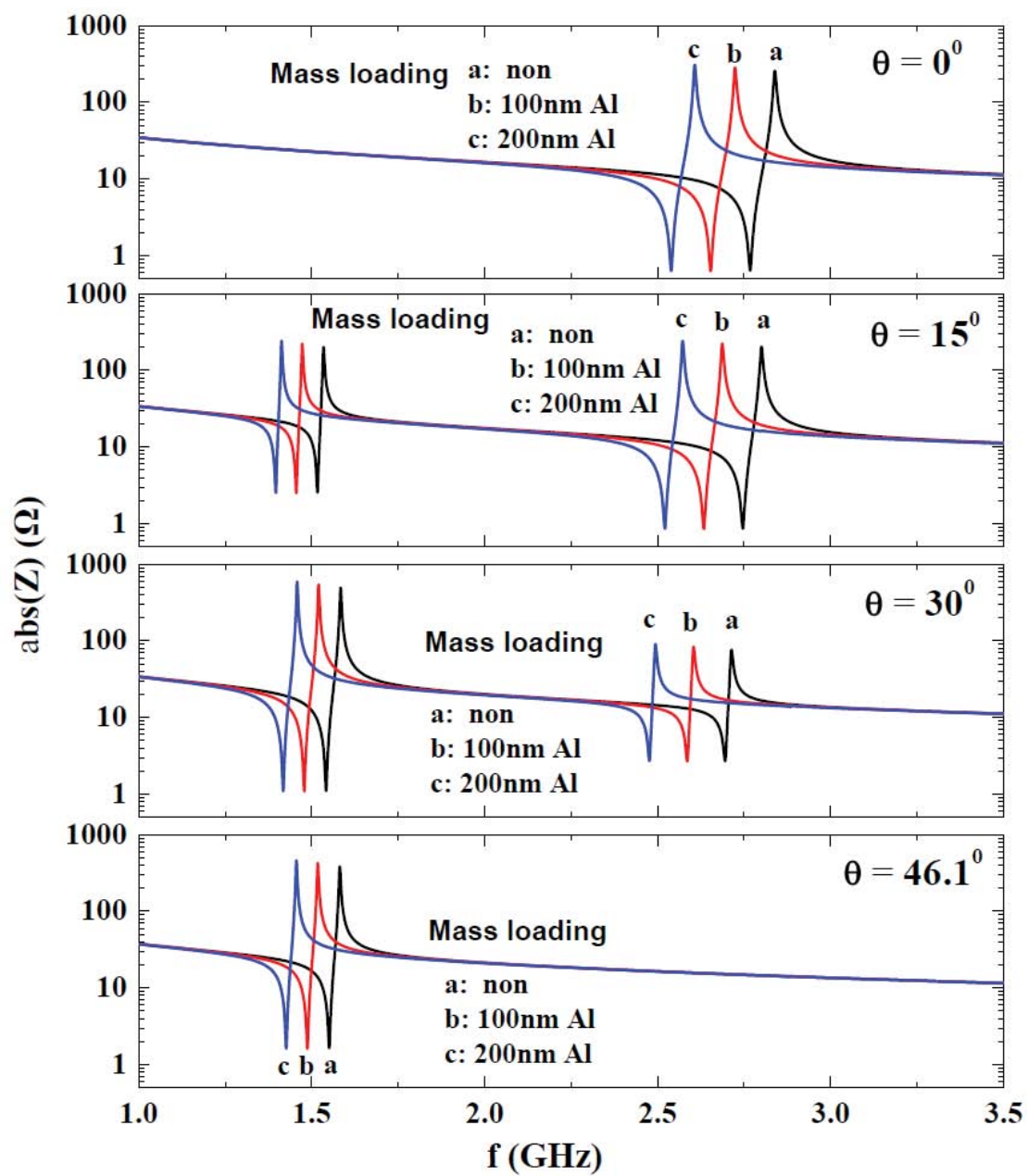
(a)
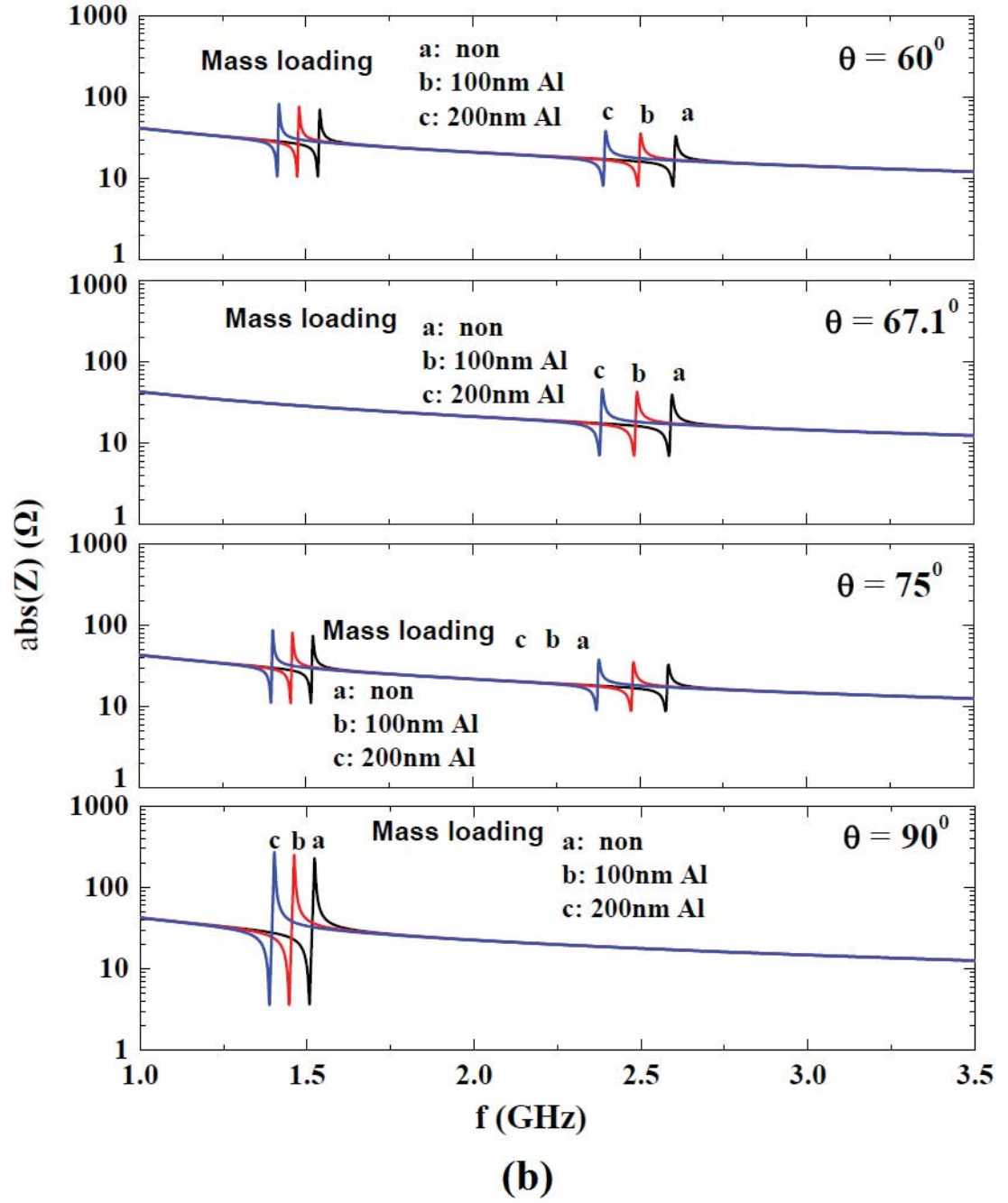
FIG. 9. Simulation of impedance spectrum of FBAR based on *c*-axis tilted AlN thin film(S: Shear mode, L: Longitudinal Mode).
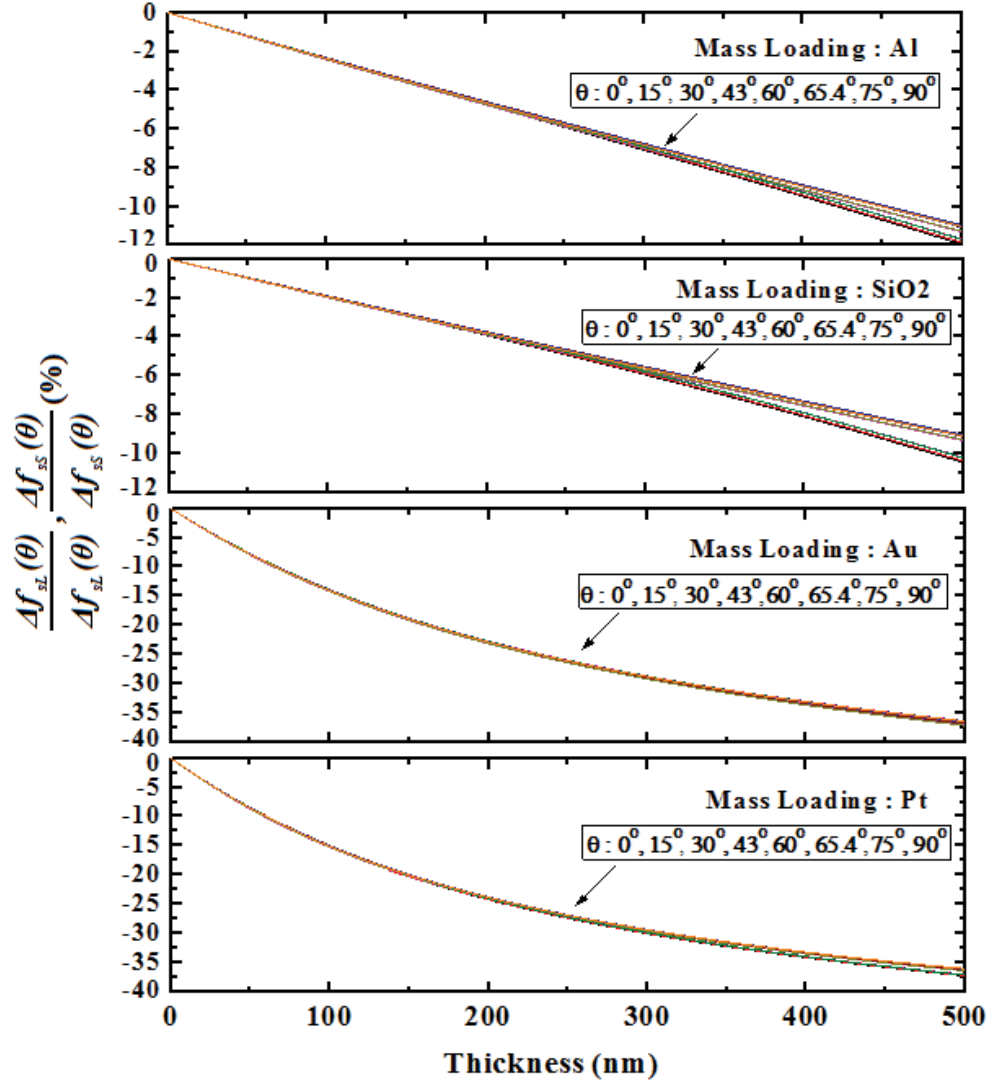
FIG. 10. Resonant frequency shift of FBAR based on *c*-axis tilted ZnO film with different mass loading.
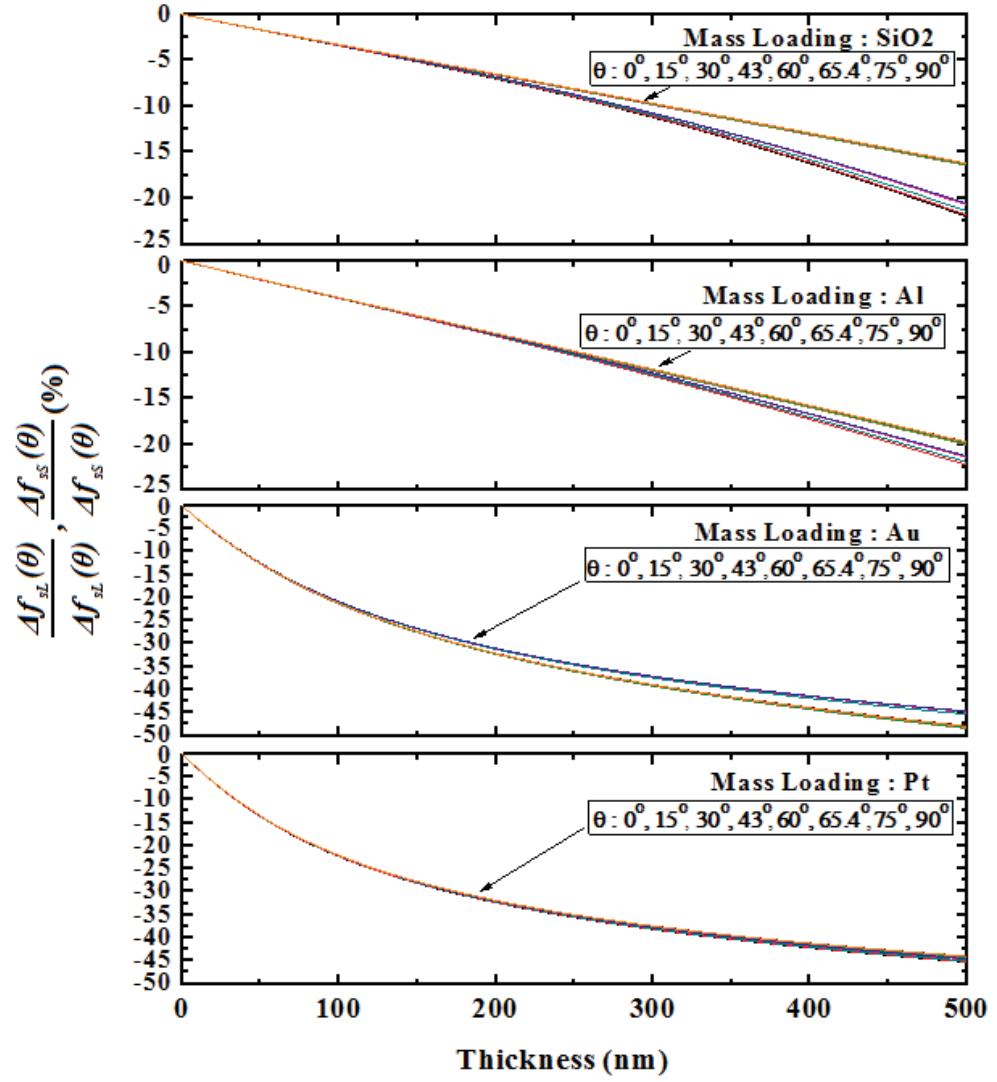
FIG. 11. Resonant frequency shift of FBAR based on *c*-axis tilted AlN film with different mass loading.

Analysis of dual-mode thin film bulk acoustic resonators based on polar *c*-axis tilted wurtzite gallium nitride

Lifeng Qin and Qing-Ming Wang[a)]

Department of Mechanical Engineering and Materials Science, University of Pittsburgh, Pittsburgh, Pennsylvania 15261, USA

We present the analytical study of dual-mode thin film bulk acoustic resonators (FBARs) based on wurtzite gallium nitride (GaN) thin films with tilted *c*-axis orientation. The normal-plane and in-plane electric polarization vector components caused by the titled *c*-axis orientation induce the coexistence of the thickness longitudinal and thickness shear modes in the thin film resonator. Due to the *c*-axis orientation dependency of material properties including elastic stiffness, dielectric constants, and piezoelectric coefficients, bulk wave properties of FBARs including acoustic velocity and electromechanical coupling coefficient, and electrical impedance spectra are greatly affected by the tilt angle. It is found that the pure longitudinal mode occurs at $\theta=0°$ and $66.4°$, and the pure shear mode occurs at $\theta=42.8°$ and $90°$. In addition, the electromechanical coupling coefficient for thickness shear mode has a maximum value 3.18% at $\theta=34.2°$, which is larger than the maximum value for pure thickness longitudinal mode 2.44% at $\theta=0°$. The calculation results show that FBARs based on tilted *c*-axis wurtzite GaN thin films are promising for frequency control device design and applications. © 2010 American Institute of Physics. [doi:10.1063/1.3427434]

I. INTRODUCTION

In the past years, thin film bulk acoustic wave resonators (FBARs) have attracted much attention for application in rf and microwave frequency control and signal processing fields such as cellular phones, navigation, satellite communication, and other data communication systems like wireless local area networks.[1–5] Commonly, FBAR consists of one thin piezoelectric layer with two metal electrodes deposited on both sides. Aluminum nitride (AlN) and zinc oxide (ZnO) are the mainstream piezoelectric materials for FBARs fabrication, and their thickness usually ranges from several micrometers down to tenth of micrometers, which results in high resonant frequency from hundreds of megahertz (MHz) to over tens of gigahertz (GHz). In addition to applications in electronic circuits as frequency control devices, FBARs can also be used for sensor application. In the case of mass sensor application as the quartz microbalance, it is well known that the resonant frequency will change due to surface mass change, and the absolute frequency is proportional to the square of the operating frequency.[6,7] Therefore, using FBAR structures, with operation frequency in GHz range, can greatly improve the sensitivity of the device. In fact, chemical sensors based on FBARs have been experimentally investigated for low concentration detection, which showed much higher sensitivity and resolution comparable to quartz crystal microbalances.[8]

FBARs are often operated in thickness longitudinal mode since the ZnO and AlN thin film materials used for device fabrication are usually with normal-plane *c*-axis orientation. For sensor applications in liquid medium, thickness shear mode bulk acoustic wave resonators are needed. This is because liquid cannot support shear wave, the damping caused by the liquid medium is not severe for thickness shear mode bulk acoustic wave resonator; while for thickness longitudinal mode resonator, the acoustic wave energy is radiated into liquid through compressional motion, leading to significant damping in the liquid medium. Fortunately, previous research works have shown that thickness shear mode can be excited through the use of AlN and ZnO thin films with tilted *c*-axis orientation.[9–14]

Until now, GaN thin films have received a great attention for potential high frequency, high temperature, and high power applications due to the unique properties of large forbidden gap, considerable hardness, and high thermal conductivity.[15–17] The piezoelectric properties of wurtzite GaN also make it an exciting material for manufacture of FBARs. For example, FBAR with resonant frequency up to 6.3 GHz and quality factor higher than 1100 has been achieved using GaN thin film.[18] The polar *c*-axis orientation of GaN thin film is usually normal to substrate surface, which produces only thickness longitudinal mode and cannot be applied for sensor application in liquid as mentioned before. Films with in-plane polarization have also been fabricated on certain substrate crystal such as tetragonal (γ) LiAlO$_2$ (100) for the fabrication of structures free of electrostatic fields for efficient white light-emitting diodes.[19] In this paper, we consider GaN film with tilted polar *c*-axis from normal-plane to in-plane change, and examine the orientation dependence of elastic, dielectric, and piezoelectric property of wurtzite GaN thin film; further the characteristics of dual-mode thin film resonators will be analyzed.

II. THEORETICAL ANALYSIS

A. Material properties of *c*-axis tilted wurtzite GaN

The material properties of wurtzite GaN thin films with tilted *c*-axis can be calculated from properties of wurtzite

---

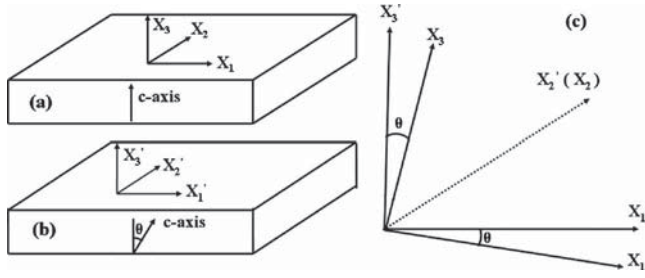a)Electronic mail: qmwang@engr.pitt.edu.

107, 114102-1

FIG. 1. The schematic of FBARs based on wurtzite GaN thin film and coordinate systems: (a) FBAR based on wurtzite GaN thin film with normal c-axis and coordinate system (X_1, X_2, X_3), (b) FBAR based on wurtzite GaN with tilted c-axis and coordinate system (X_1', X_2', X_3'), and (c) the relation of (X_1, X_2, X_3) and (X_1', X_2', X_3').

GaN thin films with normal c-axis through coordinate system rotation. Figure 1(a) shows FBAR based on wurtzite GaN thin film with normal c-axis, and (x_1, x_2, x_3) is the original material coordinate; Fig. 1(b) shows the schematic of FBAR based on c-axis tilted wurtzite GaN, where the top and bottom electrode are ignored. A rectangular Cartesian coordinate system (x_1', x_2', x_3') is chosen with top electrode on x_3'

$= h$ and bottom electrode on $x_3' = 0$. The c-axis of GaN film is tilted at an angle θ to the x_3' direction. Coordinate system (x_1', x_2', x_3') can be treated as the result of rotation of (x_1, x_2, x_3) about x_2 with an angle θ, as shown in Fig. 1(c). For the characterization of c-axis tilted wurtzite GaN FBARs, the material properties in (x_1', x_2', x_3') need to be known. Assuming the dielectric permittivity, piezoelectric stress coefficient, and elastic stiffness are (ε', e', c') for coordinate system (x_1', x_2', x_3'), and (ε, e, c) for coordinate system (x_1, x_2, x_3), the material properties in new coordinate system can be computed through properties in original coordinate system with the aids of matrix algebra[19]

$$\varepsilon' = a\varepsilon a^t, \tag{1}$$

$$e' = aeM^t, \tag{2}$$

$$c' = McM^t, \tag{3}$$

$$a = \begin{bmatrix} a_{11} & a_{12} & a_{13} \\ a_{21} & a_{22} & a_{23} \\ a_{31} & a_{32} & a_{33} \end{bmatrix} = \begin{bmatrix} \cos(\theta) & 0 & \sin(\theta) \\ 0 & 1 & 0 \\ -\sin(\theta) & 0 & \cos(\theta) \end{bmatrix}, \tag{4}$$

$$M = \begin{bmatrix} a_{11}^2 & a_{12}^2 & a_{13}^2 & 2a_{12}a_{13} & 2a_{11}a_{13} & 2a_{11}a_{12} \\ a_{21}^2 & a_{22}^2 & a_{23}^2 & 2a_{22}a_{23} & 2a_{21}a_{23} & 2a_{21}a_{22} \\ a_{31}^2 & a_{32}^2 & a_{33}^2 & 2a_{32}a_{33} & 2a_{31}a_{33} & 2a_{31}a_{32} \\ a_{21}a_{31} & a_{22}a_{32} & a_{23}a_{33} & a_{22}a_{33} + a_{23}a_{32} & a_{21}a_{33} + a_{23}a_{31} & a_{21}a_{32} + a_{22}a_{31} \\ a_{11}a_{31} & a_{12}a_{32} & a_{13}a_{33} & a_{12}a_{33} + a_{13}a_{32} & a_{11}a_{33} + a_{13}a_{31} & a_{11}a_{32} + a_{12}a_{31} \\ a_{11}a_{21} & a_{12}a_{22} & a_{13}a_{23} & a_{12}a_{23} + a_{13}a_{22} & a_{11}a_{23} + a_{13}a_{21} & a_{11}a_{22} + a_{12}a_{21} \end{bmatrix}, \tag{5}$$

where θ is the tilt angle, a^t is the transpose of a, and M^t is the transpose of M.

B. Impedance of FBAR based on c-axis tilted wurtzite GaN

Following a similar procedure,[21] the equation for c-axis tilted FBAR impedance is derived. According to the acoustic field equations and piezoelectric constitution equations, in the coordinate system (x_1', x_2', x_3') we have[20]

$$\begin{bmatrix} \dfrac{\partial}{\partial x_1'} & 0 & 0 & 0 & \dfrac{\partial}{\partial x_3'} & \dfrac{\partial}{\partial x_2'} \\ 0 & \dfrac{\partial}{\partial x_2'} & 0 & \dfrac{\partial}{\partial x_3'} & 0 & \dfrac{\partial}{\partial x_1'} \\ 0 & 0 & \dfrac{\partial}{\partial x_3'} & \dfrac{\partial}{\partial x_2'} & \dfrac{\partial}{\partial x_1'} & 0 \end{bmatrix} \begin{bmatrix} T_1 \\ T_2 \\ T_3 \\ T_4 \\ T_5 \\ T_6 \end{bmatrix} = \rho \begin{bmatrix} \dfrac{\partial^2 u_1}{\partial t^2} \\ \dfrac{\partial^2 u_2}{\partial t^2} \\ \dfrac{\partial^2 u_3}{\partial t^2} \end{bmatrix}, \tag{6}$$

$$\begin{bmatrix} S_1 \\ S_2 \\ S_3 \\ S_4 \\ S_5 \\ S_6 \end{bmatrix} = \begin{bmatrix} \partial/\partial x_1' & 0 & 0 \\ 0 & \partial/\partial x_2' & 0 \\ 0 & 0 & \partial/\partial x_3' \\ 0 & \partial/\partial x_3' & \partial/\partial x_2' \\ \partial/\partial x_3' & 0 & \partial/\partial x_1' \\ \partial/\partial x_2' & \partial/\partial x_1' & 0 \end{bmatrix} \begin{bmatrix} u_1 \\ u_2 \\ u_3 \end{bmatrix}, \tag{7}$$

$$T_p = c_{pq}^{E'} S_q - e_{kp}' E_k, \tag{8}$$

$$D_i = e_{iq}' S_q + \varepsilon_{ik}^{S'} E_k, \tag{9}$$

where T_p, S_q, D_i, and E_k are the components of stress, strain, electric displacement, and electric field intensity, $c_{pq}^{E'}$ are the elastic stiffness constants under constant electric field intensity, e_{kp}' are the piezoelectric stress constants, $\varepsilon_{ik}^{S'}$ are the permittivity constants under constant strain, and u_i is the displacement in the direction of x_i' ($i, k = 1, 2, 3$ and $p, q = 1, 2, 3, 4, 5, 6$). The thickness of GaN is much smaller than the lateral dimensions, which means that the resonator vibra-

tion can be treated as one dimension problem; hence, we can assume

$$\frac{\partial T_i}{\partial x_1'} = \frac{\partial T_i}{\partial x_2'} = 0, \tag{10}$$

$$E_1 = E_2 = 0, E_3 \neq 0, \tag{11}$$

$$\frac{\partial D_3}{\partial x_3'} = 0. \tag{12}$$

For a sinusoidal excitation, the voltage V and current I across FBAR are expressed by

$$V = \int_0^h E_3 dx_3', \tag{13}$$

$$I = j\omega A D_3, \tag{14}$$

where A is the area of the electrodes, ω is the angle frequency. The traction force at the boundary ($x_3' = 0, h$) is zero, thus we have

$$T_5(0) = T_5(h) = T_3(0) = T_3(h) = 0. \tag{15}$$

For any tilt angle θ, it is found

$$c_{34}^{E'} = c_{45}^{E'} = e_{34}' = 0. \tag{16}$$

From Eqs. (6)–(16), the impedance of FBAR can be solved

$$Z = \frac{V}{I} = \frac{1}{j\omega C_0}\left(1 - k_L^2 \frac{\tan(\gamma_L/2)}{\gamma_L/2} - k_S^2 \frac{\tan(\gamma_S/2)}{\gamma_S/2}\right), \tag{17a}$$

where

$$\gamma_L = \frac{\omega h}{v^{(L)}}, \tag{17b}$$

$$\gamma_S = \frac{\omega h}{v^{(S)}}, \tag{17c}$$

$$v^{(L)} = \left[\frac{\overline{c_{33}^{E'}} + \overline{c_{55}^{E'}}}{2\rho} + \sqrt{\left(\frac{\overline{c_{33}^{E'}} - \overline{c_{55}^{E'}}}{2\rho}\right)^2 + \left(\frac{\overline{c_{35}^{E'}}}{\rho}\right)^2}\right]^{1/2}, \tag{17d}$$

$$v^{(S)} = \left[\frac{\overline{c_{33}^{E'}} + \overline{c_{55}^{E'}}}{2\rho} - \sqrt{\left(\frac{\overline{c_{33}^{E'}} - \overline{c_{55}^{E'}}}{2\rho}\right)^2 + \left(\frac{\overline{c_{35}^{E'}}}{\rho}\right)^2}\right]^{1/2}, \tag{17e}$$

$$\overline{c_{33}^{E'}} = c_{33}^{E'} + \frac{(e_{33}')^2}{\varepsilon_{33}^{S'}}, \tag{17f}$$

$$\overline{c_{35}^{E'}} = c_{35}^{E'} + \frac{e_{33}' e_{35}'}{\varepsilon_{33}^{S'}}, \tag{17g}$$

$$\overline{c_{55}^{E'}} = c_{55}^{E'} + \frac{(e_{35}')^2}{\varepsilon_{33}^{S'}}, \tag{17h}$$

TABLE I. Material properties of wurtzite GaN (Refs. 22–24).

Property		GaN
Elastic stiffness matrix (GPa)[a]	c_{11}^E	390
$c^E = \begin{bmatrix} c_{11} & c_{12} & c_{13} & 0 & 0 & 0 \\ c_{12} & c_{11} & c_{13} & 0 & 0 & 0 \\ c_{13} & c_{13} & c_{33} & 0 & 0 & 0 \\ 0 & 0 & 0 & c_{44} & 0 & 0 \\ 0 & 0 & 0 & 0 & c_{44} & 0 \\ 0 & 0 & 0 & 0 & 0 & c_{66} \end{bmatrix}$	c_{12}^E c_{13}^E c_{33}^E c_{44}^E c_{66}^E	145 106 398 105 123
Piezoelectric strain coefficient matrix (pm/V)[b]	d_{31}	−1.7
$d = \begin{bmatrix} 0 & 0 & 0 & 0 & d_{15} & 0 \\ 0 & 0 & 0 & d_{15} & 0 & 0 \\ d_{31} & d_{31} & d_{33} & 0 & 0 & 0 \end{bmatrix}$	d_{33} d_{15}	3.4 −3.1
Dielectric constant matrix[c]	ε_{11}^S	8.05
$\varepsilon^S = \begin{bmatrix} \varepsilon_{11}^S & 0 & 0 \\ 0 & \varepsilon_{11}^S & 0 \\ 0 & 0 & \varepsilon_{33}^S \end{bmatrix}$	ε_{33}^S	11.2

[a]Reference 22.
[b]Reference 23.
[c]Reference 24.

$$C_0 = \varepsilon_{33}^{S'} A/h, \tag{17i}$$

$$k_L^2 = \frac{(e_L)^2}{\varepsilon_{33}^{S'}\rho(v^{(L)})^2}, \tag{17j}$$

$$k_S^2 = \frac{(e_S)^2}{\varepsilon_{33}^{S'}\rho(v^{(S)})^2}, \tag{17k}$$

$$e_L = e_{35}' \sin(\alpha) + e_{33}' \cos(\alpha), \tag{17l}$$

$$e_S = e_{35}' \cos(\alpha) - e_{33}' \sin(\alpha), \tag{17m}$$

$$\alpha = \frac{1}{2}\arctan\left(\frac{2\overline{c_{35}^{E'}}}{\overline{c_{33}^{E'}} - \overline{c_{55}^{E'}}}\right). \tag{17n}$$

Here, f is frequency, $v^{(L)}$ and $v^{(S)}$ are the acoustic velocities for longitudinal mode and shear mode, and k_L^2 and k_S^2 are, respectively, defined as the electromechanical coupling coefficient for the longitudinal and shear mode.

III. RESULTS AND DISCUSSION

A. Dependence of wurtzite GaN properties on the tilt angle

Using Eqs. (1)–(5) and material properties in Table I, the material properties in (x_1', x_2', x_3') can be calculated. We cal-
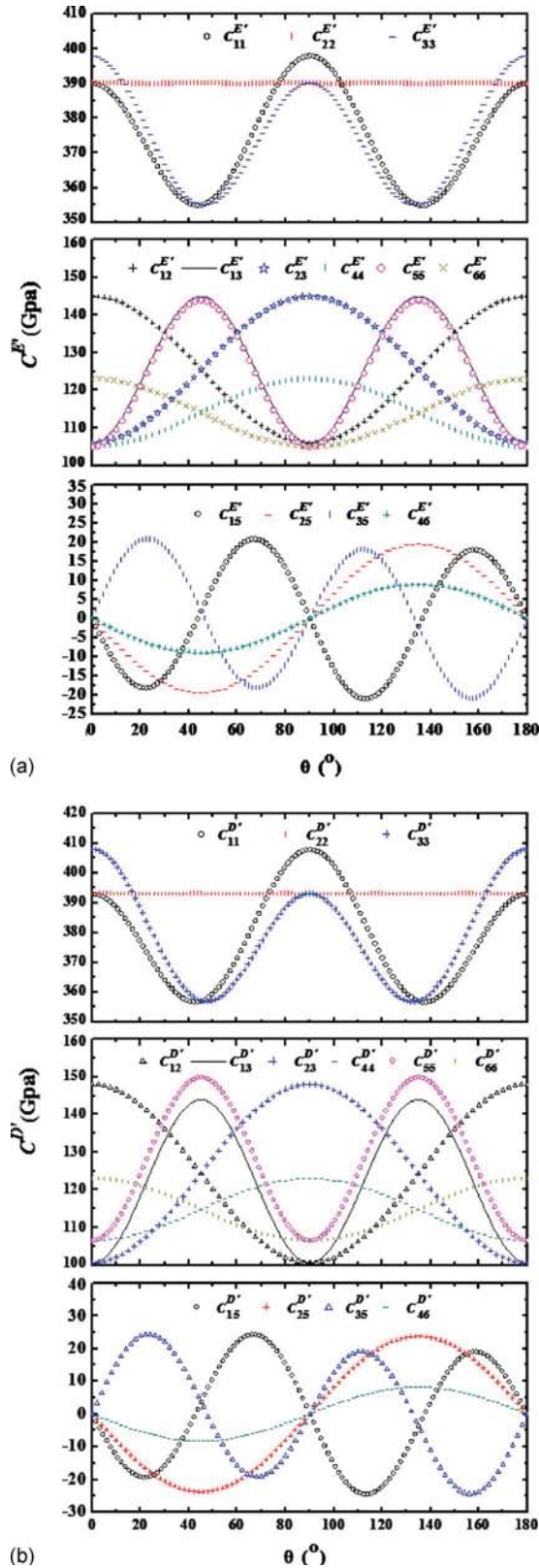
FIG. 2. (Color online) The elastic constants of wurtzite GaN thin film as a function of tilt angle: (a) $c^{E'}$ and (b) $c^{D'}$.
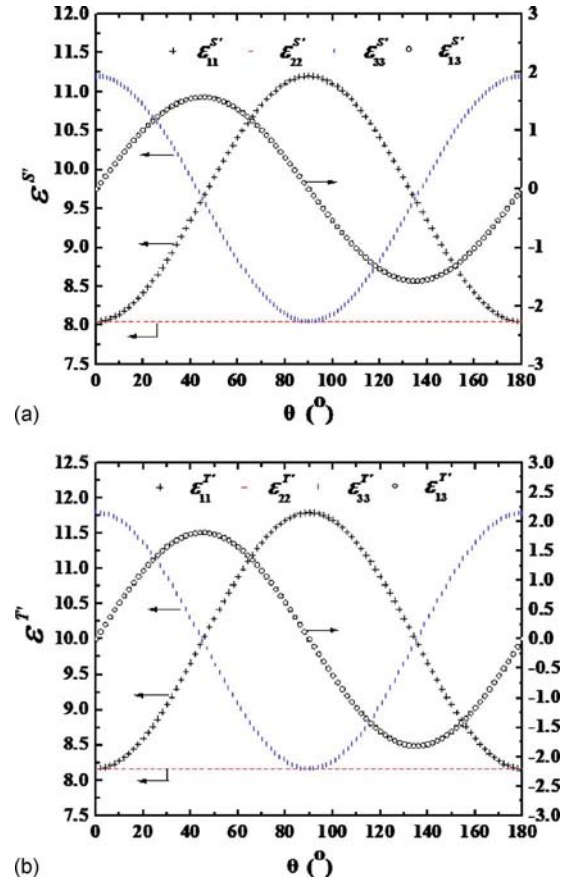

FIG. 3. (Color online) The dielectric constants of wurtzite GaN thin film as a function of tilt angle: (a)$\varepsilon_{33}^{S'}$ and (b) $\varepsilon_{33}^{T'}$.

culate two type elastic constants $c^{E'}$ and $c^{D'}$ shown in Fig. 2. $c^{E'}$ is the elastic stiffness constant under constant electric field intensity, and $c^{D'}$ is the elastic stiffness constant under constant electric displacement. When θ changes from 0° to 180°, 6 by 6 matrix $c^{E'}$ and $c^{D'}$ keeps symmetric with $c_{14}^{E'}$

$=c_{24}^{E'}=c_{34}^{E'}=c_{16}^{E'}=c_{26}^{E'}=c_{36}^{E'}=c_{56}^{E'}=c_{45}^{E'}=0$ and $c_{14}^{D'}=c_{24}^{D'}=c_{34}^{D'}$ $=c_{16}^{D'}=c_{26}^{D'}=c_{36}^{D'}=c_{56}^{D'}=c_{45}^{D'}=0$. From Fig. 2, it can be seen that $c_{22}^{E'}$ and $c_{22}^{D'}$ do not change with the tilt angle, which can be explained by the fact x_2 and x_2' are the same axis. However, the other nonzero elastic constants are strongly dependant on the tilt angle. For example, $c_{11}^{E'}$, $c_{11}^{D'}$, $c_{33}^{E'}$, and $c_{33}^{D'}$ are symmetric about $\theta=90°$, decrease at first, and increase when θ is over 45°.

The two calculated dielectric constants $\varepsilon^{S'}$ and $\varepsilon^{T'}$, the dielectric constant under constant strain and under constant stress, keep symmetric as 3×3 matrixes for $0° \leq \theta \leq 180°$, and the nonzero items are shown in Fig. 3. Similar with dielectric constant, $\varepsilon_{22}^{S'}$ and $\varepsilon_{22}^{T'}$ keep constant because x_2' does not change with θ. On the contrary, other dielectric constants show great dependency on tilt angle. The variation in $\varepsilon_{11}^{S'}$ or $\varepsilon_{11}^{T'}$ with θ has an opposite trend with $\varepsilon_{33}^{S'}$ or $\varepsilon_{33}^{T'}$. $\varepsilon_{11}^{S'}$ or $\varepsilon_{11}^{T'}$ has a maximum value at $\theta=90°$ and a minimum value at $\theta=0°$, while $\varepsilon_{33}^{S'}$ or $\varepsilon_{33}^{T'}$ has a same maximum value at $\theta=0°$ and a same minimum value at $\theta=90°$. This is attributed to the fact that axis x_1' becomes x_3 and x_3' coincides with negative x_1 when θ is equal to 90°.

The piezoelectric strain constant d' (3×6 matrix) and piezoelectric stress constant e' (3×6 matrix) also behavior a strong dependency on tilt angle, and the nonzero constants are shown in Figs. 4 and 5.

FIG. 4. (Color online) The piezoelectric strain constants (d') of wurtzite GaN thin film as a function of tilt angle.
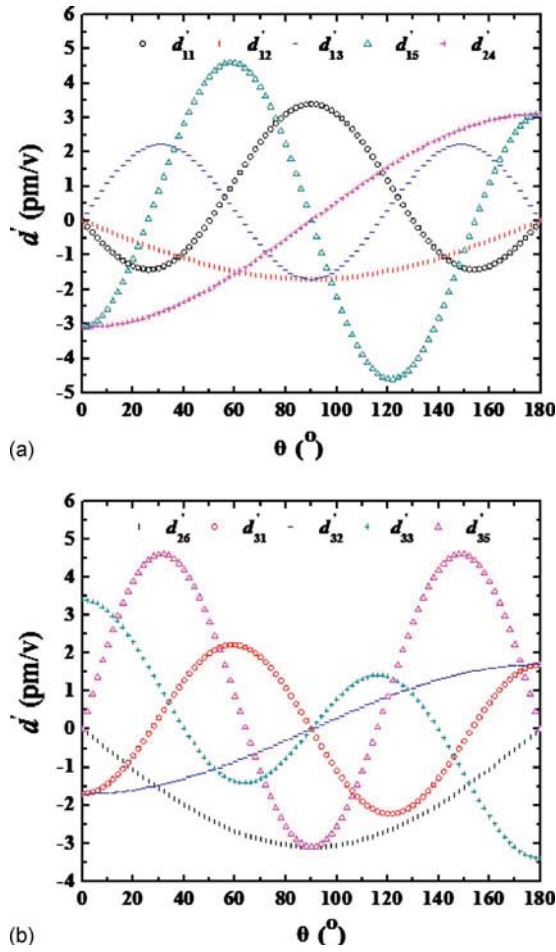

FIG. 5. (Color online) The piezoelectric stress constants (e') of wurtzite GaN thin film as a function of tilt angle.

B. Bulk acoustic wave properties o wurtzite GaN

Acoustic velocity and electromechanical coupling coefficient are two important parameters for FBAR design. Figures 6 and 7 show the calculated acoustic velocity and electromechanical coupling coefficient of GaN thin films for longitudinal and shear mode. The longitudinal velocity ($v^{(L)}$) is found in the range of 7598–8145 m/s, which is larger than shear velocity ($v^{(S)}$) range 4132–4899 m/s. On the contrary, longitudinal electromechanical coupling coefficient (k_L^2) varies from 0% to 2.44%, which is smaller than shear electromechanical coupling coefficient (k_S^2) range 0% to 3.18%. Based on the impedance expression of FBAR, the resonator could be operated in a single mode when a tilt angle makes $k_L=0$ (pure shear mode) or $k_S=0$ (pure longitudinal mode). Table II summarizes the results for some special angles: the pure longitudinal mode occurred at $\theta=0°$ and 66.4°, and the pure shear mode occurs at $\theta=42.8°$ and 90°. The electromechanical coupling coefficient of shear mode has a maximum value 3.18% at $\theta=34.2°$, which is larger than the maximum value of longitudinal mode 2.44% at $\theta=0°$. With the development of modern mobile communication systems, filters with wider bandwidth are greatly needed, which requires higher electromechanical coupling coefficient of piezoelectric material for FBAR based filters. Hence, compared with
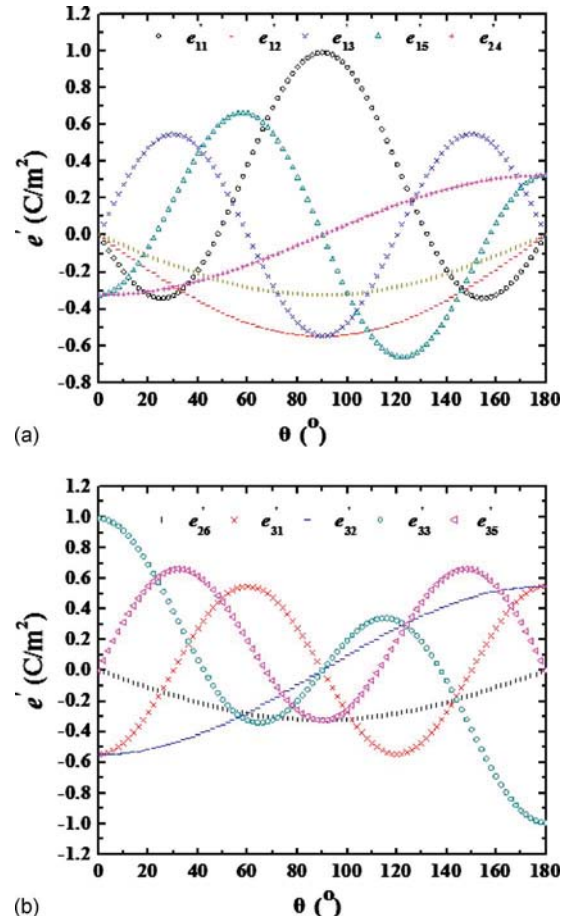
(k_L^2) up to 2.44% ($\theta=0°$), the higher value of k_S^2 up to 3.18% ($\theta=34.2°$) can provide a better choice for the design of higher bandwidth filter.

C. Simulation of electric impedance spectrum of FBAR based on wurtzite GaN

Based on the one dimension impedance equation, the electric impedance spectrum of FBAR can be simulated. Table III lists the parameters used in the simulation. Figure 8 shows the calculated impedance spectra of GaN FBARs with different tilt angle. It can be seen that there are two resonance peaks for most angles. The first peak is shear resonance, and the second one is longitudinal resonance. The resonance frequencies of longitudinal and shear modes are about in the range of 1.9 GHz to 2.0 GHz, and 1 GHz to 1.2 GHz, respectively. As mentioned before, the appearance of strong shear resonance for some certain tilt angles makes GaN FBARs possible for sensor application in liquid. Considering that low electromechanical coupling coefficient of shear mode may lead to deterioration of resonator operation in liquid,[11] pure shear mode produced at 42.8° and 90° with good electromechanical coupling coefficient is the best choice for FBAR operation in liquid application.
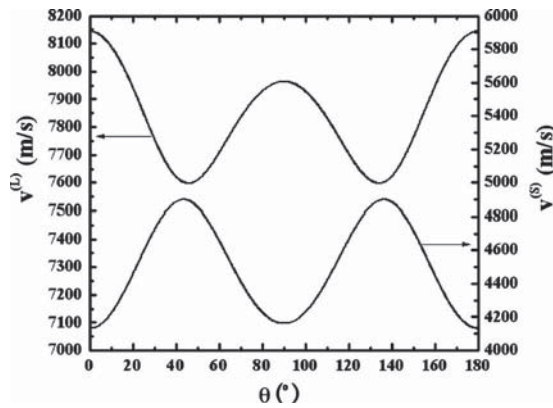
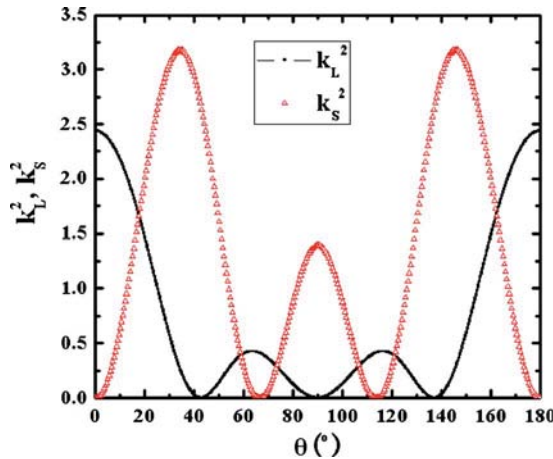FIG. 6. Acoustic velocities of wurtzite GaN thin film as function of tilt angle.

FIG. 7. (Color online) Electromechanical coupling coefficients of wurtzite GaN thin film as function of tilt angle.

TABLE II. Bulk acoustic wave properties of wurtzite GaN.

Tilt angle (°)	Mode	Velocity (m/s)		Electromechanical coupling coefficient (%)	
		v_L	v_S	$(k_L)^2$	$(k_S)^2$
0.0	Pure longitudinal	8145	4132	2.44	0
34.2	Quasi shear and longitudinal	7691	4809	0.27	3.18(max)
42.8	Pure shear	7605	4899	0	2.65
66.4	Pure longitudinal	7789	4503	0.41	0
90.0	Pure shear	7963	4161	0	1.40

(a)

(b)

FIG. 8. (Color online) Simulation of impedance spectrum of FBAR based on *c*-axis tilted wurtzite GaN thin film (S: shear mode, L: longitudinal mode).

TABLE III. Parameters used in impedance simulation.

Piezoelectric layer	Density	Thickness	Electrode area	Mechanical quality factor of longitudinal mode	Mechanical quality factor of shear mode
Wurtzite GaN	6150 kg/m³	2 μm	300×300 μm²	1000	1000

IV. CONCLUSIONS

In summary, FBARs based on wurtzite GaN thin films have been theoretically studied. It is found that the acoustic velocity, electromechanical coupling coefficient, and impedance spectra of FBARs are greatly dependant on the *c*-axis orientation. Strong shear resonant peak is found at special tilt angle. At $\theta = 34.2°$, the electromechanical coefficient of shear mode has a maximum value 3.18%; at $\theta = 42.8°$ and 90°, resonator can be operated in pure shear mode. These special tilt angles with high shear electromechanical coupling coefficient provide more opportunities for FBAR filter design and sensor application in liquid.

ACKNOWLEDGMENTS

[1] K. M. Lakin, G. R. Kline, R. S. Ketcham, and S. G. Burns, Proc.-IEEE Ultrason. Symp. **1986**, 371.

[2] K. M. Lakin, Proc.-IEEE Ultrason. Symp. **2**, 895 (1999).

[3] R. Weigel, D. P. Morgan, J. M. Owens, A. Ballato, K. M. Lakin, K. Hashimoto, and C. C. W. Ruppel, IEEE Trans. Microwave Theory Tech. **50**, 738 (2002).

[4] M. Ylilammi, J. Ella, M. Partanen, and J. Kaitila, IEEE Trans. Ultrason. Ferroelectr. Freq. Control **49**, 535 (2002).

[5] H. P. Löbl, M. Klee, R. Milsom, R. Dekker, C. Metzmacher, W. Brand, and P. Lok, J. Eur. Ceram. Soc. **21**, 2633 (2001).

[6] J. W. Grate, S. J. Martin, and R. M. White, Anal. Chem. **65**, 940A (1993).

[7] J. W. Grate, S. J. Martin, and R. M. White, Anal. Chem. **65**, 987A (1993).

[8] M. Benetti, D. Cannatà, and F. Di Pietrantonio, Appl. Phys. Lett. **87**, 173504 (2005).

[9] G. Wingqvist, J. Bjurström, A.-C. Hellgren, and I. Katardjiev, Sens. Actuators B **127**, 248 (2007).

[10] J. Bjurström, G. Wingqvist, and I. Katardjiev, IEEE Trans. Ultrason. Ferroelectr. Freq. Control **53**, 2095 (2006).

[11] G. Wingqvist, J. Bjurström, L. Liljeholm, V. Yantchev, and I. Katardjiev, Sens. Actuators B **123**, 466 (2007).

[12] F. Martin, M.-E. Jan, S. Rey-Mermet, B. Belgacem, D. Su, M. Cantoni, and P. Muralt, IEEE Trans. Ultrason. Ferroelectr. Freq. Control **53**, 1339 (2006).

[13] F. Martin, M.-E. Jan, B. Belgacem, M.-A. Dubois, and P. Muralt, Thin Solid Films **514**, 341 (2006).

[14] C.-J. Chung, Y.-C. Chen, C.-C. Cheng, and K.-S. Kao, IEEE Trans. Ultrason. Ferroelectr. Freq. Control **55**, 857 (2008).

[15] S. C. Jain, M. Willander, J. Narayan, and R. Van Overstraeten, J. Appl. Phys. **87**, 965 (2000).

[16] S. N. Mohammad, A. A. Salvador, and H. Morkoc, Proc. IEEE **83**, 1306 (1995).

[17] R. F. Davis, S. Einfeldt, E. A. Preble, A. M. Roskowski, Z. J. Reitmeier, and P. Q. Miraglia, Acta Mater. **51**, 5961 (2003).

[18] A. Müller, D. Neculoiu, G. Konstantinidis, A. Stavrinidis, D. Vasilache, A. Cismaru, M. Danila, M. Dragoman, G. Deligeorgis, and K. Tsagaraki, IEEE Electron Device Lett. **30**, 799 (2009).

[19] P. Waltereit, O. Brandt, A. Trampert, H. T. Grahn, J. Menniger, M. Ramsteiner, M. Reiche, and K. H. Ploog, Nature (London) **406**, 865 (2000).

[20] H. F. Tiersten, *Linear Piezoelectric Plates Vibrations* (Plenum, New York, 1969).

[21] N. F. Foster, G. A. Coquin, G. A. Rozgonyi, and F. A. Vannatta, IEEE Trans. Sonics Ultrason. **15**, 28 (1968).

[22] A. Polian, M. Grimsditch, and I. Grzegory, J. Appl. Phys. **79**, 3343 (1996).

[23] S. Muensit, Ph.D. thesis, Macquarie University, 1999.

[24] P. Zapol, R. Panddey, and J. Gale, J. Phys.: Condens. Matter **9**, 9517 (1997).

Analytical Study of Dual-Mode Thin Film Bulk Acoustic Resonators (FBARs) Based on ZnO and AlN Films With Tilted c-Axis Orientation

Lifeng Qin, *Member, IEEE*, Qingming Chen, Hongbin Cheng, and Qing-Ming Wang, *Member, IEEE*

Abstract—In this paper, we present the analytical study of thin film bulk acoustic wave resonators (FBARs) using ZnO and AlN films with a c-axis tilt angle (off-normal) from 0° to 180°. The tilted c-axis orientation induces normal plane and in-plane polarizations, which leads to the coexistence of the longitudinal mode and shear mode in the resonator. The equation for predicting electric impedance of FBARs was derived from the basic piezoelectric constitutive equations. Material properties including elastic, dielectric, and piezoelectric coefficients, bulk wave properties including acoustic velocity and electromechanical coupling coefficient, and impedance of FBARs were calculated and showed strong dependence on the tilt angle. Interestingly, it was found that for ZnO FBARs, pure thickness longitudinal modes occur at 0° and 65.4°, and pure thickness shear modes occur at 43° and 90°. For AlN FBARs, pure longitudinal modes occur at 0° and 67.1°, and pure shear modes occur at 46.1° and 90° for AlN. In other words, pure thickness longitudinal and shear modes exist in ZnO and AlN FBARs at specific tilted polarization angles. In addition, two peaks of shear mode electromechanical coefficient are found at 33.3° and 90° for ZnO, and 34.5° and 90° for AlN. Therefore, ZnO and AlN films with specific tilt angles may provide options in the design and fabrication of FBARs, considering their strong shear resonance with high electromechanical coefficients. The use of dual-mode FBARs for mass sensors is also analyzed; the calculated large resonant frequency shift caused by mass loading shows that they have good prospects for use in sensor applications with high sensitivity. The simulation results agreed well with the reported experiment results, and can be used for design and application of FBARs.

I. Introduction

RECENTLY, in the RF and microwave frequency control and signal processing fields, thin film bulk acoustic wave resonators (FBARs) have received great attention because of their small size, low insertion loss, and low power consumption [1]–[5]. For example, filters based on AlN FBARs which can be operated in the low and medium gigahertz range have been fabricated for signal processing and communication devices [6]–[8]. Also, FBARs show good prospects for sensor applications. Gabl *et al.*

presented a biosensor system based on 2-GHz longitudinal-mode ZnO FBARs for DNA and protein molecule detection; these sensors showed much higher sensitivity than quartz crystal microbalances (QCMs) because of substantially higher resonant frequencies of FBARs [9]. Zhang *et al.* investigated the effects of liquid nature and conductivity on ZnO FBARs, and TiO_2-coated ZnO FBARs with high mass sensitivity were fabricated for metal ion K^+ detection in a liquid environment [10]. Benetti *et al.* reported a chemical sensor based on AlN FBARs with resonance frequency around 1.6 GHz, which was used to detect low concentrations of H_2, CO, and ethanol with a fast and repeatable response [11].

However, for sensor applications in liquid, the performance of thickness longitudinal-mode FBARs will be adversely affected because the acoustic wave energy is radiated into liquid through compressional motion, resulting in excessive damping of the resonator [12]. On the other hand, shear acoustic waves do not produce compressional motion and thus are relatively undamped by liquid. Therefore, shear mode is a preferred choice for liquid operation of FBAR, like the operation of a QCM [13]. Now it must be determined what kind of AlN or ZnO thin films can excite the shear mode.

In recent studies, it has been shown that thickness shear mode resonance can be excited in piezoelectric thin films with tilted c-axis (polarization off-normal) orientations. Foster *et al.* theoretically and experimentally analyzed the excitation of longitudinal and shear wave in a ZnO transducer, which showed the shear-wave excitation greatly exceeded the longitudinal wave excitation when the c-axis was inclined at angles near 40° [14]. Wittstruck *et al.* reported the fabrication of the $Mg_xZn_{1-x}O$ through metal organic chemical vapor deposition (MOCVD); the c-axis of the $Mg_xZn_{1-x}O$ film was lying in the plane surface, providing a possibility for thickness shear wave sensing in a liquid environment [15]. Yanagitani *et al.* reported pure thickness shear-mode FBARs made of (10$\bar{1}$0) and (11$\bar{2}$0) textured ZnO films [16], [17]. Link *et al.* fabricated solidly mounted FBARs using 18° c-axis inclined ZnO thin films; mechanical quality factors of 192 were determined in water, indicating these devices are attractive for sensing applications in liquids [18]. Wu *et al.* theoretically analyzed bulk acoustic wave properties of all crystalline plane oriented sputtered and epitaxial ZnO films using the Christoffel equation; it showed that ZnO films with different

L. Qin, H. Cheng, and Q.-M. Wang are with the Department of Mechanical Engineering, University of Pittsburgh, Pittsburgh, PA (e-mail: qmwang@engr.pitt.edu).

Q. Chen is with the School of Materials and Metallurgical Engineering, Kunming University of Science and Technology, Kunming, Yunnan, P.R. China.

crystalline plane orientation formed different acoustic wave modes and properties [19].

In the case of AlN, Bjurström and Wingqvist *et al.* deposited c-axis tilted AlN films by reactive magnetron sputter deposition system. The variation of the electromechanical coupling and the quality factor of the resonators with tilt angle were examined and a dual-mode FBAR with a micro-fluidic transport system was constructed to investigate the device performance in liquid [20]–[23]. Martin *et al.* presented solidly mounted FBARs based on c-axis tilted AlN films; the resonant frequencies of resonators could be high, up to around 8 GHz for longitudinal mode and 4 GHz for shear mode [24], [25]. Chuang *et al.* fabricated solidly mounted dual-mode FBARs using 0°, 15°, and 30° c-axis tilted AlN films, and experimentally investigated the effect of mass loading on the resonators [26]. Chen *et al.* analyzed the input impedance of a dual-mode AlN FBAR by ignoring the coupling of longitudinal and shear mode, which showed the coexistence of dual mode was dependent on the tilt angle [27].

In this paper, we present the theoretical analysis of thickness longitudinal and thickness shear dual-mode FBARs based on c-axis tilted ZnO and AlN films. Following a similar procedure [14], the equation for predicting electric impedance of FBARS was derived by the basic piezoelectric equations. The material properties including elastic, dielectric, and piezoelectric constants were calculated with a tilt angle range from 0° to 180°, which were used to determine the bulk wave properties of films including acoustic velocity and electromechanical coupling coefficient. Interestingly, it is found that pure thickness longitudinal and pure thickness shear modes occur in the c-axis tilted AlN and ZnO thin film resonators at specific tilt angles. The maximum thickness shear mode electromechanical coefficients are found at 33.3° and 90° for ZnO, and 34.5° and 90° for AlN FBARs. The response of dual-mode resonators were analyzed and compared with reported experiment results. In addition, the sensitivity of FBAR mass sensors are analyzed by considering the effect of a thin layer of mass loading on the frequency shift of the resonators. The analytical and simulation results indicate that high sensitivity can be obtained when the dual-mode FBARs are used for sensor applications.

II. THEORY

A. Dual-Mode FBARs

Fig. 1(a) shows the schematic of tilted c-axis ZnO or AlN FBARs, where the top and bottom electrode are ignored. A rectangular Cartesian coordinate system (x_1', x_2', x_3') was chosen with top electrode on $x_3' = h$ and bottom electrode on $x_3' = 0$. The c-axis of ZnO or AlN films is tilted at an angle θ to the x_3' direction. Fig. 1(b) shows the c-axis normal coordinate (x_1, x_2, x_3). Coordinate system (x_1', x_2', x_3') can be treated as the result of rotation of (x_1, x_2, x_3) about x_2 with an angle θ, as shown in Fig. 1(c).
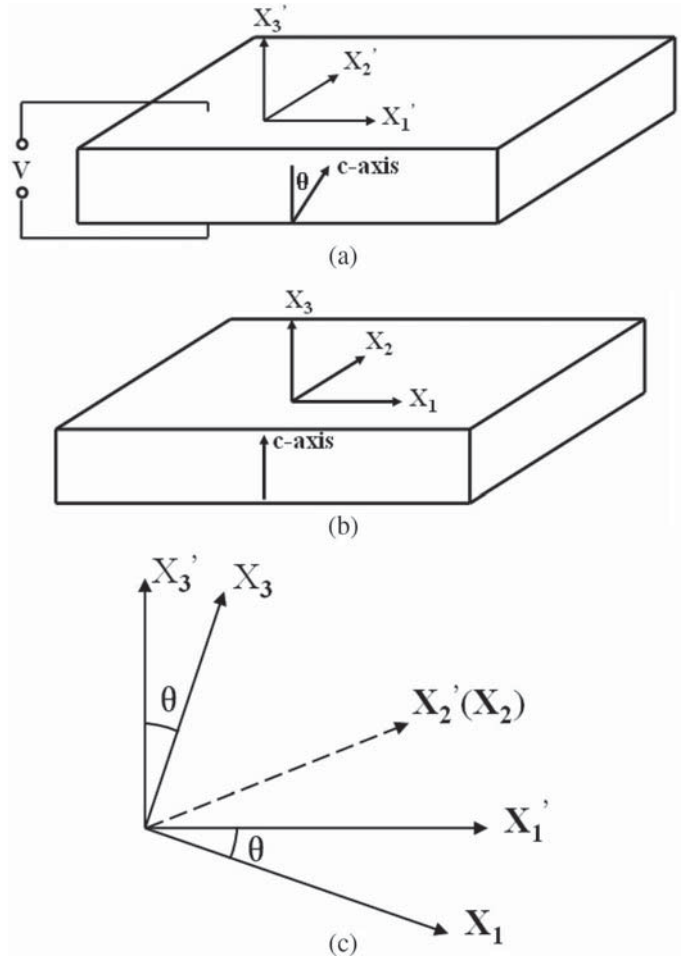

Fig. 1. The schematic of FBAR and coordinate systems. (a) Schematic of FBAR and (x_1', x_2', x_3') coordinate system; (b) (x_1, x_2, x_3) coordinate system; (c) the relation between the (x_1', x_2', x_3') and (x_1, x_2, x_3) coordinate systems.

B. Material Properties of ZnO and AlN Films

For the characterization of tilted c-axis ZnO or AlN FBARs, the material properties in (x_1', x_2', x_3') need to be known. Assuming the dielectric permittivity, piezoelectric stress coefficient, and elastic stiffness are (ε', e', c') for coordinate system (x_1', x_2', x_3'), and (ε, e, c) for coordinate system (x_1, x_2, x_3), the material properties in new coordinate system can be computed through properties in original coordinate system with the aid of matrix algebra [28]:

$$\varepsilon' = a\varepsilon a^{\mathrm{t}} \tag{1}$$

$$e' = aeM^{\mathrm{t}} \tag{2}$$

$$c' = McM^{\mathrm{t}} \tag{3}$$

$$a = \begin{bmatrix} a_{11} & a_{12} & a_{13} \\ a_{21} & a_{22} & a_{23} \\ a_{31} & a_{32} & a_{33} \end{bmatrix} = \begin{bmatrix} \cos(\theta) & 0 & \sin(\theta) \\ 0 & 1 & 0 \\ -\sin(\theta) & 0 & \cos(\theta) \end{bmatrix} \tag{4}$$

and (5), see next page, where θ is the tilt angle, a^{t} is the transpose of a, and M^{t} is the transpose of M.

$$M = \begin{bmatrix} a_{11}^2 & a_{12}^2 & a_{13}^2 & 2a_{12}a_{13} & 2a_{11}a_{13} & 2a_{11}a_{12} \\ a_{21}^2 & a_{22}^2 & a_{23}^2 & 2a_{22}a_{23} & 2a_{21}a_{23} & 2a_{21}a_{22} \\ a_{31}^2 & a_{32}^2 & a_{33}^2 & 2a_{32}a_{33} & 2a_{31}a_{33} & 2a_{31}a_{32} \\ a_{21}a_{31} & a_{22}a_{32} & a_{23}a_{33} & a_{22}a_{33} + a_{23}a_{32} & a_{21}a_{33} + a_{23}a_{31} & a_{21}a_{32} + a_{22}a_{31} \\ a_{11}a_{31} & a_{12}a_{32} & a_{13}a_{33} & a_{12}a_{33} + a_{13}a_{32} & a_{11}a_{33} + a_{13}a_{31} & a_{11}a_{32} + a_{12}a_{31} \\ a_{11}a_{21} & a_{12}a_{22} & a_{13}a_{23} & a_{12}a_{23} + a_{13}a_{22} & a_{11}a_{23} + a_{13}a_{21} & a_{11}a_{22} + a_{12}a_{21} \end{bmatrix} \tag{5}$$

C. Electric Impedance of FBARs

According to the acoustic field equations and piezoelectric constitution equations [28], [29], we have:

$$\begin{bmatrix} \dfrac{\partial}{\partial x_1'} & 0 & 0 & 0 & \dfrac{\partial}{\partial x_3'} & \dfrac{\partial}{\partial x_2'} \\ 0 & \dfrac{\partial}{\partial x_2'} & 0 & \dfrac{\partial}{\partial x_3'} & 0 & \dfrac{\partial}{\partial x_1'} \\ 0 & 0 & \dfrac{\partial}{\partial x_3'} & \dfrac{\partial}{\partial x_2'} & \dfrac{\partial}{\partial x_1'} & 0 \end{bmatrix} \begin{bmatrix} T_1 \\ T_2 \\ T_3 \\ T_4 \\ T_5 \\ T_6 \end{bmatrix} = \rho \begin{bmatrix} \dfrac{\partial^2 u_1}{\partial t^2} \\ \dfrac{\partial^2 u_2}{\partial t^2} \\ \dfrac{\partial^2 u_3}{\partial t^2} \end{bmatrix} \tag{6}$$

$$\begin{bmatrix} S_1 \\ S_2 \\ S_3 \\ S_4 \\ S_5 \\ S_6 \end{bmatrix} = \begin{bmatrix} \dfrac{\partial}{\partial x_1'} & 0 & 0 \\ 0 & \dfrac{\partial}{\partial x_2'} & 0 \\ 0 & 0 & \dfrac{\partial}{\partial x_3'} \\ 0 & \dfrac{\partial}{\partial x_3'} & \dfrac{\partial}{\partial x_2'} \\ \dfrac{\partial}{\partial x_3'} & 0 & \dfrac{\partial}{\partial x_1'} \\ \dfrac{\partial}{\partial x_2'} & \dfrac{\partial}{\partial x_1'} & 0 \end{bmatrix} \begin{bmatrix} u_1 \\ u_2 \\ u_3 \end{bmatrix} \tag{7}$$

$$T_p = c_{pq}^{E\,'} S_q - e_{kp}' E_k \tag{8}$$

$$D_i = e_{iq}' S_q + \varepsilon_{ik}^{S\,'} E_k, \tag{9}$$

where T_p, S_q, D_i, and E_k are the components of stress, strain, electric displacement, and electric field intensity, $c_{pq}^{E\,'}$ are the elastic stiffness constants under constant electric field intensity, e_{kp}' are the piezoelectric stress constants, $\varepsilon_{ik}^{S\,'}$ are the permittivity constants under constant strain, and u_i is the displacement in the direction of x_i' (i, $k = 1, 2, 3$; p, $q = 1, 2, 3, 4, 5, 6$). Because the thickness of the piezoelectric layer is much smaller than the lateral dimensions, the thickness vibration of the resonator can be treated as a one-dimensional problem; hence, we may have:

$$\frac{\partial T_i}{\partial x_1'} = \frac{\partial T_i}{\partial x_2'} = 0 \tag{10a}$$

$$E_1 = E_2 = 0, \quad E_3 \neq 0 \tag{10b}$$

$$\frac{\partial D_3}{\partial x_3'} = 0. \tag{11}$$

From (6)–(10), we can obtain:

$$T_4 = c_{44}^{E\,'} \frac{\partial u_2}{\partial x_3'} + c_{34}^{E\,'} \frac{\partial u_3}{\partial x_3'} + c_{45}^{E\,'} \frac{\partial u_1}{\partial x_3'} - e_{34}' E_3 \tag{12}$$

$$\frac{\partial T_4}{\partial x_3'} = \rho \frac{\partial^2 u_2}{\partial t^2} \tag{13}$$

$$T_5 = c_{55}^{E\,'} \frac{\partial u_1}{\partial x_3'} + c_{35}^{E\,'} \frac{\partial u_3}{\partial x_3'} + c_{45}^{E\,'} \frac{\partial u_2}{\partial x_3'} - e_{35}' E_3 \tag{14}$$

$$\frac{\partial T_5}{\partial x_3'} = \rho \frac{\partial^2 u_1}{\partial t^2} \tag{15}$$

$$T_3 = c_{33}^{E\,'} \frac{\partial u_3}{\partial x_3'} + c_{35}^{E\,'} \frac{\partial u_1}{\partial x_3'} + c_{34}^{E\,'} \frac{\partial u_2}{\partial x_3'} - e_{33}' E_3 \tag{16}$$

$$\frac{\partial T_3}{\partial x_3'} = \rho \frac{\partial^2 u_3}{\partial t^2} \tag{17}$$

$$D_3 = e_{35}' \frac{\partial u_1}{\partial x_3'} + e_{34}' \frac{\partial u_2}{\partial x_3'} + e_{33}' \frac{\partial u_3}{\partial x_3'} + \varepsilon_{33}^{S\,'} E_3. \tag{18}$$

For any tilt angle θ, it is found that

$$c_{34}^{E\,'} = c_{45}^{E\,'} = e_{34}' = 0. \tag{19}$$

Using (12), (13), and (19), we get $u_2 = 0$. Substituting (14) into (15) and substituting (16) into (17), we have:

$$\overline{c_{55}^{E\,'}} \frac{\partial^2 u_1}{\partial x_3'^2} + \overline{c_{35}^{E\,'}} \frac{\partial^2 u_3}{\partial x_3'^2} = \rho \frac{\partial^2 u_1}{\partial t^2} \tag{20}$$

$$\overline{c_{33}^{E\,'}} \frac{\partial^2 u_3}{\partial x_3'^2} + \overline{c_{35}^{E\,'}} \frac{\partial^2 u_1}{\partial x_3'^2} = \rho \frac{\partial^2 u_3}{\partial t^2}, \tag{21}$$

where

$$\overline{c_{33}^{E\,'}} = c_{33}^{E\,'} + \frac{(e_{33}')^2}{\varepsilon_{33}^{S\,'}} \tag{22a}$$

$$\overline{c_{35}^{E\,'}} = c_{35}^{E\,'} + \frac{e_{33}'e_{35}'}{\varepsilon_{33}^{S\,'}} \tag{22b}$$

$$\overline{c_{55}^{E\,'}} = c_{55}^{E\,'} + \frac{(e_{35}')^2}{\varepsilon_{33}^{S\,'}}. \tag{22c}$$

For a sinusoidal excitation, the solution to (20) and (21) is given by

$$\begin{bmatrix} u_1 \\ u_3 \end{bmatrix} = \begin{bmatrix} \sin(\alpha) & \cos(\alpha) \\ \cos(\alpha) & -\sin(\alpha) \end{bmatrix} \begin{bmatrix} u_L \\ u_S \end{bmatrix} \tag{23a}$$

$$u_L = \left(A_L \sin(\omega x_3'/v^{(L)}) + B_L \cos(\omega x_3'/v^{(L)})\right)e^{jwt} \tag{23b}$$

$$u_S = \left(A_S \sin(\omega x_3'/v^{(S)}) + B_S \cos(\omega x_3'/v^{(S)})\right)e^{jwt}, \tag{23c}$$

where

$$w = 2\pi f \tag{24a}$$

$$\alpha = \frac{1}{2}\arctan\left(\frac{2\overline{c_{35}^{E\,'}}}{\overline{c_{33}^{E\,'}} - \overline{c_{55}^{E\,'}}}\right) \tag{24b}$$

$$v^{(L)} = \left[\frac{\overline{c_{33}^{E\,'}} + \overline{c_{55}^{E\,'}}}{2\rho} + \sqrt{\left(\frac{\overline{c_{33}^{E\,'}} - \overline{c_{55}^{E\,'}}}{2\rho}\right)^2 + \left(\frac{\overline{c_{35}^{E\,'}}}{\rho}\right)^2}\right]^{1/2} \tag{24c}$$

$$v^{(S)} = \left[\frac{\overline{c_{33}^{E\,'}} + \overline{c_{55}^{E\,'}}}{2\rho} - \sqrt{\left(\frac{\overline{c_{33}^{E\,'}} - \overline{c_{55}^{E\,'}}}{2\rho}\right)^2 + \left(\frac{\overline{c_{35}^{E\,'}}}{\rho}\right)^2}\right]^{1/2}, \tag{24d}$$

f is the frequency, $v^{(L)}$ and $v^{(S)}$ are the acoustic velocities for longitudinal mode and shear mode, respectively, and A_L, B_L, A_S, B_S are the unknown amplitudes determined by the boundary conditions. The stress can be solved through substituting (23) and (24) into (14) and (16), given by

$$\begin{bmatrix} T_5 \\ T_3 \end{bmatrix} = \begin{bmatrix} \sin(\alpha) & \cos(\alpha) \\ \cos(\alpha) & -\sin(\alpha) \end{bmatrix} \begin{bmatrix} T_L \\ T_S \end{bmatrix} \tag{25a}$$

$$T_L = wZ_L\left(A_L\cos(\omega x_3'/v^{(L)}) - B_L\sin(\omega x_3'/v^{(L)})\right)e^{jwt} \\ - \left(\frac{e_L}{\varepsilon_{33}^{S\,'}}\right)D_3 \tag{25b}$$

$$T_S = wZ_S\left(A_S\cos(\omega x_3'/v^{(S)}) - B_S\sin(\omega x_3'/v^{(S)})\right)e^{jwt} \\ - \left(\frac{e_S}{\varepsilon_{33}^{S\,'}}\right)D_3, \tag{25c}$$

where

$$Z_L = \rho v^{(L)} \tag{26a}$$

$$Z_S = \rho v^{(S)} \tag{26b}$$

$$e_L = e_{35}'\sin(\alpha) + e_{33}'\cos(\alpha) \tag{26c}$$

$$e_S = e_{35}'\cos(\alpha) - e_{33}'\sin(\alpha). \tag{26d}$$

The voltage across the piezoelectric layer is found from (11), (18), (26c), and (26d) to be

$$V = \int_0^h E_3 dx_3' \\ = -\frac{e_L}{\varepsilon_{33}^{S\,'}}[u_L(h) - u_L(0)] - \frac{e_S}{\varepsilon_{33}^{S\,'}}[u_S(h) - u_S(0)] + \frac{D_3 h}{\varepsilon_{33}^{S\,'}} \tag{27}$$

where A is the area of the electrodes. The current I can be expressed by

$$I = \frac{dQ}{dt} = wAD_3. \tag{28}$$

The traction force at the boundary $(x_3' = 0, h)$ is zero, thus we have

$$T_5(0) = T_5(h) = T_3(0) = T_3(h) = 0. \tag{29}$$

Using (23), (25), and (29), we find that

$$u_L(h) - u_L(0) = \frac{2e_L D_3 \tan\left(\frac{\omega h}{2v^{(L)}}\right)}{wZ_L\varepsilon_{33}^{S\,'}} \tag{30a}$$

$$u_S(h) - u_S(0) = \frac{2e_S D_3 \tan\left(\frac{\omega h}{2v^{(S)}}\right)}{wZ_S\varepsilon_{33}^{S\,'}}. \tag{30b}$$

Hence, substituting (30) into (27) and using (28), the impedance of FBAR is found to be

$$Z = \frac{V}{I} = \frac{1}{j\omega C_0}\left(1 - k_L^2\frac{\tan(\gamma_L/2)}{\gamma_L/2} - k_S^2\frac{\tan(\gamma_S/2)}{\gamma_S/2}\right) \tag{31}$$

where

$$\gamma_L = \frac{\omega h}{v^{(L)}} \tag{32a}$$

$$\gamma_S = \frac{\omega h}{v^{(S)}} \tag{32b}$$

$$C_0 = \varepsilon_{33}^{S\,'}A/h \tag{32c}$$

$$k_L^2 = \frac{(e_L)^2}{\varepsilon_{33}^{S\,'}\rho\left(v^{(L)}\right)^2} \tag{32d}$$

$$k_S^2 = \frac{(e_S)^2}{\varepsilon_{33}^{S\,'}\rho\left(v^{(S)}\right)^2}. \tag{32e}$$

Here, k_L and k_S are respectively defined as the electromechanical coupling coefficient for the longitudinal and shear modes.

TABLE I. MATERIAL PROPERTIES OF ZnO AND AlN.

Property		AlN	ZnO
Density (kg/cm³)	ρ	3260	5700
Elastic stiffness (Gpa)	c_{11}^E	345	210
$c^E = \begin{bmatrix} c_{11} & c_{12} & c_{13} & 0 & 0 & 0 \\ c_{12} & c_{11} & c_{13} & 0 & 0 & 0 \\ c_{13} & c_{13} & c_{33} & 0 & 0 & 0 \\ 0 & 0 & 0 & c_{44} & 0 & 0 \\ 0 & 0 & 0 & 0 & c_{44} & 0 \\ 0 & 0 & 0 & 0 & 0 & c_{66} \end{bmatrix}$	c_{12}^E	125	121
	c_{13}^E	120	105
	c_{33}^E	395	211
	c_{44}^E	118	43.0
	c_{66}^E	110	44.5
Piezoelectric stress constant (C/m²)	e_{31}	−0.58	−0.57
$e = \begin{bmatrix} 0 & 0 & 0 & 0 & e_{15} & 0 \\ 0 & 0 & 0 & e_{15} & 0 & 0 \\ e_{31} & e_{31} & e_{33} & 0 & 0 & 0 \end{bmatrix}$	e_{33}	1.55	1.32
	e_{15}	−0.48	−0.48
Dielectric permittivity (10^{-11} F/m)	ε_{11}^S	8.0	7.61
$\varepsilon^S = \begin{bmatrix} \varepsilon_{11}^S & 0 & 0 \\ 0 & \varepsilon_{11}^S & 0 \\ 0 & 0 & \varepsilon_{33}^S \end{bmatrix}$	ε_{33}^S	9.5	8.85

III. RESULTS AND DISCUSSION

A. Dependence of ZnO and AlN Properties on the Tilt Angle θ

The material properties of ZnO [30], [31] and AlN [32] in the (x_1, x_1, x_1) coordinate system are listed in Table I. Using (1)–(5), (22), (26c), and (26d), the material properties and effective parameters in (x_1', x_2', x_3') coordinate system are calculated and shown in Figs. 2 and 3, which can clearly show that elastic stiffness, dielectric permittivity, and piezoelectric coefficient are tilt-angle dependent. According to (22), $\overline{c_{33}^{E'}}$ and $\overline{c_{55}^{E'}}$ can be regarded as piezoelectrically stiffened $c_{33}^{E'}$ and $c_{55}^{E'}$, respectively; and have larger values, as shown in Figs. 2(a) and 3(a). The value of $\overline{c_{35}^{E'}}$, as shown in Figs. 2(b) and 3(b), is much smaller compared with $\overline{c_{33}^{E'}}$ and $\overline{c_{55}^{E'}}$, which makes the calculated angle α through (24b) very small, in a range of 0 to 5° shown in Figs. 2(d) and 3(d). α indicates the strength of the coupling between the longitudinal and shear modes. The smaller the value of α is, the weaker is the coupling. The small value of α makes the calculated e_L and e_S through (26) very close to e_{33}' and e_{55}', respectively, which can be clearly seen from Figs. 2(e) and 2(f) and Figs. 3(e) and 3(f). The calculated $\varepsilon_{33}^{S'}$, as shown in Figs. 2(c) and 3(c), varies from 7.61×10^{-11} to 8.85×10^{-11} F/m for ZnO and 8.00×10^{-11} to 9.50×10^{-11} F/m for AlN.

B. Bulk Acoustic Wave Properties of ZnO and AlN

It is necessary to know the acoustic velocity and electromechanical coupling coefficient of ZnO and AlN films with different tilt angle, because they are two important bulk acoustic wave properties for FBAR design. Figs. 4(a) and 5(a) show the acoustic velocity of ZnO and AlN films for longitudinal and shear mode based on (24c) and (24d); Figs. 4(b) and 5(b) show electromechanical coupling coef-

ficient of ZnO and AlN films for longitudinal and shear mode based on (32d) and (32e). The longitudinal and shear velocity of AlN are found in the range of 10 287 to 11 354 m/s and 6016 to 6368 m/s, respectively; for ZnO, the longitudinal and shear velocity are in the range of 5935 to 6362 m/s and 2747 to 3233 m/s, respectively. For most tilt angles, the longitudinal electromechanical coefficient (k_L^2) of ZnO, varying from 0% to 8.53%, is higher than that of AlN, varying from 0 to 6.0%; and the shear electromechanical coefficient (k_S^2) of ZnO, varying from 0 to 13.1%, is higher than that of AlN, varying from 0 to 6.5%.

Based on the electric impedance expression (31), it can be found that the conditions for a single mode is $k_L = 0$ (for pure shear mode) or $k_S = 0$ (for pure longitudinal mode), which corresponds to to $e_L = 0$ or $e_S = 0$ according to (32d) and (32e). The tilt angle for pure modes are numerically solved and summarized in Table II and III, which also include the special tilt angle where the maximum shear electromechanical coupling coefficient occurs. For ZnO, the pure longitudinal mode is excited at $\theta = 0°$ with $k_L^2 = 8.5\%$ and $\theta = 65.4°$ with $k_L^2 = 1.2\%$; the pure shear mode is excited at $\theta = 43°$ with $k_S^2 = 10.4\%$ and $\theta = 90°$ with $k_S^2 = 6.6\%$; and the maximum of electromechanical coupling coefficient for shear mode is 13.1% at $\theta = 33.3°$. For AlN, the pure longitudinal mode is excited at $\theta = 0°$ with $k_L^2 = 6\%$ and $\theta = 67.1°$ with $k_L^2 = 0.6\%$; the pure shear mode is excited at $\theta = 46.1°$ with $k_S^2 = 4.6\%$ and $\theta = 90°$ with $k_S^2 = 2.4\%$; and the maximum of electromechanical coupling coefficient for shear mode is 6.5% at $\theta = 34.5°$.

C. Simulation of Electric Impedance Spectra of FBARs Based on ZnO and AlN Films

It is well known that the mechanical quality factor (Q) of thin films varies with the thin film deposition processing conditions. The reported Q value of ZnO and AlN
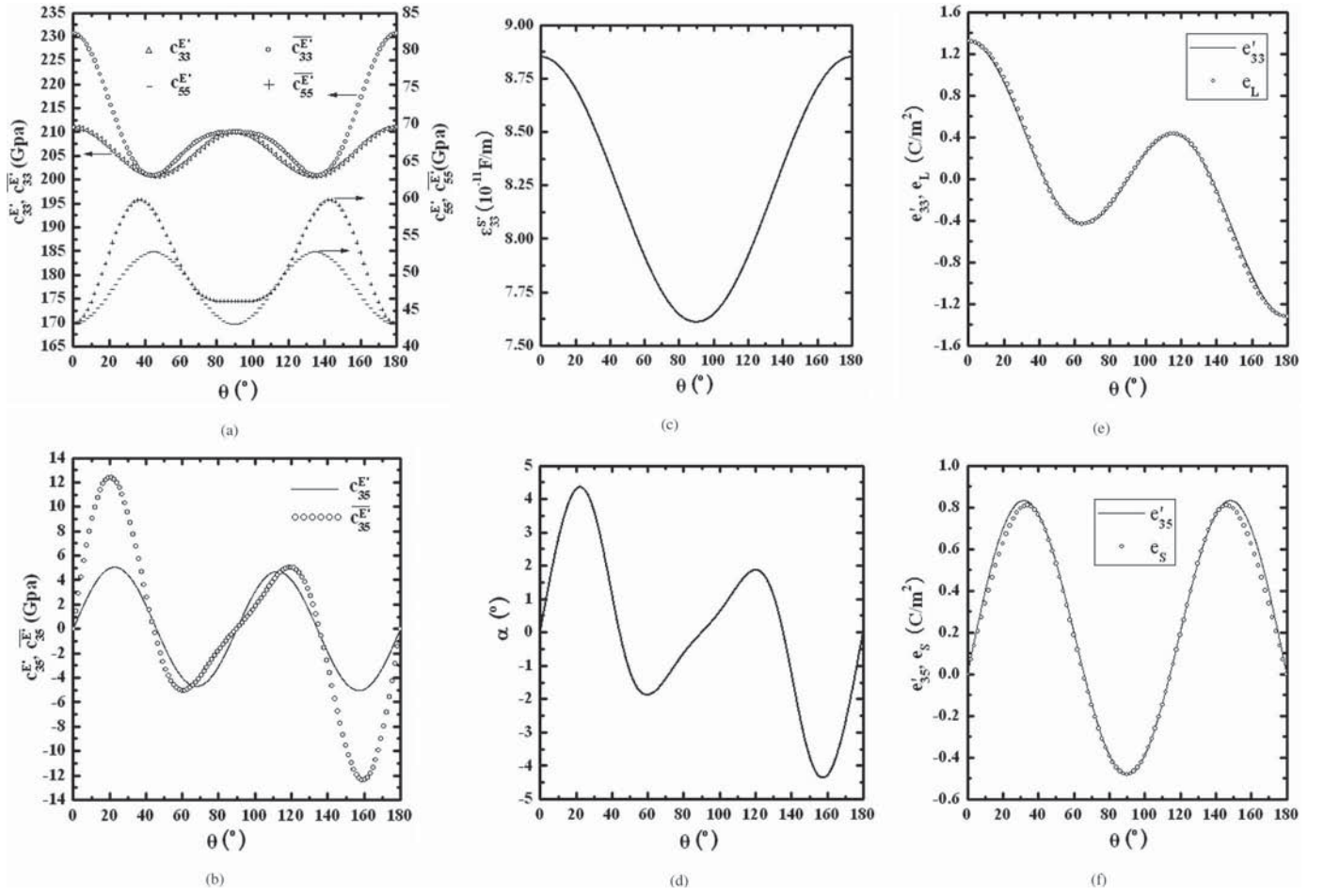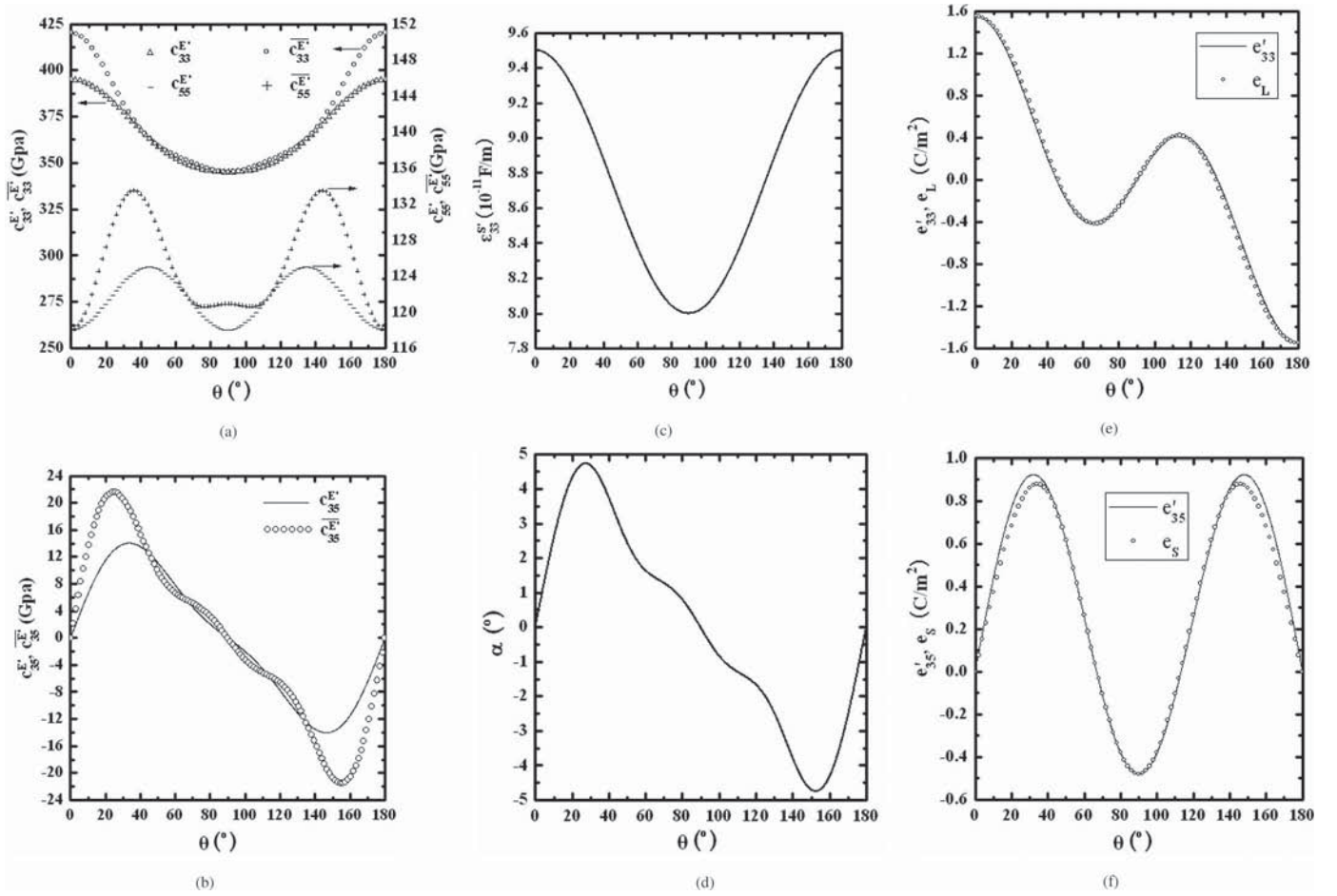
Fig. 2. ZnO material properties and effective parameters in the (x'_1, x'_2, x'_3) coordinate system. (a) $c_{33}^{E'}$, $\overline{c_{33}^{E'}}$, $c_{55}^{E'}$, and $\overline{c_{55}^{E'}}$; (b) $c_{35}^{E'}$ and $\overline{c_{35}^{E'}}$; (c) $\varepsilon_{33}^{S'}$; (d) α; (e) e'_{33} and e_{L}; (f) e'_{35} and e_{S}.

TABLE II. BULK ACOUSTIC WAVE PROPERTIES OF ZnO.

Tilt angle (°)	Mode	Velocity (m/s)		Electromechanical coupling coefficient (%)	
		v_{L}	v_{S}	$(k_{L})^2$	$(k_{S})^2$
0.0	Pure longitudinal	6362	2747	8.5	0
33.3	Quasi shear and longitudinal	5992	3216	1.1	13.1 (max)
43.0	Pure shear	5936	3213	0	10.4
65.4	Pure longitudinal	6028	2916	1.2	0
90.0	Pure shear	6070	2842	0	6.6

TABLE III. BULK ACOUSTIC WAVE PROPERTIES OF AlN.

Tilt angle (°)	Mode	Velocity (m/s)		Electromechanical coupling coefficient (%)	
		v_{L}	v_{S}	$(k_{L})^2$	$(k_{S})^2$
0	Pure longitudinal	11354	6016	6.0	0
34.5	Quasi shear and longitudinal	10749	6363	0.8	6.5 (max)
46.1	Pure shear	10548	6325	0	4.6
67.1	Pure longitudinal	10380	6104	0.6	0
90	Pure shear	10287	6089	0	2.4

Fig. 3. AlN material properties and effective parameters in the (x_1', x_2', x_3') coordinate system. (a) $c_{33}^{E'}$, $\overline{c_{33}^{E'}}$, $c_{55}^{E'}$, and $\overline{c_{55}^{E'}}$; (b) $c_{35}^{E'}$ and $\overline{c_{35}^{E'}}$; (c) $\varepsilon_{33}^{S'}$; (d) α; (e) e_{33}' and e_L; (f) e_{35}' and e_S.

is around several hundred [10], [18], [20], [22]. Here, for simplification, Q_L(mechanical quality factor of longitudinal mode) is assumed to be 350 for ZnO and 400 for AlN; Q_S (mechanical quality factor of shear mode) assumed to be 350 for ZnO and 400 for AlN. Thus, the new acoustic velocity v_L' (longitudinal mode) and v_S' (shear mode) are adopted for impedance calculation when Q_S and Q_L are taken into consideration [33]:

$$v_L' = v_L + j\frac{v_L}{2Q_L} \tag{33a}$$

$$v_S' = v_S + j\frac{v_S}{2Q_S}. \tag{33b}$$

In addition, the thickness of ZnO or AlN films is assumed to be 2 μm and the electrode area is assumed to 9 × 10^{-8} m². Because of symmetry, tilt angle from 0 to 90° is adopted in the simulation. Figs. 6 and 7, respectively, show the calculated impedance spectra of ZnO and AlN FBARs with different tilt angles, where the resonance frequencies of shear and longitudinal mode are fairly separated because of the difference of the acoustic velocities. For ZnO, the resonance frequencies of thickness longitudinal

and shear modes are found in the range of 1.4 to 1.6 GHz and 0.68 to 0.81 GHz, respectively; the ratio of longitudinal and shear resonance frequency varies from 1.84 to 2.32. Link et al. reported that the ratio of longitudinal and shear resonance frequency was around 2.0 for 18° c-axis inclined ZnO thin film [18], which is consistent with our theoretically calculated value 2.09 ($\theta = 18°$). For AlN, the resonance frequencies of thickness longitudinal and shear modes are found in the range of 2.57 to 2.84 GHz and 1.50 to 1.60 GHz, respectively, and the ratio of longitudinal and shear resonance frequency varies from 1.66 to 1.89. For a specific tilt angle ($\theta = 28°$) of AlN, the theoretical value found was 1.726, which agrees well with 1.72 calculated through the experiment result of Wingqvist et al. [23]. For another tilt angle ($\theta = 30°$) of AlN, the theoretical value was found to be 1.713, which was also close to 1.76 calculated by the experimental results of Chuang et al. [26].

It also can be seen from Figs. 6 and 7 that resonance peaks of the spectra are different with the change of tilt angle. Interestingly, besides tilt angle 0° (i.e., normal polarization), a pure thickness longitudinal mode occurs at 65.4° for ZnO and 67.1° for AlN, with smaller electromechanical coefficient. In addition, besides tilt angle 90° (i.e.,
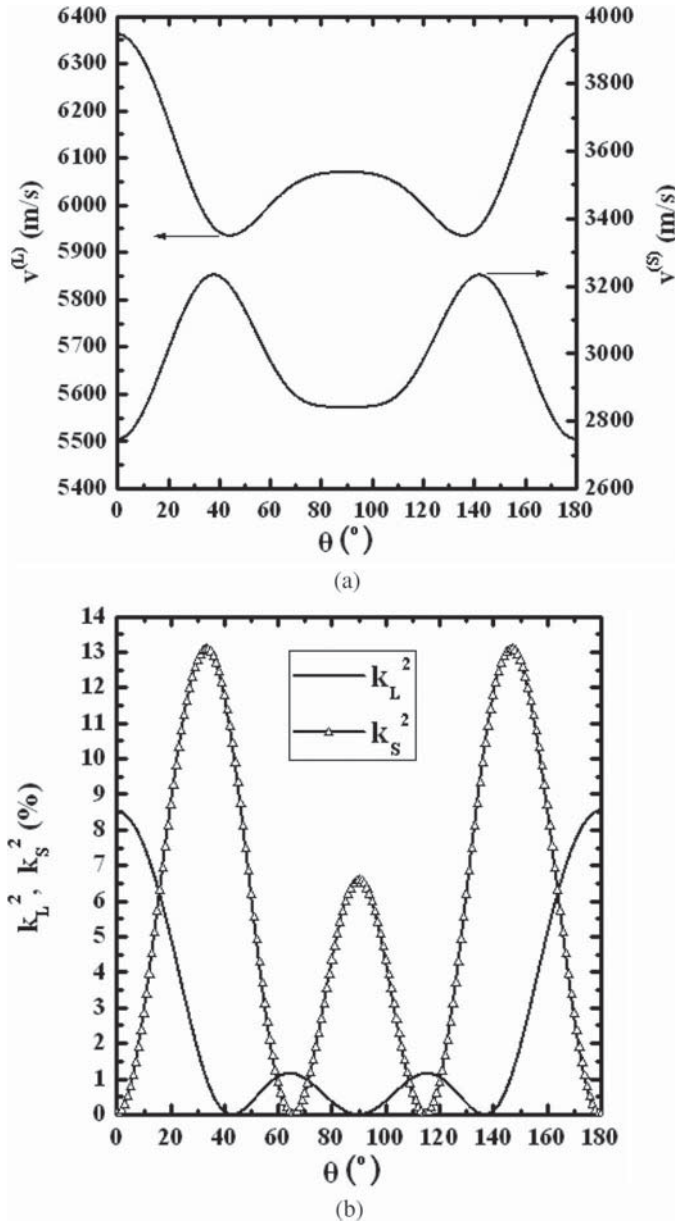
Fig. 4. Bulk acoustic wave properties of ZnO. (a) Acoustic velocity and (b) electromechanical coupling coefficient.

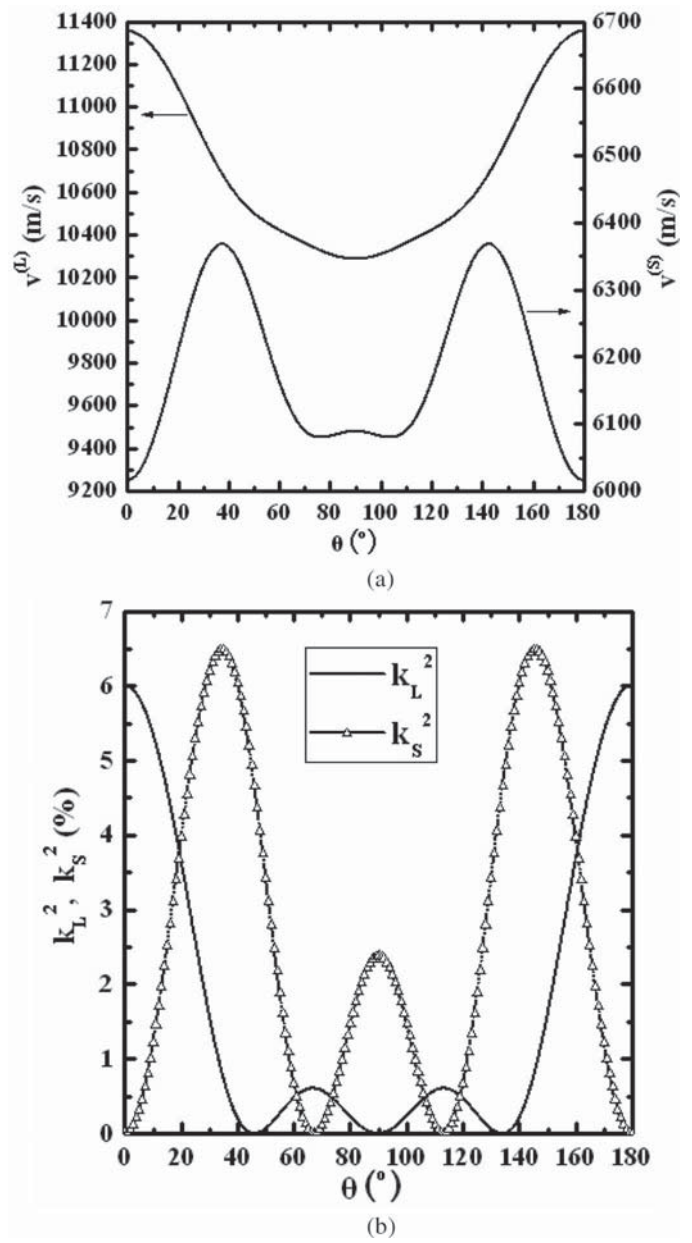
Fig. 5. Bulk acoustic wave properties of AlN. (a) Acoustic velocity and (b) electromechanical coupling coefficient.

in-plane polarization) a pure thickness shear mode occurs at 43° for ZnO and 46.1° for AlN, with higher electromechanical coefficient. The strongest resonance peak of thickness shear mode for ZnO occurs at 33.3°, where the maximum shear mode electromechanical coupling coefficient is found to be 13.1%. For AlN, the strongest resonance peak of thickness shear mode occurs at 34.5°, where the maximum shear mode electromechanical coupling coefficient is found to be 6.5%. From Figs. 4(b) and 5(b), it can also be found that two peaks for k_S^2 exist at tilt angle $\theta = 33.3°, 90°$ for ZnO, and $\theta = 34.5°, 90°$ for AlN. It is noticed that a low electromechanical coupling coefficient of shear mode will lead to deterioration of resonator operation in liquid [23]. Hence, tilt angle close to $33.3°, 90°$ for ZnO films, and $34.5°, 90°$ for AlN films are good options for sensor applications of FBARs in liquid environment. In fact,

Wingqvist *et al.* [23] presented AlN FBARs with a tilt angle around 30°; they showed a strong shear resonance around 1.2 GHz with high Q_S of around 150 in the water, and the viscous load experiments indicated the potential of FBARs for biosensor bioanalytical tools as well as for liquid sensing in general.

D. Sensitivity Analysis of ZnO and AlN FBAR Mass Sensors

When bulk acoustic wave resonators are used for mass sensors such as in the case of the commonly used QCM, it is well known from the Sauerbrey equation that the resonant frequency will change due to surface mass loading [34], [35], $\Delta f = -(2f_0^2 \Delta m)/(A(\mu_q \rho_q)^{1/2})$, where f_0 is

$$p^{\mathrm{L}} = 1 + \frac{\left[e_{\mathrm{L}} \sin^2\left(\frac{\gamma^{\mathrm{L}}}{2}\right)\left(\frac{Z_{\mathrm{sl}}^{\mathrm{L}} Z_{\mathrm{sl}}^{\mathrm{S}}}{Z_{\mathrm{L}} Z_{\mathrm{S}}} \cos(\gamma^{\mathrm{S}}) + j \frac{Z_{\mathrm{sl}}^{\mathrm{LL}}}{Z_{\mathrm{L}}} \sin(\gamma^{\mathrm{S}})\right) + j e_{\mathrm{S}} \sin^2\left(\frac{\gamma^{\mathrm{S}}}{2}\right) \frac{Z_{\mathrm{sl}}^{\mathrm{SL}}}{Z_{\mathrm{S}}} \sin(\gamma^{\mathrm{L}})\right]}{e_{\mathrm{L}} \times \left(\frac{Z_{\mathrm{sl}}^{\mathrm{L}} Z_{\mathrm{sl}}^{\mathrm{S}}}{Z_{\mathrm{L}} Z_{\mathrm{S}}} \cos(\gamma^{\mathrm{L}}) \cos(\gamma^{\mathrm{S}}) - \sin(\gamma^{\mathrm{L}}) \sin(\gamma^{\mathrm{S}}) + j\left(\frac{Z_{\mathrm{sl}}^{\mathrm{LL}}}{Z_{\mathrm{L}}} \cos(\gamma^{\mathrm{L}}) \sin(\gamma^{\mathrm{S}}) + \frac{Z_{\mathrm{sl}}^{\mathrm{SS}}}{Z_{\mathrm{S}}} \sin(\gamma^{\mathrm{L}}) \cos(\gamma^{\mathrm{S}})\right)\right)} \tag{35g}$$

$$p^{\mathrm{S}} = 1 + \frac{\left[e_{\mathrm{S}} \sin^2\left(\frac{\gamma^{\mathrm{S}}}{2}\right)\left(\frac{Z_{\mathrm{sl}}^{\mathrm{L}} Z_{\mathrm{sl}}^{\mathrm{S}}}{Z_{\mathrm{L}} Z_{\mathrm{S}}} \cos(\gamma^{\mathrm{L}}) + j \frac{Z_{\mathrm{sl}}^{\mathrm{SS}}}{Z_{\mathrm{S}}} \sin(\gamma^{\mathrm{L}})\right) + j e_{\mathrm{L}} \sin^2\left(\frac{\gamma^{\mathrm{L}}}{2}\right) \frac{Z_{\mathrm{sl}}^{\mathrm{SL}}}{Z_{\mathrm{L}}} \sin(\gamma^{\mathrm{S}})\right]}{e_{\mathrm{S}} \times \left(\frac{Z_{\mathrm{sl}}^{\mathrm{L}} Z_{\mathrm{sl}}^{\mathrm{S}}}{Z_{\mathrm{L}} Z_{\mathrm{S}}} \cos(\gamma^{\mathrm{L}}) \cos(\gamma^{\mathrm{S}}) - \sin(\gamma^{\mathrm{L}}) \sin(\gamma^{\mathrm{S}}) + j\left(\frac{Z_{\mathrm{sl}}^{\mathrm{LL}}}{Z_{\mathrm{L}}} \cos(\gamma^{\mathrm{L}}) \sin(\gamma^{\mathrm{S}}) + \frac{Z_{\mathrm{sl}}^{\mathrm{SS}}}{Z_{\mathrm{S}}} \sin(\gamma^{\mathrm{L}}) \cos(\gamma^{\mathrm{S}})\right)\right)} \tag{35h}$$

the resonant frequency (in hertz), Δf is frequency change (in hertz), Δm is the mass change (in grams), A is the piezoelectrically active crystal area (the area between electrodes, in square centimeters), ρ_{q} is the density of quartz ($\rho_{\mathrm{q}} = 2.648$ g/cm³), and μ_{q} is the shear modulus of quartz for AT-cut crystal ($\mu_{\mathrm{q}} = 2.947 \times 10^{11}$ g/cm·s²). The absolute frequency change is proportional to the square of the operating frequency. Because the operational frequency of FBARs can be up to tens of gigahertz, it is believed that sensor sensitivity will be greatly improved. For analyzing sensor performance of the FBARs, the electric impedance expression of an FBAR with a mass loading layer needs to be derived. Acoustic wave resonator sensors usually consist of four layers: one piezoelectric layer, two electrode layers, and a surface loading (mass) layer, as shown in Fig. 8. Usually the electrode layer is quite thin and its acoustic impedance is very small compared with the piezoelectric and mass-loading layers. Thus for simplicity, the effect of electrodes is neglected here. In other words, we only consider the effect of the mass layer on the resonance frequency shift of the dual-mode FBARs. For derivation of the impedance expression, (1)–(28) are adopted here, but the traction forces at the boundary $(x_3' = 0, h)$ change to

$$T_5(0) = T_3(0) = 0 \tag{34a}$$

$$\begin{bmatrix} T_5(h) \\ T_3(h) \end{bmatrix} = \begin{bmatrix} -j\omega Z_{\mathrm{sl}}^{\mathrm{S}} & 0 \\ 0 & -j\omega Z_{\mathrm{sl}}^{\mathrm{L}} \end{bmatrix} \begin{bmatrix} u_1(h) \\ u_3(h) \end{bmatrix}. \tag{34b}$$

$Z_{\mathrm{sl}}^{\mathrm{L}}$ and $Z_{\mathrm{sl}}^{\mathrm{S}}$ are the longitudinal and shear acoustic impedance of the surface mass-loading layer, which can be expressed by

$$Z_{\mathrm{sl}}^{\mathrm{L}} = j\rho_{\mathrm{sl}} v_{\mathrm{sl}}^{\mathrm{L}} \tan\left(\gamma_{\mathrm{sl}}^{\mathrm{L}}\right) \tag{34c}$$

$$Z_{\mathrm{sl}}^{\mathrm{S}} = j\rho_{\mathrm{sl}} v_{\mathrm{sl}}^{\mathrm{S}} \tan\left(\gamma_{\mathrm{sl}}^{\mathrm{S}}\right) \tag{34d}$$

$$v_{\mathrm{sl}}^{\mathrm{L}} = \sqrt{\frac{c_{\mathrm{sl}}^{33}}{\rho_{\mathrm{sl}}}}, \quad v_{\mathrm{sl}}^{\mathrm{S}} = \sqrt{\frac{c_{\mathrm{sl}}^{55}}{\rho_{\mathrm{sl}}}}, \quad \gamma_{\mathrm{sl}}^{\mathrm{L}} = \frac{\omega v_{\mathrm{sl}}^{\mathrm{L}}}{l_{\mathrm{sl}}}, \quad \gamma_{\mathrm{sl}}^{\mathrm{S}} = \frac{\omega v_{\mathrm{sl}}^{\mathrm{S}}}{l_{\mathrm{sl}}}, \tag{34e}$$

where $v_{\mathrm{sl}}^{\mathrm{L}}$ and $v_{\mathrm{sl}}^{\mathrm{S}}$ are longitudinal and shear acoustic velocity of mass-loading layer; $\gamma_{\mathrm{sl}}^{\mathrm{L}}$ and $\gamma_{\mathrm{sl}}^{\mathrm{S}}$ are longitudinal and shear phase delay in the layer; ρ_{sl} and l_{sl} are the density and thickness of the mass layer; c_{sl}^{33} and c_{sl}^{55} are the elastic constants of the mass layer. According to the boundary condition (34) and (1)–(28), the electric impedance of the mass-loaded FBAR can be solved:

$$Z = \frac{1}{j\omega C_0}\left[1 - \left(k^{\mathrm{L}}\right)^2 p^{\mathrm{L}} \frac{\tan(\gamma_{\mathrm{L}}/2)}{\gamma_{\mathrm{L}}/2} - \left(k^{\mathrm{S}}\right)^2 p^{\mathrm{S}} \frac{\tan(\gamma_{\mathrm{S}}/2)}{\gamma_{\mathrm{S}}/2}\right], \tag{35a}$$

where

$$C_0 = \frac{\varepsilon_{33}^{\mathrm{S}\,\prime} A}{h} \tag{35b}$$

$$\left(k^{\mathrm{L}}\right)^2 = \frac{(e_{\mathrm{L}})^2}{\varepsilon_{33}^{\mathrm{S}\,\prime} \rho \left(v^{(\mathrm{L})}\right)^2} \tag{35c}$$

$$\left(k^{\mathrm{S}}\right)^2 = \frac{(e_{\mathrm{S}})^2}{\varepsilon_{33}^{\mathrm{S}\,\prime} \rho (v^{(\mathrm{S})})^2} \tag{35d}$$

$$\gamma_{\mathrm{L}} = \frac{\omega h}{v^{(\mathrm{L})}} \tag{35e}$$

$$\gamma_{\mathrm{S}} = \frac{\omega h}{v^{(\mathrm{S})}}, \tag{35f}$$

with p^{L} and p^{S} as defined in (35g) and (35h), see above, and

$$Z_{\mathrm{sl}}^{\mathrm{LL}} = Z_{\mathrm{sl}}^{\mathrm{L}} \cos^2(\alpha) + Z_{\mathrm{sl}}^{\mathrm{S}} \sin^2(\alpha) \tag{35i}$$

$$Z_{\mathrm{sl}}^{\mathrm{SS}} = Z_{\mathrm{sl}}^{\mathrm{S}} \cos^2(\alpha) + Z_{\mathrm{sl}}^{\mathrm{L}} \sin^2(\alpha) \tag{35j}$$

$$Z_{\mathrm{sl}}^{\mathrm{SL}} = (Z_{\mathrm{sl}}^{\mathrm{S}} - Z_{\mathrm{sl}}^{\mathrm{L}}) \sin(\alpha) \cos(\alpha). \tag{35k}$$

Through analyzing (35), the condition for pure longitudinal mode is $\alpha = 0$, $e_{\mathrm{S}} = 0$, which is equivalent to $c_{35}^{E\,\prime} = 0$, $e_{35}' = 0$; and the condition for pure shear mode is $\alpha = 0$, $e_{\mathrm{L}} = 0$, which is equivalent to $c_{35}^{E\,\prime} = 0$, $e_{33}' = 0$. Hence, from Figs. 2 and 3, we can conclude that the pure longitudinal mode for ZnO and AlN is excited at $\theta = 0°$, and for pure shear mode it is $\theta = 90°$. In addition, α is small because of the small value of $c_{35}^{E\,\prime}$, then longitudinal mode is predominant when $e_{\mathrm{S}} = 0$ and shear mode is predominant when $e_{\mathrm{L}} = 0$; therefore, at $\theta = 65.4°$ for ZnO and $\theta = 67.1°$ for AlN, it can be approximated by pure longitudinal mode; at $\theta = 43°$ for ZnO and $\theta = 46.1°$ for AlN, it can be approximated by pure shear mode.

For a better understanding of the dual-mode FBAR for mass sensors, we gradually increase the mass loading and
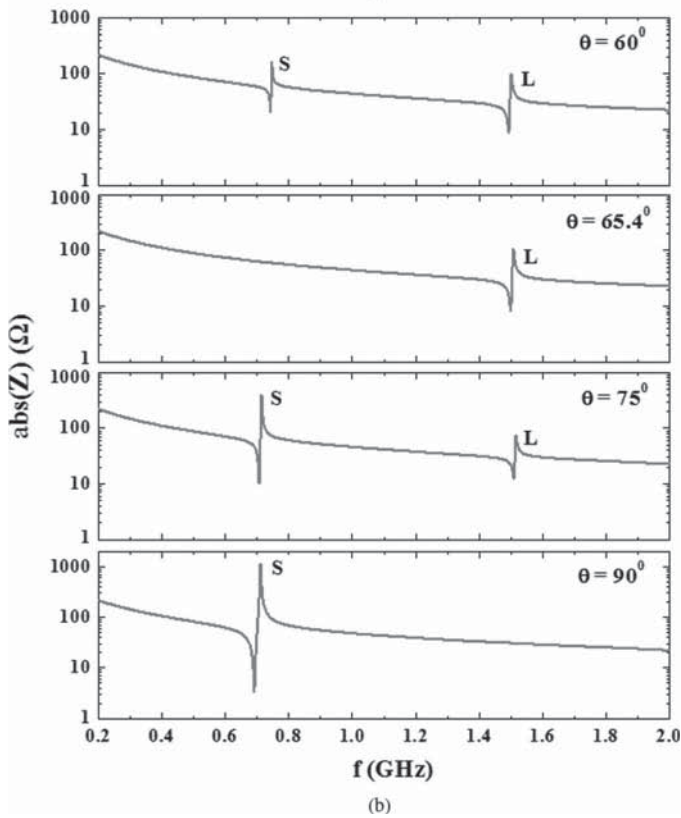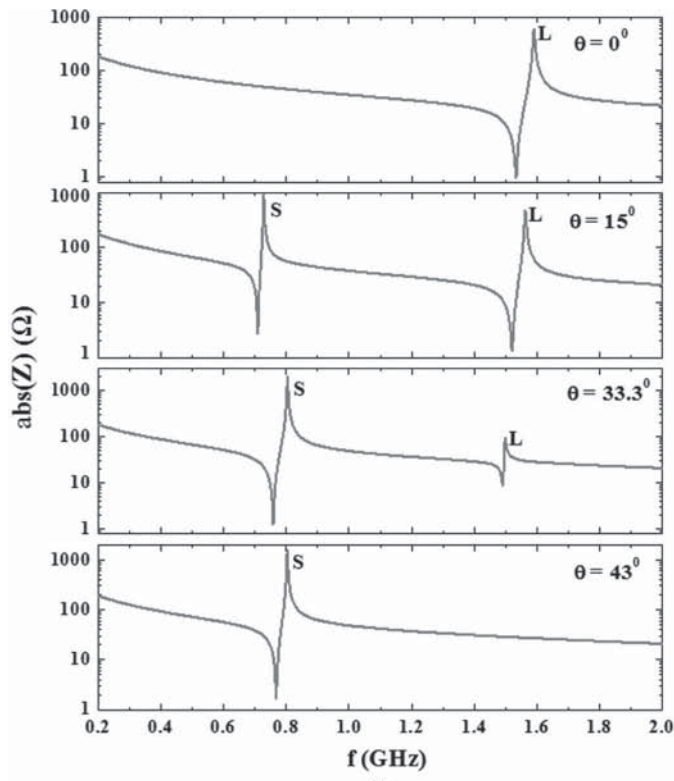
Fig. 6. Impedance spectrum simulation of FBAR based on c-axis tilted ZnO film. (a) $\theta = 0, 15, 33.3$, and 43°; (b) $\theta = 60, 65.4, 75$, and 90°.
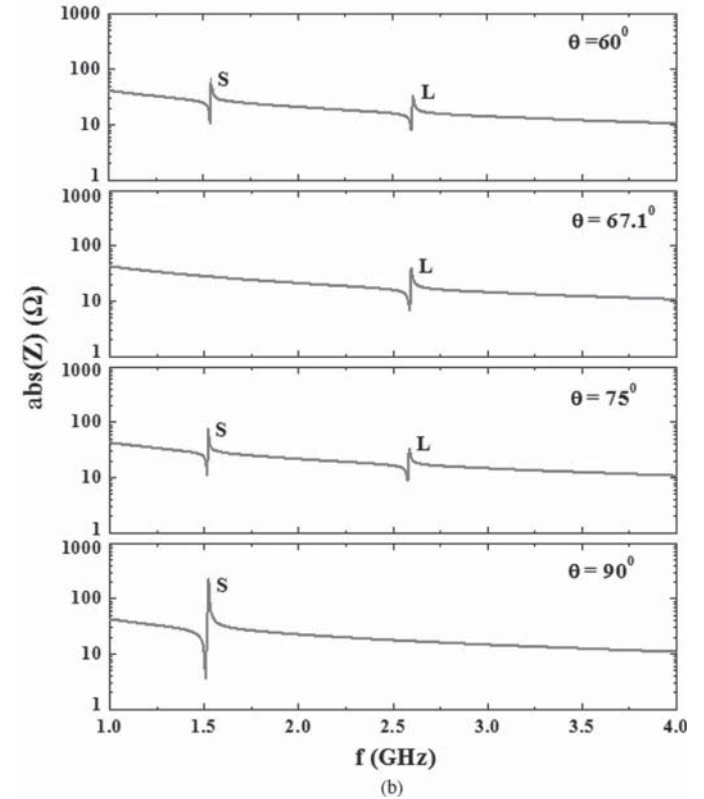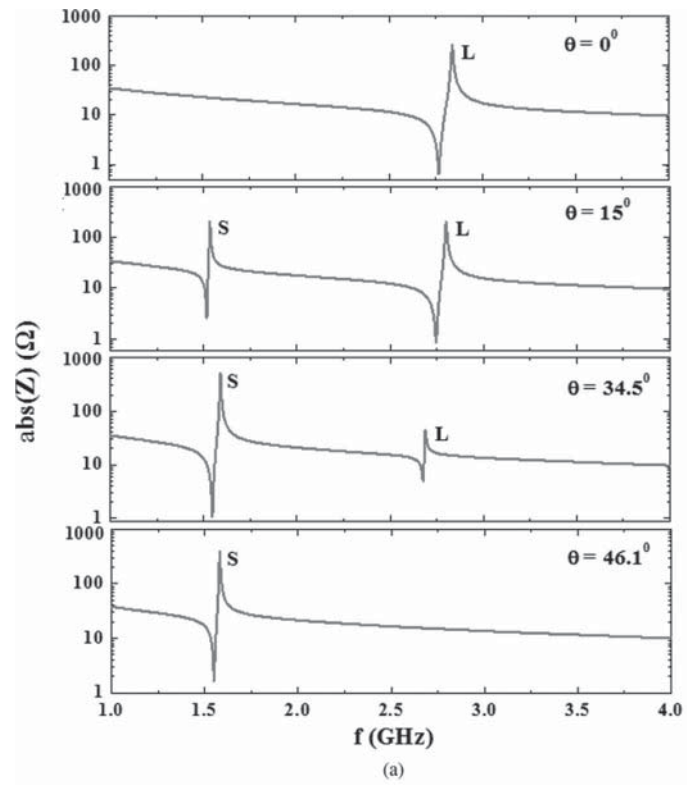

Fig. 7. Impedance spectrum simulation of FBAR based on c-axis tilted AlN film. (a) $\theta = 0, 15, 34.5$, and 46.1°; (b) $\theta = 60, 67.1, 75$, and 90°.

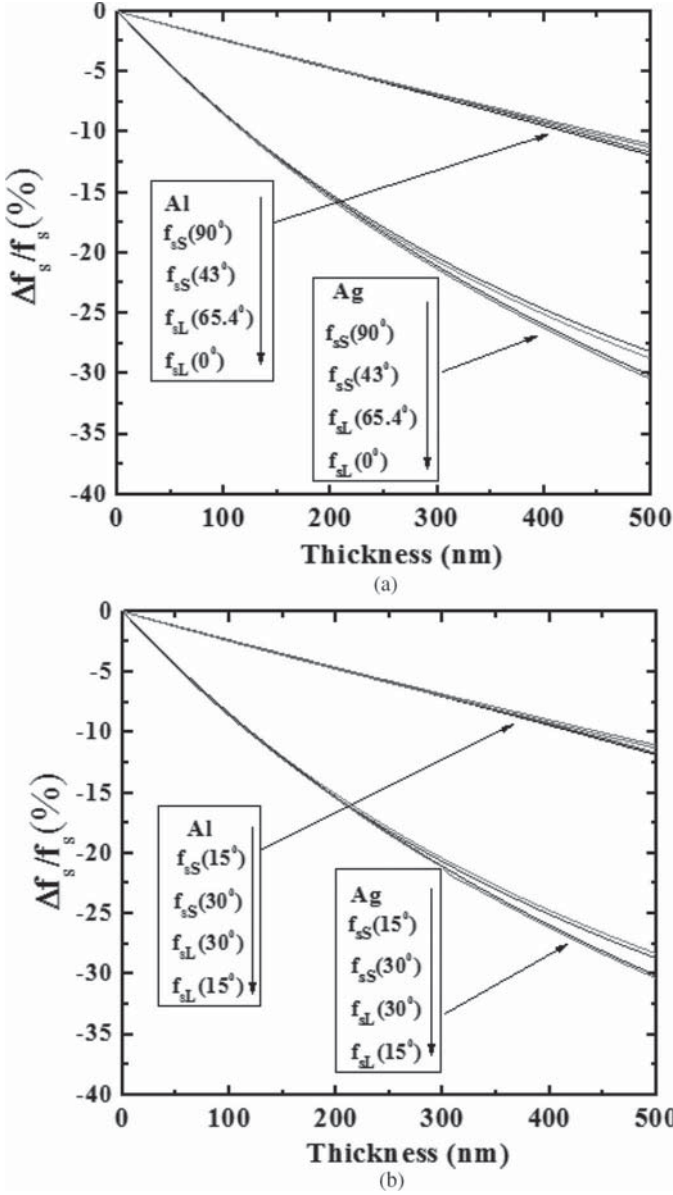Fig. 8. The schematic of FBAR for mass sensor applications.

(a)

(b)

Fig. 9. Resonant frequency shift of FBAR based on c-axis tilted ZnO film vs. thickness of mass loading. (a) θ = 0, 43, 65.4, and 90°; (b) θ = 15 and 30°.

(a)

(b)

Fig. 10. Resonant frequency shift of FBAR based on c-axis tilted AlN film vs. thickness of mass loading. (a) θ = 0, 46.1, 67.1, and 90°; (b) θ = 15 and 30°.

investigate the change of the resonant frequency f_s, which corresponds to maximum conductance and is usually adopted for sensor output. Here, $f_{sL}(\theta)$ and $f_{sS}(\theta)$ are used to express the longitudinal and shear resonant frequency of FBAR based on AlN or ZnO with c-axis tilt angle θ. Figs. 9 and 10 show the change of $f_{sL}(\theta)$ and $f_{sS}(\theta)$ with the thickness of the mass-loading layer for some specific

tilt angles. In the simulation, Al and Ag are the materials for the mass-loading layer, and Table IV lists their parameters for calculation of $f_{sL}(\theta)$ and $f_{sS}(\theta)$ using (35). As shown in Figs. 9 and 10, for mass loading Al and Ag, both $f_{sL}(\theta)$ and $f_{sS}(\theta)$ linearly decrease when the thickness of mass-loading layer is small. For the same thickness of mass loading, the resonant frequency shift for Ag is higher than Al, because Ag has higher density than Al, inducing higher acoustic loading. The mass sensitivity of dual-mode FBARs is defined as

$$S_L(\theta) = \frac{\Delta f_{sL}(\theta)/f_{sL}(\theta)}{\Delta m} \quad (36a)$$

$$S_S(\theta) = \frac{\Delta f_{sS}(\theta)/f_{sS}(\theta)}{\Delta m} \quad (36b)$$

TABLE IV. PARAMETERS FOR CALCULATION OF $F_{sL}(\theta)$ AND $F_{sS}(\theta)$.

Mass-loading layer	Density (kg/m³)	Thickness (nm)	Young's modulus (GPa)	Poisson's ratio	Q_L	Q_S
Al	2700	0–500	70	0.35	1000	1000
Ag	10490	0–500	83	0.37	1000	1000

TABLE V. MASS SENSITIVITY OF FBAR BASED ON c-AXIS TILTED ZnO.

Tilt angle (°)	$f_{sL}(\theta)$ (GHz)	$f_{sS}(\theta)$ (GHz)	$S_L(\theta)$ (cm²/g)		$S_S(\theta)$ (cm²/g)	
			Al	Ag	Al	Ag
0	1.533439408	—	−904	−904	—	—
15	1.520757366	0.709173538	−896	−894	−896	−896
30	1.496097496	0.751143640	−882	−879	−926	−919
43	—	0.767714844	—	—	−911	−909
65.4	1.499892844	—	−881	−877	—	—
90	—	0.690955092	—	—	−896	−896

TABLE VI. MASS SENSITIVITY OF FBAR BASED ON c-AXIS TILTED AlN.

Tilt angle (°)	$f_{sL}(\theta)$ (GHz)	$f_{sS}(\theta)$ (GHz)	$S_L(\theta)$ (cm²/g)		$S_S(\theta)$ (cm²/g)	
			Al	Ag	Al	Ag
0	2.767650148	—	−1570	−1558	—	—
15	2.746620142	1.517122380	−1556	−1548	−1548	−1539
30	2.695601826	1.541801144	−1541	−1531	−1570	−1560
46.1	—	1.550894306	—	—	−1563	−1548
67.1	2.588555566	—	−1548	−1525	—	—
90	—	1.507487836	—	—	−1548	−1535

$$\Delta m = \rho_m t_m, \qquad (36c)$$

where $S_L(\theta)$ is the mass sensitivity of longitudinal mode for FBAR based on AlN or ZnO with c-axis tilt angle θ and $S_S(\theta)$ is the mass sensitivity of shear mode; $\Delta f_{sL}(\theta)$ and $\Delta f_{sS}(\theta)$ are the resonant frequency shifts caused by mass loading Δm; ρ_m, and t_m are the density and thickness of mass-loading layer. The mass sensitivity of FBARs in a linear range $(\Delta f_s(\theta)/f_s(\theta) \leq 5\%)$ is evaluated through examining resonant frequency shift for 5 nm Al or Ag mass loading, and the calculated mass sensitivity for some special angles according to (36) is listed in Tables V and VI. It can be seen from Tables V and VI that $S_L(\theta)$ and $S_S(\theta)$ of ZnO are around −900 cm²/g, and $S_L(\theta)$ and $S_S(\theta)$ of AlN are around −1550 cm²/g, which is much higher than −14 cm²/g, the mass sensitivity of a 6-MHz QCM [36]. Because of the small value of α or $c_{35}^{E}{}'$ for all θ, the coupling between longitudinal and shear mode is weak, so the resonator can be approximated by a simple combination of two single modes. On the other hand, it is known that the mass sensitivity (S_m) of single mode resonator is dependent on the density (ρ_p) and thickness (d_p) of the piezo layer [36].

$$S_m = \frac{-1}{\rho_p d_p} \qquad (37)$$

Hence, for ZnO or AlN FBAR, $S_L(\theta)$ and $S_S(\theta)$ have similar values, and do not change much with tilt angle, which also can be seen in Table V and VI.

It should be pointed out that in (35) the mass loading layer is assumed to be isotropic. When this layer is the material used for electrodes, (35) can be used to analyze the effect of electrode thickness, which actually has been shown in mass sensitivity calculations. Moreover, through replacing the acoustic impedance of the single mass-loading layer with the acoustic impedance of a multilayer loading, (35) can be used for analysis of multilayer loading on the frequency change of the resonator, as long as the multilayer is isotropic and non-piezoelectrically active.

IV. CONCLUSION

FBARs based on ZnO and AlN films with tilted c-axis orientation have been theoretically studied. Because of the crystalline orientation dependence of the material properties, including elastic stiffness, piezoelectric coefficients, and dielectric constants, the acoustic velocity, electro-mechanical coefficient, and electric impedance of FBARs all depend on the crystalline orientation. The equation for predicting the electric impedance of FBARs has been derived through the basic piezoelectric equations, which shows the coexistence of longitudinal and shear modes when the c-axis tilt angle changes. The simulation results show that a pure longitudinal mode occurs at 0° and 65.4°, and a pure shear mode occurs at 43° and 90° for ZnO; a pure longitudinal mode occurs at 0° and 67.1°, and a pure shear mode occurs at 46.1° and 90° for AlN. Two peaks

of shear electromechanical coefficient are found at $\theta = 33.3°, 90°$ for ZnO and $\theta = 34.5°, 90°$ for AlN. ZnO and AlN films with a tilt angle around these two peaks are good options for FBAR applications in liquid, considering their strong shear resonance and high electromechanical coefficients. The mass sensitivity of FBAR-based ZnO and AlN are much higher than that of QCMs, which shows good promise for use as mass sensors.

REFERENCES

[1] K. M. Lakin, G. R. Kline, R. S. Ketcham, and S. G. Burns, "Thin film resonator based low insertion loss filters," in *IEEE Ultrasonics Symp.*, 1986, pp. 371–376.

[2] K. M. Lakin, "Thin film resonators and filters," in *IEEE Ultrasonics Symp.*, 1999, vol. 2, pp. 895–906.

[3] R. Weigel, D. P. Morgan, J. M. Owens, A. Ballato, K. M. Lakin, K.-y. Hashimoto, and C. C. W. Ruppel, "Microwave acoustic materials, devices, and applications," *IEEE Trans. Microw. Theory Tech.*, vol. 50, pp. 738–749, Mar. 2002.

[4] M. Ylilammi, J. Ella, M. Partanen, and J. Kaitila, "Thin film bulk acoustic wave filter," *IEEE Trans. Ultrason. Ferroelectr. Freq. Control*, vol. 49, pp. 535–539, Apr. 2002.

[5] H. P. Löbl, M. Klee, R. Milsom, R. Dekker, C. Metzmacher, W. Brand, and P. Lok, "Materials for bulk acoustic wave (BAW) resonators and filters," *J. Eur. Ceram. Soc.*, vol. 21, no. 15, pp. 2633–2640, 2001.

[6] T. Nishihara, T. Yokoyama, T. Miyashita, and Y. Satoh, "High performance and miniature thin film bulk acoustic wave filters for 5 GHz," in *Proc. IEEE Ultrasonics Symp.*, 2002, vol. 1, pp. 969–972.

[7] R. Lanz and P. Muralt, "Solidly mounted BAW filters for 8 GHz based on AlN thin films," in *Proc. IEEE Ultrasonics Symp.*, 2003, pp. 178–181.

[8] D. Feld, K. Wang, P. Bradley, A. Barfknecht, B. Ly, and R. Ruby, "A high performance 3.0 mm × 3.0 mm × 1.1 mm FBAR full band filter for U.S. PCS handsets," in *IEEE Ultrasonics Symp.*, 2002, pp. 913–918.

[9] R. Gabl, H.-D. Feucht, H. Zeininger, G. Eckstein, M. Schreiter, R. Primig, D. Pitzer, and W. Wersing, "First results on label-free detection of DNA and protein molecules using a novel integrated sensor technology based on gravimetric detection principles," *Biosens. Bioelectron.*, vol. 19, no. 6, pp. 615–620, Jan. 2004.

[10] H. Zhang, M. S. Marma, E. S. Kim, C. E. McKenna, and M. E. Thompson, "A film bulk acoustic resonator in liquid environments," *J. Micromech. Microeng.*, vol. 15, no. 10, pp. 1911–1916, 2005.

[11] M. Benetti, D. Cannatà, and F. Di Pietrantonio, "Microbalance chemical sensor based on thin-film bulk acoustic wave resonators," *Appl. Phys. Lett.*, vol. 87, art. no. 173504, 2005.

[12] H. Zhang and E. S. Kim, "Micromachined acoustic resonant mass sensor," *J. Microelectromech. Syst.*, vol. 14, no. 4, pp. 699–706, Aug. 2005.

[13] D. S. Ballantine, R. M. White, S. J. Martin, A. J. Ricco, G. C. Frye, E. T. Zellers, and H. Wohltjen, *Acoustic Wave Sensors: Theory, Design, and Physico-Chemical Applications*. New York, NY: Academic Press, 1997.

[14] N. F. Foster, G. A. Coquin, G. A. Rozgonyi, and F. A. Vannatta, "Cadmium sulphide and zinc oxide thin-film transducers," *IEEE Trans. Sonics Ultrason.*, vol. 15, pp. 28–40, Jan. 1968.

[15] R. H. Wittstruck, X. Tong, N. W. Emanetoglu, P. Wu, Y. Chen, J. Zhu, S. Muthukumar, Y. Lu, and A. Ballato, "Characteristics of Mg$_x$Zn$_{1-x}$O thin film bulk acoustic wave devices," *IEEE Trans. Ultrason. Ferroelectr. Freq. Control*, vol. 50, pp. 1272–1278, Oct. 2003.

[16] T. Yanagitani, T. Nohara, M. Matsukawa, Y. Watanabe, and T. Otani, "Characteristics of (1010) and (110) textured ZnO piezofilms for a shear mode resonator in the VHF-UHF frequency ranges," *IEEE Trans. Ultrason. Ferroelectr. Freq. Control*, vol. 52, pp. 2140–2145, Nov. 2005.

[17] T. Yanagitani, N. Mishima, M. Matsukawa, and Y. Watanabe, "Electromechanical coupling coefficient k_{15} of polycrystalline ZnO films with the c-axes lie in the substrate plane," *IEEE Trans. Ultrason. Ferroelectr. Freq. Control*, vol. 54, pp. 701–704, Apr. 2007.

[18] M. Link, M. Schreiter, J. Weber, R. Primig, D. Pitzer, and R. Gabl, "Solidly mounted ZnO shear mode film bulk acoustic resonators for sensing applications in liquids," *IEEE Trans. Ultrason. Ferroelectr. Freq. Control*, vol. 53, pp. 492–496, Feb. 2006.

[19] S. Wu, Z. Lin, M. Lee, and R. Ro, "Bulk acoustic wave analysis of crystalline plane oriented ZnO films," *J. Appl. Phys.*, vol. 102, no. 8, art. no. 084908, 2007.

[20] J. Bjurström, D. Rosén, I. Katardjiev, V. M. Yanchev, and I. Petrov, "Dependence of the electromechanical coupling on the degree of orientation of c-textured thin AlN films," *IEEE Trans. Ultrason. Ferroelectr. Freq. Control*, vol. 51, pp. 1347–1353, Oct. 2004.

[21] G. Wingqvist, J. Bjurström, L. Liljeholm, I. Katardjiev, and A. L. Spetz, "Shear mode AlN thin film electroacoustic resonator for biosensor applications," in *IEEE Sensor Proc.*, 2005, pp. 492–495.

[22] J. Bjurström, G. Wingqvist, and I. Katardjiev, "Synthesis of textured thin piezoelectric AlN films with a nonzero c-axis mean tilt for the fabrication of shear mode resonators," *IEEE Trans. Ultrason. Ferroelectr. Freq. Control*, vol. 53, pp. 2095–2100, Nov. 2006.

[23] G. Wingqvist, J. Bjurström, L. Liljeholm, V. Yantchev, and I. Katardjiev, "Shear mode AlN thin film electro-acoustic resonant sensor operation in viscous media," *Sens. Actuators B*, vol. 123, pp. 466–473, Apr. 2007.

[24] F. Martin, M.-E. Jan, S. Rey-Mermet, B. Belgacem, D. Su, M. Cantoni, and P. Muralt, "Shear mode coupling and tilted grain growth of AlN thin films in BAW resonators," *IEEE Trans. Ultrason. Ferroelectr. Freq. Control*, vol. 53, pp. 1339–1343, Jul. 2006.

[25] F. Martin, M.-E. Jan, B. Belgacem, M.-A. Dubois, and P. Muralt, "Shear mode coupling and properties dispersion in 8 GHz range AlN thin film bulk acoustic wave (BAW) resonator," *Thin Solid Films*, vol. 514, no. 1-2, pp. 341–343, 2006.

[26] C. Chung, Y. Chen, C. Cheng, and K. Kao, "Synthesis and bulk acoustic wave properties on the dual mode frequency shift of solidly mounted resonators," *IEEE Trans. Ultrason. Ferroelectr. Freq. Control*, vol. 55, pp. 857–864, Apr. 2008.

[27] Q. Chen, F. Li, H. Cheng, and Q. Wang, "Characteristics of dual mode AlN thin film bulk acoustic wave resonators," in *IEEE Int. Frequency Control Symp.*, 2008, pp. 609–614.

[28] H. F. Tiersten, *Linear Piezoelectric Plates Vibrations*. New York, NY: Plenum Press, 1969.

[29] B. A. Auld, *Acoustic Fields and Waves in Solids*, vol. 1, New York, NY: Wiley, 1973.

[30] G. Carlotti, G. Socino, A. Petri, and E. Verona, "Elastic constants of sputtered ZnO films," in *IEEE Ultrasonics Symp.*, pp. 295–300, 1987.

[31] J. F. Rosenbaum, *Bulk Acoustic Waves Theory and Devices*. Norwood, MA: Artech House, 1988.

[32] K. Tsubouchi, K. Sugai, and N. Mikoshiba, "AlN material constants evaluation and SAW properties on AlN/Al$_2$O$_3$ and AlN/Si," in *IEEE Ultrasonics Symp.*, 1981, pp. 375–380.

[33] Q. Chen and Q.-M. Wang, "The effective electromechanical coupling coefficient of piezoelectric thin-film resonators," *Appl. Phys. Lett.*, vol. 86, art. no. 022904, 2005.

[34] G. Sauerbrey, "Use of quartz vibrator for weighing thin films on a microbalance," *Z. Phys.*, vol. 155, pp. 206–222, Feb. 1959.

[35] *QCM100 Quartz Crystal Microbalance Analog Controller/QCM25 Crystal Oscillator*, rev 1.1, Stanford Research Systems, Sunnyvale, CA, 2002.

[36] R. P. O'Toole, S. G. Burns, G. J. Bastiaans, and M. D. Porter, "Thin aluminum nitride film resonators: Miniaturized high sensitivity mass sensors," *Anal. Chem.*, vol. 64, no. 11, pp. 1289–1294, 1992.
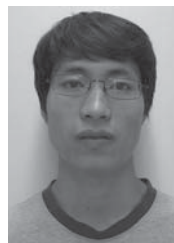
Lifeng Qin was born in Dongyang, Zhejiang, China, in 1979. He received B.S. and M.S. degrees in the Department of Biomedical Engineering from Zhejiang University, Hangzhou, Zhejiang, China, in 2002 and 2005, respectively. He is currently a Ph.D. degree candidate in the Department of Mechanical Engineering and Materials Science, University of Pittsburgh, Pittsburgh, PA.

He has been working as a research assistant in University of Pittsburgh since 2005. His primary research interests include biosensors, piezoelectric devices for characterizing mechanical properties of thin films, and SAW and BAW sensor applications. He is a member of IEEE.
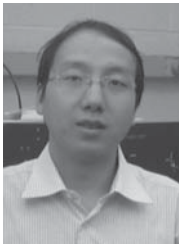
Qingming Chen received the B.S. and M.S. degrees in materials science and engineering from Tsinghua University in 1999 and 2001, respectively, and the Ph.D. degree in mechanical engineering from the University of Pittsburgh, Pittsburgh, PA, in 2006. From 2006 to 2007, he was a post-doc research associate at the University working on thin film bulk acoustic wave resonators and piezoelectric MEMS. He is a professor at the Kunming University of Science and Technology since 2007. His primary research interests include functional materials and devices, microelectromechanical systems (MEMS) and microfabrication, acoustic devices including SAW and BAW resonators for RF resonator and filter applications. He is a member of the American Society of Mechanical Engineers (ASME).

Hongbin Cheng received his B.S. and M.S. degrees from Tsinghua University, Beijing, China, in 1995 and 1998, respectively; and his Ph.D. degree from the University of Pittsburgh in 2009. He is currently a faculty member in Central South University of China. His primary research interests include piezoelectric devices for sensor and actuator applications, nanomaterials, and micro- and nanofabrication.

Qing-Ming Wang (M'00) is an associate professor in the Department of Mechanical Engineering and Materials Science, the University of Pittsburgh, PA. He received the B.S. and M.S. degrees in materials science and engineering from Tsinghua University, Beijing, China, in 1987 and 1989, respectively, and the Ph.D. degree in materials from the Pennsylvania State University in 1998.

Prior to joining the University of Pittsburgh, Dr. Wang was an R&D engineer and materials scientist for Lexmark International, Inc., Lexington, KY, where he worked on piezoelectric and electrostatic microactuators for inkjet printhead development. From 1990 to 1992, he worked as a development engineer for a technology company in Beijing, where he participated in the research and development of electronic materials and piezoelectric devices. From 1992 to 1994, he was a research assistant in the New Mexico Institute of Mining and Technology, working on nickel-zinc ferrite and ferrite/polymer composites for EMI filter application. From 1994 to 1998, he was a graduate assistant in the Materials Research Laboratory of the Pennsylvania State University working toward his Ph.D. degree in the areas of piezoelectric ceramic actuators for low-frequency active noise cancellation and vibration damping, and thin film materials for microactuator and microsensor applications.

Dr. Wang's primary research interests are in microelectromechanical systems (MEMS) and microfabrication; thin film bulk acoustic wave resonators (FBAR) and acoustic wave sensors; functional nanomaterials and devices; and piezoelectric and electrostrictive thin films and composites for transducer, actuator, and sensor applications. He is a member of IEEE, IEEE-UFFC, the Materials Research Society (MRS), ASME, and the American Ceramic Society.

Acoustic Wave Flow Sensor Using Quartz Thickness Shear Mode Resonator

Lifeng Qin, Zijing Zeng, Hongbin Cheng, and Qing-Ming Wang, *Member, IEEE*

Abstract—A quartz thickness shear mode (TSM) bulk acoustic wave resonator was used for *in situ* and real-time detection of liquid flow rate in this study. A special flow chamber made of 2 parallel acrylic plates was designed for flow measurement. The flow chamber has a rectangular flow channel, 2 flow reservoirs for stabilizing the fluid flow, a sensor mounting port for resonator holding, one inlet port, and one outlet port for pipe connection. A 5-MHz TSM quartz resonator was edge-bonded to the sensor mounting port with one side exposed to the flowing liquid and other side exposed to air. The electrical impedance spectra of the quartz resonator at different volumetric flow rate conditions were measured by an impedance analyzer for the extraction of the resonant frequency through a data-fitting method. The fundamental, 3rd, 5th, 7th, and 9th resonant frequency shifts were found to be around 920, 3572, 5947, 8228, and 10 300 Hz for flow rate variation from 0 to 3000 mL/min, which had a corresponding Reynolds number change from 0 to 822. The resonant frequency shifts of different modes are found to be quadratic with flow rate, which is attributed to the nonlinear effect of quartz resonator due to the effective normal pressure imposing on the resonator sensor by the flowing fluid. The results indicate that quartz TSM resonators can be used for flow sensors with characteristics of simplicity, fast response, and good repeatability.

I. Introduction

A flow sensor is a device for sensing the rate of fluid flow. It is a critical component for system operation monitoring and control in many industrial and laboratory applications. Typically, a flow sensor is the sensing element used in a flow meter or flow logger to record the flow of fluids. There are various types of flow sensors and flow meters in practical applications. Traditional mechanical devices, such as variable area flow meters, pitot tubes, and turbine meters, are simple and do not require power supply [1]; however, they are limited by their physical size and mechanical characteristics, especially for applications that require integration of electronic control. Some invasive methods such as ultrasonic flow meters [2] and laser doppler anemometers [3] are nonintrusive and highly sensitive to flow rate, however, they are expensive and require complex auxiliary electronic parts. Additionally, the widely used thermal anemometers such as hot-wire anemometer, can measure the flow in a precise location

and has extremely high frequency response. However, it also has many problems in device design and applications, including breakage of filament stability, calibration, and auxiliary electronics [4].

Acoustic wave resonators including BAW and SAW devices have been regarded as the most sensitive sensor platforms that take the advantage of precise frequency counting in electronic measurement, and they have been extensively studied for many physical- and chemical-sensing applications [5]. Acoustic wave resonators have been investigated for flow rate measurement, and flow sensors based on SAW resonators have been demonstrated with attractive features of high sensitivity, wide dynamic range, and direct digital output [6], [7]. This kind of SAW flow sensor is based on thermal convection: a SAW device with a heater is placed in the flow path. When the fluid flow passes over the sensor surface, it carries heat and changes the temperature of the sensor substrate. Thus, the frequency of the SAW device changes due to its frequency-temperature dependence. Although the theoretical aspect of this kind of sensor is simple and well established, the necessity of a heater for sensor operation may impose practical difficulties in which large power consumption is usually not desirable for compact sensor operation. In addition, the variation of ambient temperature and heater power supply may cause instability of frequency output; to minimize these effects, an additional SAW device that is not exposed to the fluid flow is needed as a reference, which increases system complexity.

On the other hand, to the best of our knowledge, BAW resonators have not been investigated for flow sensors. Among all the acoustic wave sensor configurations, BAW resonators, particularly quartz thickness shear mode (TSM) resonators, are often preferable in many sensor applications due to its high sensitivity, simple structure, and easy interconnection with electronic measurement systems [8]–[12]. Commonly, a resonator consists of one thin layer of piezoelectric material with 2 electrodes on both sides. For sensor applications, an external chemical or physical sensitive thin film is usually coated on the top of the resonator. When an ac electric field is applied across the resonator electrodes, acoustic waves are generated and propagate in the device due to the piezoelectric property of quartz crystal. Variations in coating thin-film parameters, including the thickness, density, and complex shear modulus and interfacial interactions, affect the amplitude and phase of the acoustic wave propagation in the device, which changes the electrical properties of the resonator. Therefore, the measured quantity can be precisely ex-

tracted by the resonance characteristics and the electrical spectrum of the resonator.

The electrical properties of the resonator, such as resonant frequency shift and mechanical damping, depend not only on the mechanical properties of the coating layer and the surface interactions, but also on mechanical or electrical loading conditions because the material properties of quartz resonators are subjected to changes under electrical or mechanical fields. For example, it is found that the resonant frequency of quartz resonators will shift due to nonlinear elastic responses when it is subjected to bias fields [13]–[19]. Among these studies, Ballato *et al.* revealed that the resonant frequency shift of a single-rotated Y-cut quartz resonator due to the applied force on the rim is dependent on the force magnitude, crystal cut angle, azimuth angle, and the vibration mode [13]. The force-frequency effect of double-rotated quartz resonators was also investigated [14]. Ratajski introduced the force-frequency coefficient K_f for quantifying the force-frequency effect, and an empirical chart based on the normalized experimental results was derived, which can be used to determine the force-frequency behavior of any crystal cut in the singly rotated Y-cut group [15]. Lee *et al.* derived 2-D governing equations for theoretical analysis of force-frequency effect; and the formula for predicting the resonant frequency shift was developed and compared with experimental results [16], [17]. Numerical methods including finite element method (FEM) were also used to investigate the force-frequency effect of quartz resonators [18], [19]. When the acoustic wave resonators are used for frequency control and signal processing applications, it is often desirable to minimize force-frequency effect. On the other hand, through the force-frequency effect, quartz acoustic wave resonators have also found applications as force sensors, pressure sensors, or accelerometers [20]–[22]. Therefore, it is possible to apply the resonator for flow measurement if the mechanical load due to the flow can significantly change the frequency response of acoustic wave resonators due to linear or nonlinear response of the device by choosing an appropriate flow path and mechanical boundary conditions.

In this paper, a quartz acoustic wave resonator is studied as flow sensor for *in situ* and real-time detection of fluid (water) flow rate at room temperature. Considering the structural simplicity and high mechanical quality factor, a quartz TSM resonator is particularly chosen as the sensing element. For flow rate measurement, the quartz resonator is edge-bonded at the sensor mounting port in a specially designed flow chamber. First, the relationship of the resonant frequency shift to the flow rate is theoretically discussed based on the nonlinear response of the resonator. The resonant frequency shifts of fundamental thickness shear mode and overtones are then monitored as the sensor responses to different flow rates. The sensitivity and repeatability of the acoustic wave flow sensor are experimentally studied. Finally a brief discussion is given on the flow sensor optimization and potential applications.
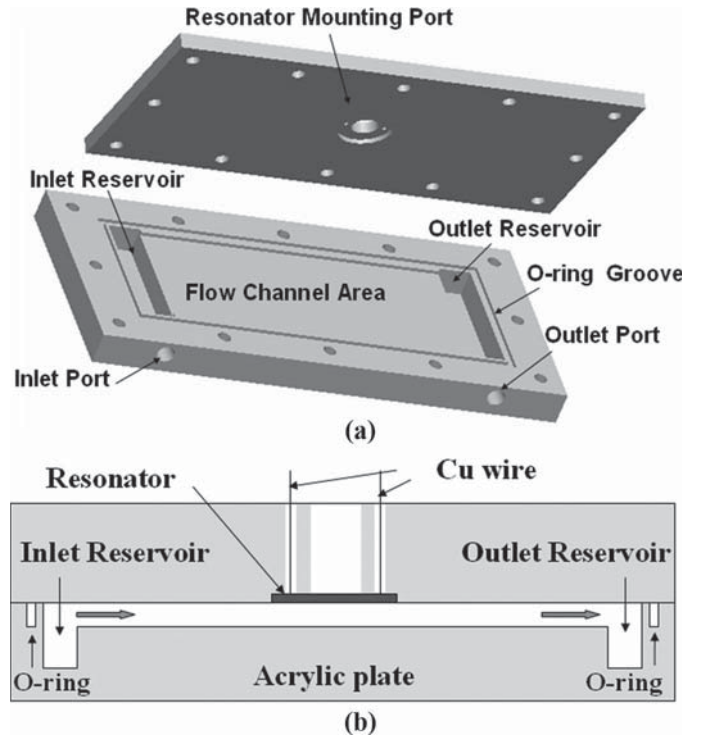
Fig. 1. Schematic of flow chamber: (a) top and bottom plate and (b) cross-sectional view.

II. MATERIAL AND METHODS

A. Quartz TSM Resonator and Flow Chamber

A 5-MHz quartz At-cut TSM resonator (Stanford Research Systems, Inc., Sunnyvale, CA) with 25.4-mm diameter was used in this study as a flow sensor. A flow chamber was designed according to the method proposed by Chuang *et al.* [23]. Fig. 1 shows the schematic of the chamber, which is composed of 2 parallel acrylic plates, in which a rectangular flow channel, inlet and outlet reservoir, 1 sensor mounting port, and 1 inlet port and outlet port are formed. These 2 plates were held together through bolts and an O-ring between them to prevent the liquid leakage. The top plate was machined to form a sensor mounting port, and the quartz resonator was edge-bonded at the port using epoxy of Eccobond 45 Clear (Ellsworth Adhesives, Germantown, WI) such that one surface of the resonator is exposed to the flowing liquid and the other surface is exposed to the air. Two fine Cu wires were bonded to the resonator electrodes through silver paste, which provides electrical connection for resonator impedance measurement. The rectangular flow channel, inlet reservoir, outlet reservoir, inlet port, and outlet port were formed in the bottom of the plate. During flow measurement, fluid entered the inlet reservoir through the inlet port, passed through the rectangular flow channel, flowed into the outlet reservoir, and exited through the outlet port. Plastic pipes were connected to inlet and outlet ports for flow delivery. The dimension of the flow channel is 165.10 mm × 69.85 mm × 0.51 mm
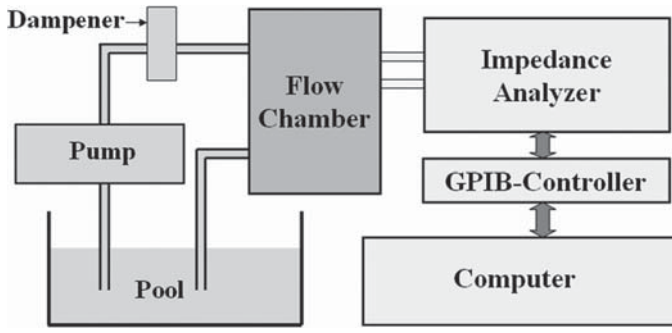
Fig. 2. The experiment setup for flow rate measurement.

$(L \times w \times h)$, and the dimension for these 2 reservoirs is 19.05 mm $\times$ 76.0 mm $\times$ 15.24 mm.

B. Experiment Setup and Procedure

Fig. 2 shows the measurement setup, which is made of a water pool, Manostat Preston pump (Thermo Scientific, Barrington, IL), pulse dampener (Cole-Parmer Instrument Company, Vernon Hills, IL), flow chamber, Agilent 4294A precision impedance analyzer (Agilent Technologies, Palo Alto, CA), Hi-Speed GPIB Controller (National Instruments, Austin, TX), and computer. The pool was used to store the fluid: deionized (DI) water, which was driven by the pump. The water level in the pool is a little higher than the flow chamber, which produces around 30 cm of water pressure on the resonator. The pulse dampener was adopted to smooth the flow considering the unstable flow due to the pulse pump. The resonator admittance impedance spectra near the resonant frequencies were recorded by the impedance analyzer. By data fitting the admittance impedance spectra, the resonant frequencies were precisely extracted; 1st (fundamental), 3rd, 5th, 7th, and 9th series resonant frequencies as the sensor response were monitored and recorded during flow measurement. Water flow rates up to 3000 mL/min were used in this study, all of which are limited to laminar flow; corresponding Reynolds numbers were 0 to 822.

C. Method of Flow Measurement

Fig. 3 shows the schematic cross sections of the flow channel, and the Cartesian coordinate system (x, y, z) for fluid flow discussion. The top and bottom plate is at $y = h/2$ and $y = -h/2$. The lateral walls are at $z = \pm w/2$. In the rectangular flow channel, the relation of pressure p and volumetric flow rate Q is given by [23], [24]:

$$Q = \frac{h^3 w}{12\mu}\left(-\frac{dp}{dx}\right)\left[1 - \frac{192h}{\pi^5 w}\sum_{n=1,3,5...}^{\infty}\frac{1}{n^5}\tanh\left(\frac{n\pi w}{2h}\right)\right], \quad (1)$$

where μ, L, w, and h are the viscosity of fluid, the length, width, and height of the flow channel. Shear stress τ at the wall ($y = \pm h/2$) is given by [23]:
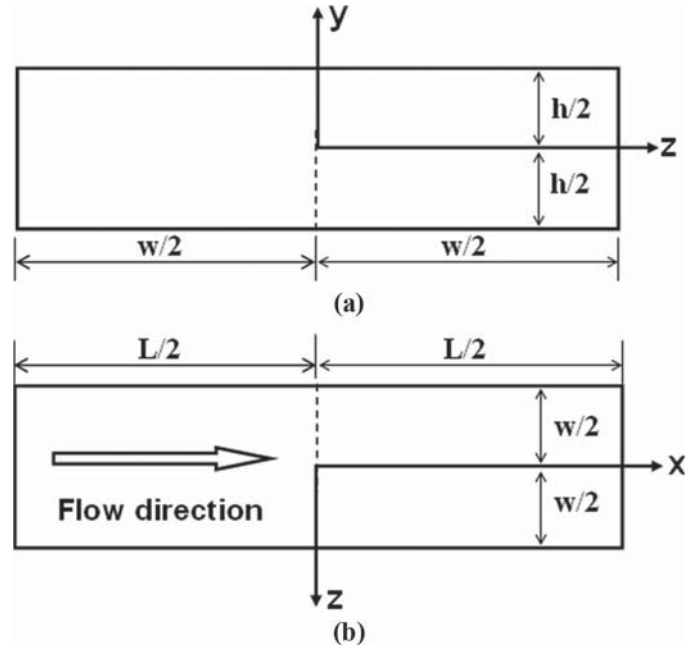
Fig. 3. Schematic cross-sections of the flow channel: (a) yz plane and (b) xz plane.

$$\tau = \frac{h}{2}\left(-\frac{dp}{dx}\right)\left[1 - \frac{8}{\pi^2}\sum_{n=1,3,5...}^{\infty}\frac{1}{n^2}\frac{\cosh\left(\frac{n\pi z}{h}\right)}{\cosh\left(\frac{n\pi w}{2h}\right)}\right]. \quad (2)$$

From (1), one can get:

$$\frac{dp}{dx} = -\frac{12Q\mu}{h^3 w\left(1 - \frac{192h}{\pi^5 w}\sum_{n=1,3,5...}^{\infty}\frac{1}{n^5}\tanh\left(\frac{n\pi w}{2h}\right)\right)}. \quad (3)$$

The resonator is located at $(0, h/2, 0)$. Thus, when Q is constant, the normal pressure difference ΔP on the 2 sides of the resonator can be obtained as:

$$\Delta P = \int_{L/2}^{0}\frac{dp}{dx}dx + \frac{8\mu L_p}{\pi R_p^4}Q$$

$$= \frac{6Q\mu L}{h^3 w\left(1 - \frac{192h}{\pi^5 w}\sum_{n=1,3,5...}^{\infty}\frac{1}{n^5}\tanh\left(\frac{n\pi w}{2h}\right)\right)} + \frac{8\mu L_p}{\pi R_p^4}Q, \quad (4)$$

where L_p and R_p are the length and radius of the pipe connected to the outlet port. The first term in (4) represents the pressure drop from the resonator position to the outlet port in the flow channel, and the second term is the pipe pressure drop from the outlet port to the water pool. Also, The shear stress τ_r on the resonator surface can be obtained by substituting the resonator position into (2):
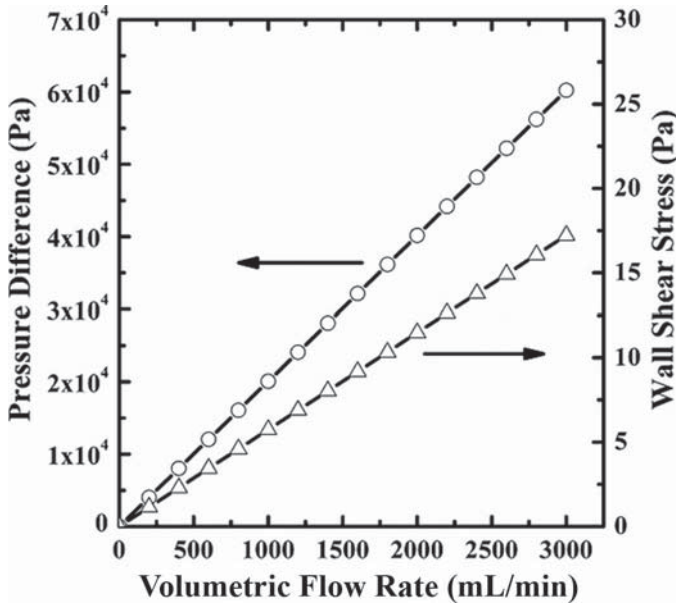
Fig. 4. The normal pressure difference and wall shear stress versus volumetric flow rate.

$$\tau_r = \frac{h}{2}\left(-\frac{dp}{dx}\right)\left[1 - \frac{8}{\pi^2}\sum_{n=1,3,5...}^{\infty}\frac{1}{n^2}\frac{\cosh\left(\frac{n\pi z}{h}\right)}{\cosh\left(\frac{n\pi w}{2h}\right)}\right]_{z=0}$$

$$= \frac{6\mu Q}{h^2 w}\frac{\left[1 - \frac{8}{\pi^2}\sum_{n=1,3,5...}^{\infty}\frac{1}{n^2\cosh\left(\frac{n\pi w}{2h}\right)}\right]}{\left[1 - \frac{192h}{\pi^5 w}\sum_{n=1,3,5...}^{\infty}\frac{1}{n^5}\tanh\left(\frac{n\pi w}{2h}\right)\right]}. \quad (5)$$

Eqs. (4) and (5) indicate that both ΔP and τ_r are proportional to the flow rate. Fig. 4 plots the calculation results of ΔP and τ_r verse flow rate.

When the device is subjected to fluid flow, the resonator will be deformed due to ΔP and τ_r. In Fig. 5(a) the dotted line indicates the middle plane, which has a flexure deflection w. During the deformation, the resonator disk is subjected to either tension or compression on the 2 sides of the middle plane. According to the first-order perturbation integral [25], this antisymmetrical deformation has no effect on the resonant frequencies. However, the stretch of middle plane and the contraction of thickness cause a second-order (or nonlinear) frequency shift [26].

It is found that the resonant frequencies are affected by zero-order strains through the second- and third-order elastic stiffness coefficient, and also by first order strain gradients through the third-order elastic stiffness [17]. In other words, resonant frequency shift will be induced by the mechanical strain or stress. For a given flow rate in the flow path of the chamber, finite element analysis (FEA) was performed using ANSYS (ANSYS Inc., Canonsburg, PA), the results indicate that the magnitude of ΔP is significantly (around 3500 times) higher than τ_r. Thus ΔP could be the primary factor for resonant
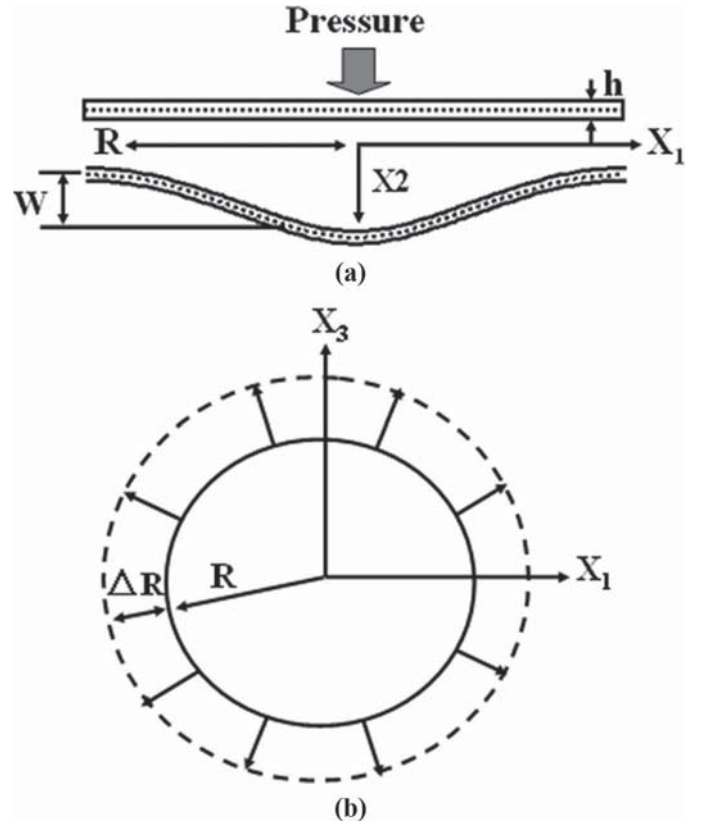
Fig. 5. Deflection of a quartz resonator disk subjected to normal pressure caused by fluid flow: (a) side view and (b) top view.

frequency shift of the quartz resonator, and the effect of τ_r on frequency change is then ignored in the following analysis.

In the theoretical analysis of force-frequency relationship for quartz resonators, the isotropic assumption is often made for the calculation of the stress distribution, and the results were found to be consistent with the experimental results [17], [27]. For the determination of the mechanical deflection of quartz resonators subjected to a steady-fluid flow rate, it is assumed that the quartz resonator is isotropic plate with Poisson's ratio υ, Young's modulus E, and thickness h_r. Thus, for an isotropic plate with clamped edge, the deflection w due to the uniform normal load ΔP on the surface can be obtained by [28]:

$$w = \frac{\Delta P}{64D}\left(R^2 - r^2\right)^2, \quad (6)$$

where $D = (Eh_r^3)/(12(1 - \upsilon^2))$ is the rigidity of the quartz plate, ΔP is the normal pressure difference across the thickness of resonator, R is radius, and r is the radial distance of the point of interest in the middle plane. Therefore, the radius of the middle plane will be elongated from R to $R + \Delta R$, as was schematically shown in Fig. 5(b), and ΔR is given by:

$$\Delta R = \int_0^R \left[\left(1 + \left(w' \right)^2 \right)^{1/2} - 1 \right] dr$$

$$\cong \int_0^R \frac{1}{2} \left(w' \right)^2 dr \tag{7}$$

$$= \frac{R^7}{6720 D^2} \Delta P^2.$$

The resonant frequency shift can be determined by the force-induced strain distribution [17], and the main terms for fundamental resonant frequency are given [26]:

$$\frac{\Delta f}{f} = A_1 \varepsilon_1^o + A_2 \varepsilon_2^o + A_3 \varepsilon_3^o, \tag{8}$$

where the coefficients A_1, A_2, and A_3 are determined by the second-order and third-order elastic constants; ε_1^o, ε_2^o, and ε_3^o are the initial strains of middle plain due to the pressure. Here, for estimation, the average strains are used [26], and the expression can be easily found for ε_1^o and ε_3^o :

$$\varepsilon_1^o = \varepsilon_3^o \cong \frac{\Delta R}{R} = \frac{R^6}{6720 D^2} \Delta P^2. \tag{9}$$

Because the normal stress along the thickness direction is approximately zero for a very thin plate, according to strain and stress relations, ε_2^o can be given:

$$\varepsilon_2^o = -\frac{C_{21}}{C_{22}} \varepsilon_1^o - \frac{C_{23}}{C_{22}} \varepsilon_3^o = -\frac{\left(C_{21} + C_{23} \right) R^6}{6720 C_{22} D^2} \Delta P^2, \tag{10}$$

where C_{ij} is the stiffness of quartz crystal.

From (1) to (10), the relationship between the fundamental resonant frequency shift and flow rate is found as:

$$\frac{\Delta f}{f} = \left[\left(A_1 + A_3 \right) - \left(\frac{C_{21} + C_{23}}{C_{22}} \right) A_2 \right] \frac{R^6}{6720 D^2} \Delta P^2$$

$$= \left[\left(A_1 + A_3 \right) - \left(\frac{C_{21} + C_{23}}{C_{22}} \right) A_2 \right] \frac{R^6}{6720 D^2}$$

$$\times \left(\frac{6 \mu L}{h^3 w \left(1 - \frac{192 h}{\pi^5 w} \sum_{n=1,3,5...}^{\infty} \frac{1}{n^5} \tanh \left(\frac{n \pi w}{2 h} \right) \right)} + \frac{8 \mu L_p}{\pi R_p^4} \right)^2 Q^2. \tag{11}$$

It can be seen from (4) that the normal pressure difference is proportional to the flow rate; and (8)–(10) show that the resonant frequency shift has a quadratic relationship with normal pressure difference. Thus, as shown in (11), the resonant frequency shift of quartz resonator caused by fluid flow is in a quadratic relation with the flow rate. For sensor design and application, it is often desirable to establish a linear or first-order transduction relationship between the measure and the output electrical signal. With frequency as the output signal, a nonlinear
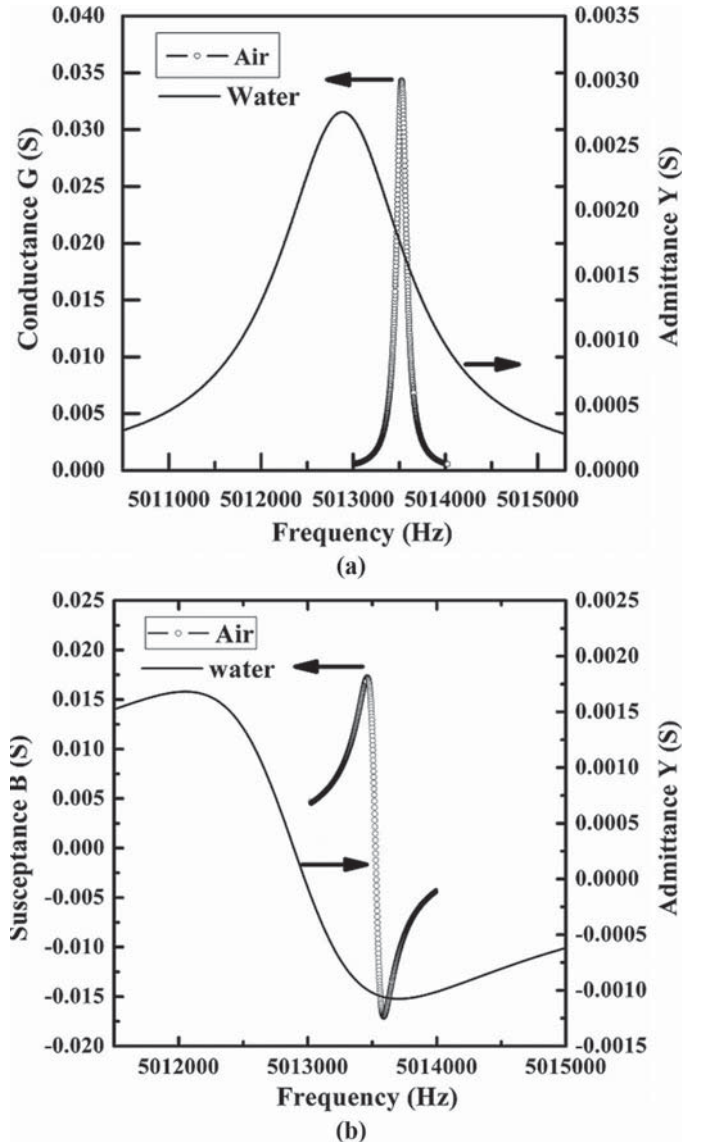
Fig. 6. Admittance (Y = G + jB) spectrum near fundamental resonant frequency in the air and water: (a) conductance G and (b) susceptance B.

relationship is still quite convenient for sensor applications.

III. Results and Discussion

The electrical admittance spectra of TSM quartz resonator are first measured in the air and deionized (DI) water with zero flow rate. Fig. 6 shows the admittance-frequency spectra of the resonator near the fundamental resonant frequency. G is conductance, the real part of admittance (Y), and B is susceptance, the imaginary part of admittance. It can be seen that resonant frequency is decreased due to the liquid load, and the spectrum is widened and the peak is greatly decreased due to increased viscous damping. The increased damping is reflected from the change of motional resistance (R) and mechanical Q of

the resonator. The motional resistance and Q factor of the resonator are found to be 29 Ω and 39477 in the air, and 362 Ω and 3077 in the water. The 1st resonance frequency shift due to water load is around 645 Hz, which is very close to the theoretical value 669 Hz calculated according to the Kanazawa equation [29], [30].

$$\Delta f = \frac{f_0^{\ 3/2}(\rho_L \eta_L)^{1/2}}{(\pi \rho_q \mu_q)^{1/2}}, \qquad (12)$$

where f_0, ρ_L, η_L, ρ_q, and μ_q are 1st resonant frequency in the air, density of liquid, viscosity of liquid, density of quartz, and piezoelectric stiffened shear modulus; $\rho_L = 1000$ (kgm^{-3}), $\eta_L = 8.7048 \times 10^{-4}$(Pa·s), $\rho_q = 2651$(kgm^{-3}), and $\mu_q = 2.947 \times 10^{10}$ (Nm^{-2}) were used for the calculation. The resonant frequency of resonator in the DI water with zero flow rate is used as the baseline for the frequency shift of device under different flow rates.

It is found that the flow variation due to the pulse pump makes the resonator admittance spectrum unstable under a certain flow rate, which induces some error in extracting resonant frequencies. Even when a pulse damper is adopted, the effect of flow variation can still be seen in the admittance spectrum, as shown in Fig. 7(a). To reduce the measurement noise, 5-times average values are taken for each data point in the electrical admittance-frequency spectrum, which is an average measurement algorithm provided by the precision impedance analyzer. From Fig. 7(b) it can be seen the admittance spectrum after average becomes stable and smooth, which improves the precision of extracting resonant frequency.

For flow measurement, 9 different flow rates (0, 375, 750, 1125, 1500, 1875, 2250, 2625, and 3000 mL/min) were chosen in the acoustic wave flow sensor test by justifying the pumping speed in the water circulation setup. Fig. 8 shows the frequency shifts for fundamental shear mode and higher order resonances of the quartz acoustic wave resonator under these flow rates. It can be seen that resonant frequency increases with flow rate. In addition, the peak value of conductance-frequency spectrum (G–f) has a different trend-to-flow rate for different modes. For the fundamental mode, the peak decreases for the first 8 flow rates and increases at the 9th flow rate. For the 3rd, 5th, and 7th modes, it seems that the G peak has not clear trend with the flow rate. For the 9th mode, the peak increases with the flow rate. Compared with conductance peak value, it is clear that the frequency shift is an indication of flow rate; thus, it can be used as the sensor output for the acoustic wave flow sensor.

Fig. 9 plots the results of different mode resonant frequency shifts versus flow rate. It is found that the resonant frequency shift has a nearly perfect quadratic relation with flow rate, agreeing very well with the prediction of (11). It is also found that the resonant frequency shifts of all the overtones are basically the same for a certain flow rate when compared in terms of fractional frequency
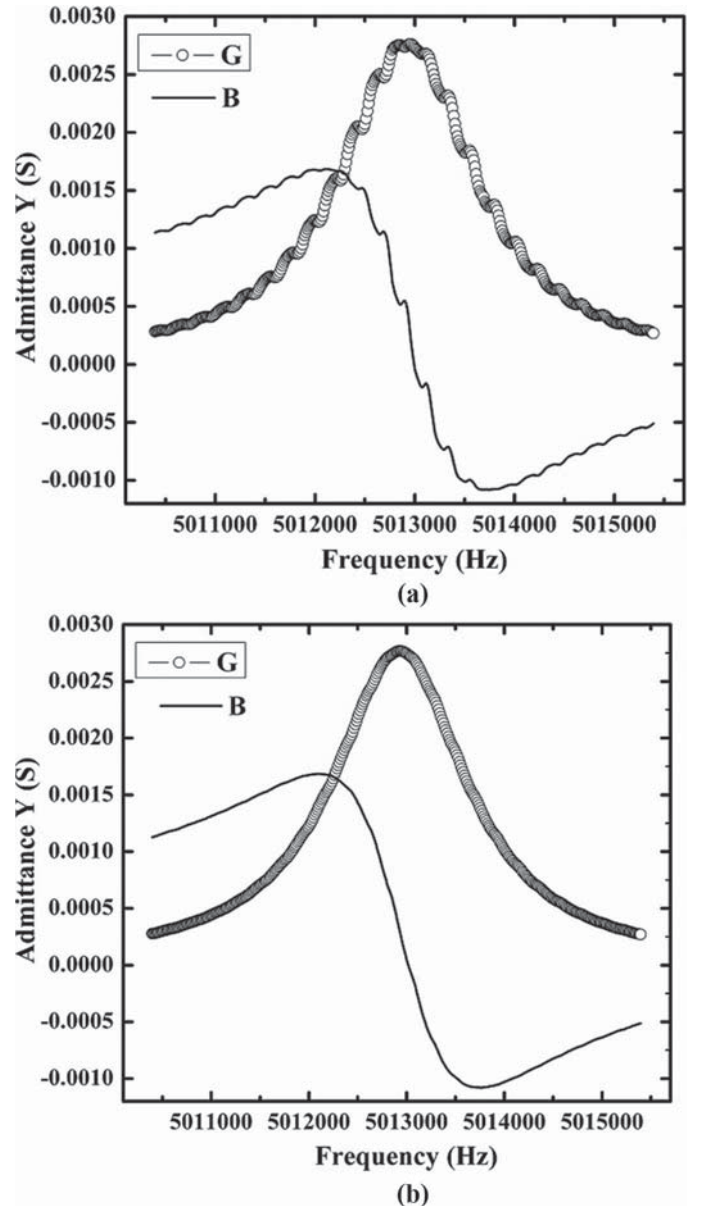
Fig. 7. Typical electrical admittance ($Y = G + jB$) spectra of quartz resonator flow sensor: (a) without average and (b) after 5-time average. G = conductance; B = susceptance.

shift ($\Delta f/f$). For example, the fractional frequency shifts of fundamental and overtones (3rd, 5th, 7th, and 9th) for a flow rate of 2250 mL/min are found to be 118, 127.6, 127.7, 127.6, and 127.2 ppm.

The repeatability of the resonator was also investigated. Nine flow rate levels were subsequently applied from 0 up to 3000 mL/min and from 3000 back to 0 mL/min. For each flow rate, the duration time is 1 min, and the resonant frequencies were monitored in real time through a LabVIEW program (National Instruments). Fig. 10 plots the result of the fundamental shear mode resonant frequency shift with time. It can be seen that the resonator has an excellent repeatability for different flow rates. Variations of the frequency shift with time are also observed, particularly under the 5th and 6th flow rate levels, which
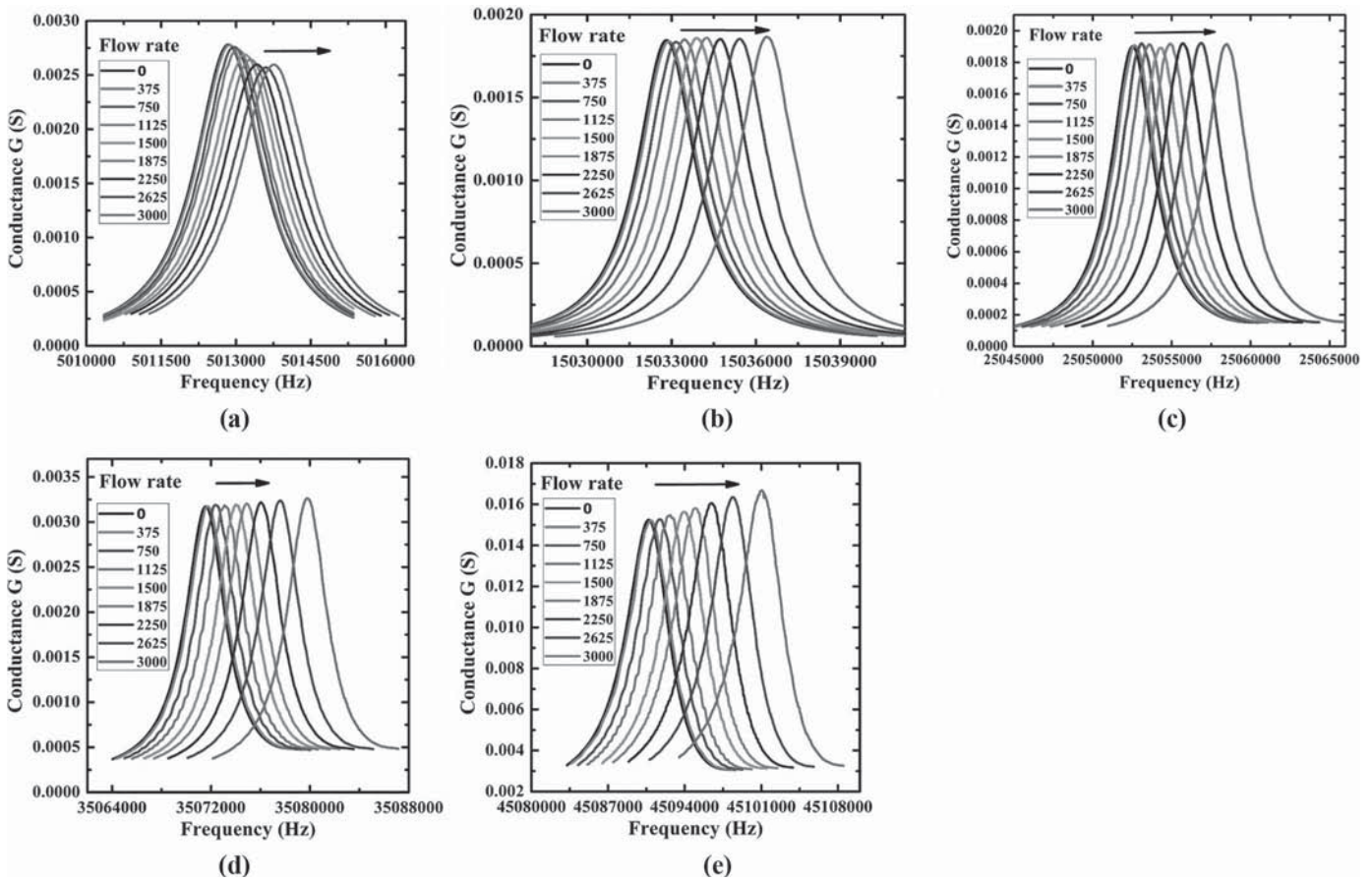
Fig. 8. Frequency shift of quartz resonator conductance spectrum under different flow rates: (a) 1st mode, (b) 3rd mode, (c) 5th mode, (d) 7th mode, and (e) 9th mode. Along the arrow direction, the flow rate increases from 0 to 3000 mL/min, and the conductance spectrum moves from left to right accordingly.
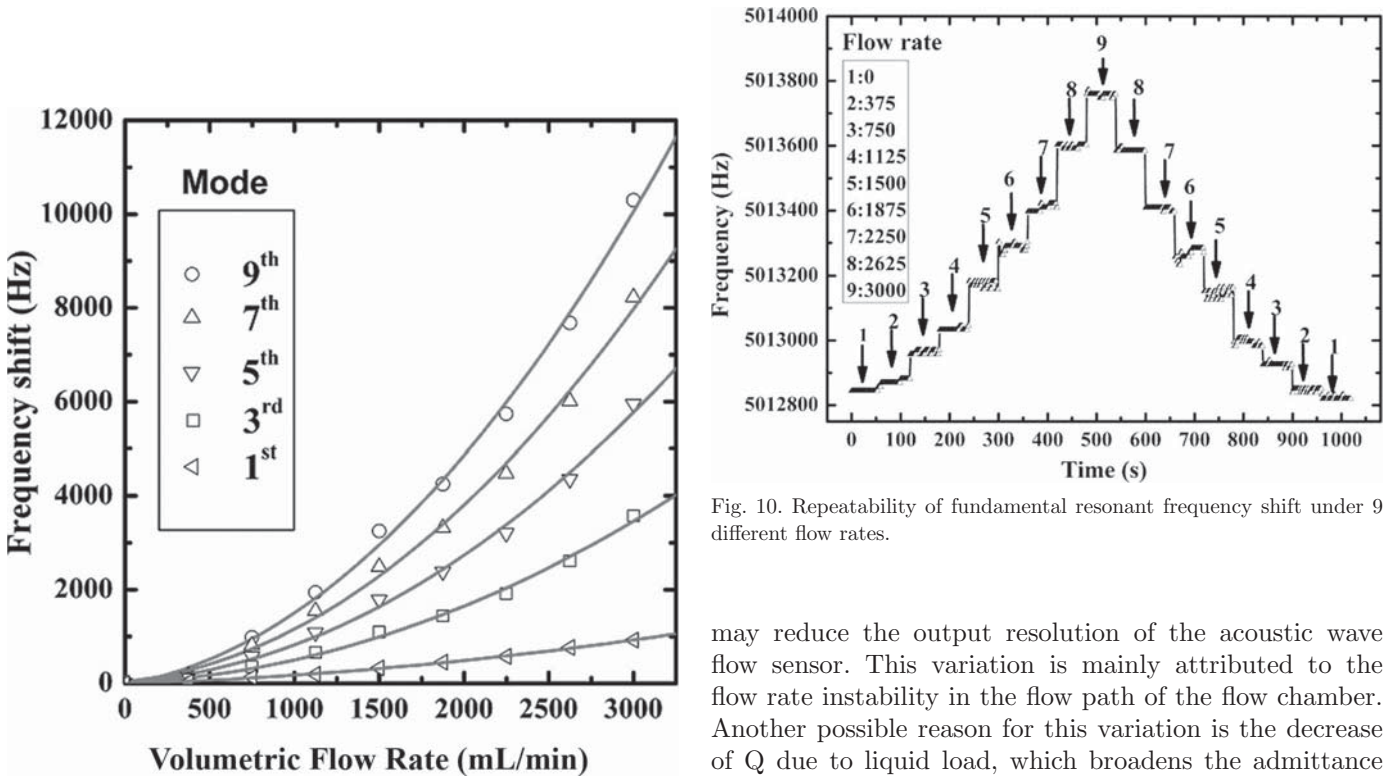

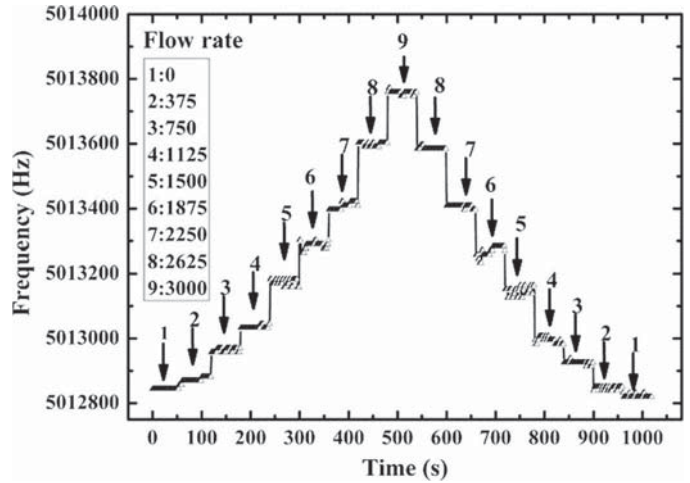Fig. 9. Resonant frequency shifts of fundamental mode and overtones versus flow rate.

Fig. 10. Repeatability of fundamental resonant frequency shift under 9 different flow rates.

may reduce the output resolution of the acoustic wave flow sensor. This variation is mainly attributed to the flow rate instability in the flow path of the flow chamber. Another possible reason for this variation is the decrease of Q due to liquid load, which broadens the admittance spectrum and makes it more difficult to identify the peak frequency of the spectrum because the resonant frequency

is extracted through searching the peak of conductance spectrum.

The experimental results indicate some attractive features of the TSM quartz acoustic wave flow sensor. One is its structural simplicity; no coating layer or other auxiliary sensing component is needed in the construction of the flow sensor cell. Another feature is that the operation of the acoustic wave flow sensor is very simple: the frequency shift of the quartz resonator is a convenient output that can be easily read by a simple oscillator circuit and frequency counter. In addition, a wide range of flow rates can be measured by using the quartz acoustic wave flow sensor. Moreover, for many industrial applications, one is interested, not in the resolution of flow rate, but in the threshold of flow rate or pressure for monitoring the operational parameters of electromechanical or energy systems. Thus, compared with the conventional expensive and complex flow-sensing devices, the acoustic wave flow sensor studied in this paper may provide an alternative method for flow-rate monitoring with substantially simple sensor cell structure and low operation cost.

It should be noticed that, before the practical implementation of this acoustic wave flow sensor, some issues need to be considered. Using the relationship between the flow pressure and flow rate given by (4), it is possible to extract the flow rate by the measurement of pressure at one point using a quartz resonator sensor. However, the flow rate measurement is also related to the outlet pressure [second term in (4)], which is often unknown in practical applications. Thus, to eliminate the effect of the outlet pressure, one approach is to introduce a fluid connection channel from the outlet to the other side of the quartz resonator such that the other side of the device is exposed to a hydrostatic pressure that is equal to the pressure at the outlet port. For this case, (4) and (11) will then be simplified as:

$$\Delta P = \frac{6Q\mu L}{h^3 w \left(1 - \frac{192h}{\pi^5 w} \sum_{n=1,3,5...}^{\infty} \frac{1}{n^5} \tanh\left(\frac{n\pi w}{2h}\right)\right)} \quad (13)$$

$$\frac{\Delta f}{f} = \left[(A_1 + A_3) - \left(\frac{C_{21} + C_{23}}{C_{22}}\right)A_2\right]\frac{R^6}{6720D^2} \\ \times \left(\frac{6\mu L}{h^3 w \left(1 - \frac{192h}{\pi^5 w} \sum_{n=1,3,5...}^{\infty} \frac{1}{n^5} \tanh\left(\frac{n\pi w}{2h}\right)\right)}\right)^2 Q^2. \quad (14)$$

Another approach is to adopt a dual resonator configuration: if 2 quartz TSM resonators are installed in the flow chamber with one side contacting liquid and another side exposed to air. Assuming they are located at $(x_1, h/2, 0)$ and $(x_2, h/2, 0)$, then, according to (1) and (11), one can get:

$$Q = \frac{h^3 w}{12\mu}\left(-\frac{dp}{dx}\right)\left(1 - \frac{192h}{\pi^5 w}\sum_{n=1,3,5...}^{\infty}\frac{1}{n^5}\tanh\left(\frac{n\pi w}{2h}\right)\right) \\ = -\frac{h^3 w}{12\mu}\left(1 - \frac{192h}{\pi^5 w}\sum_{n=1,3,5...}^{\infty}\frac{1}{n^5}\tanh\left(\frac{n\pi w}{2h}\right)\right)\frac{P(x_2) - P(x_1)}{x_2 - x_1}, \quad (15a)$$

$$\frac{\Delta f_1}{f_1} = \left[(A_1 + A_3) - \left(\frac{C_{21} + C_{23}}{C_{22}}\right)A_2\right]\frac{R^6}{6720D^2}\Delta P_1^2, \quad (15b)$$

$$\frac{\Delta f_2}{f_2} = \left[(A_1 + A_3) - \left(\frac{C_{21} + C_{23}}{C_{22}}\right)A_2\right]\frac{R^6}{6720D^2}\Delta P_2^2, \quad (15c)$$

where $P(x_i)$, ΔP_i, and $\Delta f_i/f_i$ are pressure at $x = x_i$ in the flow channel, pressure difference across the resonator thickness, and fractional frequency shift of the resonator. One can find:

$$P(x_2) - P(x_1) = \Delta P_2 - \Delta P_1. \quad (16)$$

Combining (15) and (16):

$$Q = -\frac{h^3 w}{12\mu(x_2 - x_1)}\left(1 - \frac{192h}{\pi^5 w}\sum_{n=1,3,5.....}^{\infty}\frac{1}{n^5}\tanh\left(\frac{n\pi w}{2h}\right)\right) \\ \times \frac{\left(\sqrt{\frac{\Delta f_2}{f_2}} - \sqrt{\frac{\Delta f_1}{f_1}}\right)}{\sqrt{\left[(A_1 + A_3) - \left(\frac{C_{21} + C_{23}}{C_{22}}\right)A_2\right]\frac{R^6}{6720D^2}}}. \quad (17)$$

From (17), it can be found that by using the dual resonator configuration, flow measurement is independent of outlet pressure and Q can be obtained by the frequency shift of 2 resonators.

The sensitivity of the TSM quartz acoustic wave flow sensor seems not as high as the flow sensors based on SAW device, which has a frequency shift greater than 142 kHz (1900 ppm) for gas flow rate in the range from 0 to 1000 mL/min [6]. The experimental results in this work show for 1000 mL/min flow rate a frequency shift less 190 Hz (40 ppm) for the fundamental shear mode resonance and 2000 Hz (43 ppm) for the 9th mode. This is because a nonlinear (second-order effect) frequency shift of the quartz resonator is used for the signal transduction, which is usually much smaller than a linear effect. The 9th overtone has a frequency shift of 10 300 Hz (228 ppm) for 3000 mL/min flow rate, which is equivalent to 0.076 ppm/(mL/min). Assuming that the quartz resonator sensor has a temperature dependent noise level of 1 ppm on the frequency shift, the calculated resolution for the flow sensor is about 13 mL/min.

It should also be noted that theoretically this acoustic wave flow sensor is applicable to the flow rate measurement for any type of fluid such as air, oil, and others.

Other conduit materials and geometry may be used for the fabrication of the flow sensor structures to meet the need of specific applications, as long as the fluid pressure is not high enough to cause the failure of thin quartz resonator disk.

In addition, because the resonant behavior can be affected by the chemical reactions or physical adsorption occurring on the resonator electrode, the electrode facing the fluid needs to be protected, particularly when it is exposed to reactive or abrasive fluid. For this purpose, in the measurement of abrasive fluids, the electrode material should be anti-abrasive or a protective thin film needs to be coated on the electrode of the resonator sensor. Further study is also needed to investigate the resonator behavior under higher pressure levels and determine the maximum pressure that the resonator can endure for long-term use, because the highest pressure in the experiment study is about 6×10^4 Pa, which is quite moderate as compared with many practical applications. Furthermore, it is well known that the flow is laminar and the velocity profile is parabolic for low Reynolds numbers (generally under 2000), and the flow becomes turbulent for Reynolds numbers over 4000. The Reynolds numbers of the current experiments spanned from 0 to 822, therefore, experiments at high Reynolds numbers are still needed to investigate the influence of the turbulent flow profile on the resonator response.

IV. Conclusion

In this paper, a TSM quartz resonator was studied as a flow sensor to measure the liquid flow rate. A special flow sensor structure was designed and constructed, and the theoretical relationship between the quartz resonator frequency shift and flow rate was derived. Both theoretical and experimental results have indicated that the frequency shift of quartz resonator caused by fluid flow can be attributed to the nonlinear (quadratic) frequency response of the device due to the normal pressure imposing on the sensor disk through the fluid flow. The resonant frequencies of different modes can be used as the sensor output for flow rate monitoring, and the fundamental, 3rd, 5th, 7th, and 9th mode resonant frequency shifts were found to be around 920, 3572, 5947, 8228, and 10 300 Hz for flow rate variations from 0 to 3000 mL/min or a Reynolds number change from 0 to 822. To obtain the flow rate by measuring the pressure drop across the quartz resonator disk using a single resonator sensor configuration, the effect of the outlet pressure needs to be eliminated. It is proposed that a fluid connection channel from the outlet to the other side of the quartz resonator can be introduced such that the other surface of the device is exposed to a hydrostatic pressure that is equal to the pressure at the outlet port. Another approach for flow rate measurement is to use dual-sensor configuration, in which 2 quartz resonators are installed in the flow chamber along the flow channel. The relative frequency shifts of the 2 resonators will be directly related to the flow rate, and independent of the outlet pressure. In addition, considering that the resonant behavior can be affected by the chemical reactions or physical adsorption occurring on the resonator electrode, the electrode facing the fluid may need to be protected, particularly when it is exposed to reactive or abrasive fluids. Further experiment studies under higher pressure and high Reynolds numbers are needed to determine the pressure limit and the flow profile influence on resonator response.

References

[1] R. W. Miller, *Flow Measurement Engineering Handbook*, 2nd ed. New York: New York, 1989.

[2] L. C. Lynnworth, *Ultrasonic Measurements for Process Control*. New York: Academic Press, 1989.

[3] K. Shirai, T. Pfister, L. Büttner, J. Czarske, H. Müller, S. Becker, H. Lienhart, and F. Durst, "Highly spatially resolved velocity measurements of a turbulent channel flow by a fiber-optic heterodyne laser-Doppler velocity-profile sensor," *Exp. Fluids*, vol. 40, pp. 473–481, 2006.

[4] C. G. Lomas, *Fundamentals of Hot Wire Anemometry*. New York: Cambridge University Press, 1986.

[5] D. S. Ballantine, Jr., R. M. White, S. J. Martin, A. J. Ricco, G. C. Frye, E. T. Zellars, H. Wohltjen, *Acoustic Wave Sensors: Theory, Design, and Physico-Chemical Applications*, San Diego, Academic, 1997.

[6] S. G. Joshi, "Surface-acoustic-wave (SAW) flow sensor," *IEEE Trans. Ultrason. Ferroelectr. Freq. Control*, vol. 38, pp. 148–154, Mar. 1991.

[7] D. Rebière, "Acoustic wave devices to measure gas flow: Comparison between surface acoustic wave (SAW) and shear horizontal acoustic plate mode (SH-APM) oscillators," *Sens. Actuators A*, vol. 42, pp. 384–388, Apr. 1994.

[8] D. A. Buttry and M. D. Word, "Measurement of interfacial processes at electrode surfaces with the electrochemical quartz crystal microbalance," *Chem. Rev.*, vol. 92, pp. 1355–1379, Jun. 1992.

[9] L. Qin, H. Cheng, J. M. Li, and Q.-M. Wang, "Characterization of polymer nanocomposite films using quartz thickness shear mode (TSM) acoustic wave sensor," *Sens. Actuators A*, vol. 136, pp. 111–117, May 2007.

[10] F. Li, J. H.-C. Wang, and Q.-M. Wang, "Thickness shear mode acoustic wave sensors for characterizing the viscoelastic properties of cell monolayer," *Sens. Actuators B*, vol. 128, pp. 399–406, Jan. 2008.

[11] A. Janshoff, H.-J. Galla, and C. Steinem, "Piezoelectric mass-sensing devices as biosensors—An alternative to optical biosensors?" *Angew. Chem. Int. Ed.*, vol. 39, pp. 4004–4032, Nov. 2000.

[12] K. A. Marx, "Quartz crystal microbalance: A useful tool for studying thin polymer films and complex biomolecular systems at the solution-surface interface," *Biomacromolecules*, vol. 4, pp. 1099–1120, Sep.–Oct. 2003.

[13] A. D. Ballato and R. Bechmann, "Effect of initial stress in vibrating quartz plates," in *Proc. IRE*, vol. 48, 1960, pp. 261–262.

[14] A. Ballato, E. P. EerNisse, and T. Lukaszek, "The force–frequency effect in doubly rotated quartz resonators," in *Proc. 31st Ann. Symp. Frequency Control*, 1977, pp. 8–16,.

[15] J. M. Ratajski, "Forced-frequency coefficient of singly-rotated vibrating quartz crystals," *IBM J. Res. Develop.*, vol. 12, pp. 92–96, 1968.

[16] P. C. L. Lee, Y. S. Wang, and X. Markenscoff, "High frequency vibrations of crystal plates under initial stresses," *J. Acoust. Soc. Am.*, vol. 57, pp. 95–105, Jan. 1975.

[17] P. C. Y. Lee, Y. S. Wang, and X. Markenscoff, "Nonlinear effects of initial bending on the vibrations of crystal plates," *J. Acoust. Soc. Am.*, vol. 59, pp. 90–96, Jan. 1976.

[18] L. D. Clayton and E. P. EerNisse, "Frequency shift calculations for quartz resonators," in *Proc. 45th Annu. Symp. Frequency Control*, 1991, pp. 309–320.

[19] Z. Wang, Y. Dong, H. Zhu, and G. Feng, "Effect of transverse force on the performance of quartz resonator force sensors," *IEEE Trans. Ultrason. Ferroelectr. Freq. Control*, vol. 51, pp. 470–476, Apr. 2004.

[20] B. Jakoby, H. Eisenschmid, and F. Herrmann, "The potential of microacoustic SAW and BAW-based sensors for automotive applications—A Review," *IEEE Sens. J.*, vol. 2, no. 5, pp. 443–452, Oct. 2002.

[21] P. Errol, E. P. EerNisse, and R. B. Wiggins, "Review of thickness-shear mode quartz resonator sensors for temperature and pressure," *IEEE Sens. J.*, vol. 1, no. 1, pp. 79–87, Jun. 2001.

[22] H. E. Karrer and J. Leach, "A quartz resonator pressure transducer," *IEEE Trans. Ind. Electron. Contr. Instrumen.*, vol. IECI-16, no. 1, Jul. 1969.

[23] B. J. Chung, A. M. Robertson, and D. G. Peters, "The numerical design of a parallel plate flow chamber for investigation of endothelial cell response to shear stress," *Comput. Struc.*, vol. 81, pp. 535–546, May 2003.

[24] C.-S. Yih, *Fluid Mechanics*, rev. ed. Ann Arbor, MI: West River Press, 1979.

[25] H. F. Tiersten, "Perturbation theory for linear electroelastic equations for small fields superposed on a bias," *J. Acoust. Soc. Am.*, vol. 64, pp. 832–837, Sep. 1978.

[26] J. Yang and S. Guo, "An estimate on the second-order normal acceleration sensitivity of a quartz resonator," *IEEE Trans. Ultrason. Ferroelectr. Freq. Control*, vol. 53, pp. 1562–1563, Sep. 2006.

[27] D. Janiaud, L. Nissim, and J.-J. Gagnepain, "Analytical calculation of initial stress effects on anisotropic crystals: Application to quartz resonators," in *Proc. 32nd Annu. Symp. Frequency Control*, 1978, pp. 169–179.

[28] S. Timoshenko and S. Woinowsky-Krieger, *Theory of Plates and Shells*, 2nd ed. New York: McGraw-Hill, 1959, pp. 55–56.

[29] K. K. Kanazawa and J. G. Gordon II, "Frequency of a quartz microbalance in contact with liquid," *Anal. Chem.*, vol. 57, pp. 1770–1771, Jul. 1985.

[30] R. Lucklum and P. Hauptmann, "Transduction mechanism of acoustic-wave based chemical and biochemical sensors," *Meas. Sci. Technol.*, vol. 14, pp. 1854–1864, Sep. 2003.
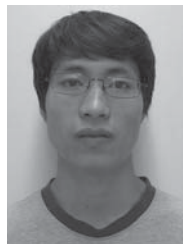
Lifeng Qin was born in Dongyang, Zhejiang, China, in 1979. He earned B.S. and M.S. degrees from the Department of Biomedical Engineering at Zhejiang University, Hangzhou, Zhejiang, China, in 2002 and 2005, respectively. He is currently a Ph.D. candidate in the Department of Mechanical Engineering and Materials Science at the University of Pittsburgh, Pittsburgh, PA.

He has been working as a research assistant at the University of Pittsburgh since 2005. His primary research interests include biosensors, piezoelectric devices for characterizing mechanical properties of thin films, and surface acoustic wave (SAW) and bulk acoustic wave (BAW) sensor applications.
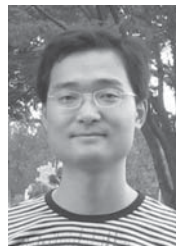
Zijing Zeng was born in Xinyuan, Xinjiang, China, in 1982. He earned his B.E. degree from the Department of Automotive Engineering at Tsinghua University, Beijing, China, in 2005. He is currently a Ph.D. candidate in the Department of Mechanical Engineering and Materials Science (MEMS) at the University of Pittsburgh, Pittsburgh, PA.

He is currently working as a research assistant in the Complex Biofluid and Tissue Lab at MEMS. His primary research interests include hemodynamics, computational fluid dynamics, and cerebral aneurysm diseases; his research work is also related to experimental and medical device design.

Hongbin Cheng received his B.S and M.S degrees from Tsinghua University, Beijing, China, in 1995 and 1998, respectively. He is currently a Ph.D. candidate in the Department of Mechanical Engineering, University of Pittsburgh, Pittsburgh, PA. His primary research interests include piezoelectric devices for sensor and actuator applications, nanofabrication, and applications.

Qing-Ming Wang (M'00) is an associate professor in the Department of Mechanical Engineering and Materials Science, University of Pittsburgh, Pittsburgh, PA. He received B.S. and M.S. degrees in materials science and engineering from Tsinghua University, Beijing, China, in 1987 and 1989, respectively, and the Ph.D. degree in materials from Pennsylvania State University, State College, PA, in 1998.

Prior to joining the University of Pittsburgh, Dr. Wang was an R&D engineer and materials scientist in Lexmark International, Inc., Lexington, KY, where he worked on piezoelectric and electrostatic microactuators for inkjet printhead development. From 1990 to 1992, he worked as a development engineer in a technology company in Beijing where he participated in the research and development of electronic materials and piezoelectric devices. From 1992 to 1994, he was a research assistant in the New Mexico Institute of Mining and Technology working on nickel-zinc ferrite and ferrite/polymer composites for EMI filter application. From 1994 to 1998, he was a graduate assistant in the Materials Research Laboratory at Pennsylvania State University working toward his Ph.D. degree in the areas of piezoelectric ceramic actuators for low frequency active noise cancellation and vibration damping and thin-film materials for microactuator and microsensor applications.

Dr.Wang's primary research interests are in microelectromechanical systems (MEMS) and microfabrication; thin-film bulk acoustic wave resonators (FBAR) and acoustic wave sensors; functional nanomaterials and devices; and piezoelectric and electrostrictive thin films and composites for transducer, actuator, and sensor applications.

He is a member of IEEE, IEEE-UFFC, the Materials Research Society (MRS), ASME, and the American Ceramic Society.

Vibration Characteristics of a Circular Cylindrical Panel Piezoelectric Transducer

Zengtao Yang, Jiashi Yang, *Senior Member, IEEE*, Yuantai Hu, and Qing-Ming Wang, *Member, IEEE*

Abstract—We study the theory of the basic vibration characteristics of a circular cylindrical shell piezoelectric transducer. The linear theory of piezoelectricity is used. Both the free-vibration solution for resonant frequencies and modes as well as the electrically forced-vibration solution for admittance are obtained. Numerical results are presented.

I. Introduction

PIEZOELECTRIC materials are frequently used for making electromechanical transducers of various shapes. We are interested in circular cylindrical shell piezoelectric transducers to be attached to circular cylindrical structures for exciting and detecting acoustic waves. It is part of our effort in the development of electromechanical transducers for nondestructive evaluation (NDE) of circular cylindrical elastic structures, in particular the circular cylindrical pressure vessels in nuclear reactors. Existing theoretical results on circular cylindrical piezoelectric transducers are mostly for full cylinders, e.g. [1]–[14], but the application we are interested in requires knowledge of vibration characteristics of a finite portion of a circular cylinder. There are limited results on vibrations of finite circular cylindrical piezoelectric panels [15], [16] where mixed boundary conditions are chosen in a particular way so that analytical solutions are possible, but the mixed mechanical boundary conditions treated are different from typical situations in our applications. There are also extensive results on circular cylindrical piezoelectric shells for smart structural applications [17] where approximate, 2-D structural theories are used. Results from smart structural analyses are for the so-called low-frequency modes of extension and flexure, etc. They are insufficient for NDE where the so-called high-frequency thickness modes [18] are usually used, for which analyses based on the exact 3-D equations are necessary. In this paper, we formulate a problem of finite circular cylindrical shell piezoelectric transducers that is relevant to NDE of circular cylindrical structures and perform a theoretical analysis on these transducers.

II. Governing Equations

Consider a portion of a circular cylindrical shell with inner radius a and outer radius b as shown in Fig. 1. The 2 radii going through the edges of the shell form an angle 2β; β is less than π and is otherwise arbitrary. The shell is unbounded in the z direction determined by the right-hand rule from the x and y axes in the figure. Only a cross section of the shell is shown. The material of the shell is ceramics poled in the z direction. A cylindrical coordinate system is defined by $x = r\cos\theta$, $y = r\sin\theta$, and $z = z$. In the index notation below, (x,y,z) correspond to $(1,2,3)$.

We consider the so-called antiplane or shear horizontal (SH) vibration with [19], [20]

$$u_1 = u_2 = 0, \quad u_3 = u(x_1, x_2, t), \quad \phi = \phi(x_1, x_2, t), \quad (1)$$

where u_i is the displacement vector and φ is the electric potential. Modes described by (1) are allowed by the 3-D equations of linear piezoelectricity. For these modes, the 3-D equations of linear piezoelectricity reduce to a 2-D mathematical problem. Corresponding to the displacement and potential fields in (1), the nonvanishing strain and electric field components are

$$\begin{Bmatrix} 2S_{13} \\ 2S_{23} \end{Bmatrix} = \nabla u, \quad \begin{Bmatrix} E_1 \\ E_2 \end{Bmatrix} = -\nabla\phi, \quad (2)$$

where $\nabla = \mathbf{i}_1\partial_1 + \mathbf{i}_2\partial_2$ is the 2-D gradient operator. For ceramics poled in the x_3 direction, the nontrivial components of T_{ij} and D_i are

$$\begin{Bmatrix} T_{13} \\ T_{23} \end{Bmatrix} = c\nabla u + e\nabla\phi, \quad \begin{Bmatrix} D_1 \\ D_2 \end{Bmatrix} = e\nabla u - \varepsilon\nabla\phi, \quad (3)$$

where we have denoted the relevant elastic, piezoelectric, and dielectric constants by $c = c_{44}$, $e = e_{15}$, and $\varepsilon = \varepsilon_{11}$. The nontrivial equation of motion and the charge equation of electrostatics take the following form:

$$c\nabla^2 u + e\nabla^2\phi = \rho\ddot{u}, \quad e\nabla^2 u - \varepsilon\nabla^2\phi = 0. \quad (4)$$

We introduce [19], [20]
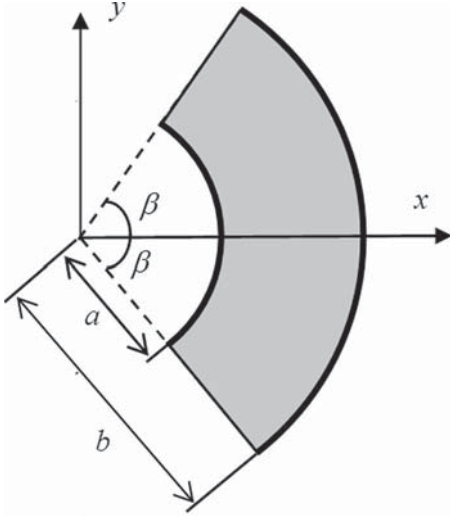
$$\psi = \phi - \frac{e}{\varepsilon}u. \quad (5)$$

Fig. 1. A circular cylindrical shell piezoelectric transducer.

Then, in terms of u and ψ,

$$T_{23} = \overline{c}u_{,2} + e\psi_{,2}, \quad T_{31} = \overline{c}u_{,1} + e\psi_{,1},$$
$$D_1 = -\varepsilon\psi_{,1}, \quad D_2 = -\varepsilon\psi_{,2}, \tag{6}$$

and

$$v_T^2 \nabla^2 u = \ddot{u}, \quad \nabla^2 \psi = 0, \tag{7}$$

where

$$v_T^2 = \frac{\overline{c}}{\rho}, \quad \overline{c} = c + \frac{e^2}{\varepsilon} = c(1 + k^2), \quad k^2 = \frac{e^2}{\varepsilon c}. \tag{8}$$

In polar coordinates, (7) takes the form

$$v_T^2 \left(\frac{\partial^2 u}{\partial r^2} + \frac{1}{r}\frac{\partial u}{\partial r} + \frac{1}{r^2}\frac{\partial^2 u}{\partial \theta^2} \right) = \ddot{u},$$
$$\frac{\partial^2 \psi}{\partial r^2} + \frac{1}{r}\frac{\partial \psi}{\partial r} + \frac{1}{r^2}\frac{\partial^2 \psi}{\partial \theta^2} = 0. \tag{9}$$

Mechanically the boundaries are all traction-free. Electrically the boundaries at $\theta = \pm\beta$ are unelectroded. The boundaries at $r = a$, b may be either electroded or unelectroded. We will consider time-harmonic modes and use the complex notation. All fields are with an $\exp(i\omega t)$ factor that will be dropped for convenience.

III. Free Vibration

According to whether u and ψ are even or odd functions of θ, we classify the modes into symmetric and antisymmetric. First, consider the following symmetric modes:

$$u = u(r)\cos\nu\theta, \quad \psi = \psi(r)\cos\nu\theta. \tag{10}$$

Substitution of (10) into (9) results in

$$\frac{\partial^2 u}{\partial r^2} + \frac{1}{r}\frac{\partial u}{\partial r} + \left(\xi^2 - \frac{\nu^2}{r^2}\right)u = 0, \tag{11a}$$

$$\frac{\partial^2 \psi}{\partial r^2} + \frac{1}{r}\frac{\partial \psi}{\partial r} - \frac{\nu^2}{r^2}\psi = 0, \tag{11b}$$

where we have denoted

$$\xi = \frac{\omega}{v_T}. \tag{12}$$

Eq. (11a) can be written as Bessel's equations of order ν; (11b) allows a simple power function solution. Then, when $\nu \neq 0$,

$$u = [CJ_\nu(\xi r) + DY_\nu(\xi r)]\cos\nu\theta,$$
$$\psi = [Fr^\nu + Gr^{-\nu}]\cos\nu\theta, \tag{13a}$$

where J_ν and Y_ν are the νth order Bessel functions of the first and second kind. C, D, F, and G are undetermined constants. When $\nu = 0$, we have

$$u = CJ_0(\xi r) + DY_0(\xi r),$$
$$\psi = F\ln r + G. \tag{13b}$$

The other fields are then given by ($\nu \neq 0$):

$$\begin{aligned}
\phi &= \psi + \frac{e}{\varepsilon}u \\
&= \left[\frac{e}{\varepsilon}CJ_\nu(\xi r) + \frac{e}{\varepsilon}DY_\nu(\xi r) + Fr^\nu + Gr^{-\nu}\right]\cos\nu\theta, \\
T_{rz} &= \overline{c}u_{,r} + e\psi_{,r} \\
&= [\overline{c}\xi CJ'_\nu(\xi r) + \overline{c}\xi DY'_\nu(\xi r) \\
&\quad + e\nu Fr^{\nu-1} - e\nu Gr^{-\nu-1}]\cos\nu\theta, \\
T_{\theta z} &= \overline{c}\frac{1}{r}u_{,\theta} + e\frac{1}{r}\psi_{,\theta} \\
&= -\frac{\nu}{r}[\overline{c}CJ_\nu(\xi r) + \overline{c}DY_\nu(\xi r) + eFr^\nu + eGr^{-\nu}]\sin\nu\theta, \\
D_r &= -\varepsilon\psi_{,r} = [-\varepsilon\nu Fr^{\nu-1} + \varepsilon\nu Gr^{-\nu-1}]\cos\nu\theta, \\
D_\theta &= -\varepsilon\frac{1}{r}\psi_{,\theta} = \varepsilon\frac{\nu}{r}[Fr^\nu + Gr^{-\nu}]\sin\nu\theta,
\end{aligned} \tag{14a}$$

or, when $\nu = 0$:

$$\phi = \psi + \frac{e}{\varepsilon}u = \frac{e}{\varepsilon}[CJ_0(\xi r) + DY_0(\xi r)] + F\ln r + G,$$

$$T_{rz} = \overline{c}u_{,r} + e\psi_{,r} = -\overline{c}\xi[CJ_1(\xi r) + DY_1(\xi r)] + e\frac{F}{r},$$

$$D_r = -\varepsilon\psi_{,r} = -\varepsilon\frac{F}{r}. \tag{14b}$$

For traction-free and unelectroded edges at $\theta = \pm\beta$, we must have $T_{\theta z} = 0$ and $D_\theta = 0$, which implied that

$$u_{,\theta} = 0, \quad \psi_{,\theta} = 0, \quad \theta = \pm\beta. \tag{15}$$

From (15) we obtain

$$\sin\nu\beta = 0, \quad \nu\beta = m\pi, \quad \nu = \nu_m = \frac{m\pi}{\beta}, \quad m = 0,1,2,\cdots. \tag{16}$$

Similarly, for antisymmetric modes, we have

$$\cos\nu\beta = 0, \quad \nu\beta = \left(m + \frac{1}{2}\right)\pi,$$
$$\nu = \nu_m = \left(m + \frac{1}{2}\right)\frac{\pi}{\beta}, \quad m = 0,1,2,\cdots. \tag{17}$$

For antisymmetric modes $\nu \neq 0$. We will discuss unelectroded and electroded transducers separately below.

A. Unelectroded Transducer

For traction-free and unelectroded boundaries at $r = a,b$, we must have $T_{rz} = 0$ and $D_r = 0$, or, equivalently,

$$u_{,r} = 0, \quad \psi_{,r} = 0, \quad r = a,b. \tag{18}$$

Then, when $\nu \neq 0$ or $m \neq 0$, we have

$$C\xi J'_{\nu_m}(\xi a) + D\xi Y'_{\nu_m}(\xi a) = 0,$$
$$F\nu_m a^{\nu_m - 1} - G\nu_m a^{-\nu_m - 1} = 0,$$
$$C\xi J'_{\nu_m}(\xi b) + D\xi Y'_{\nu_m}(\xi b) = 0,$$
$$F\nu_m b^{\nu_m - 1} - G\nu_m b^{-\nu_m - 1} = 0, \tag{19a}$$

or, when $m = 0$:

$$-\overline{c}\xi[CJ_1(\xi a) + DY_1(\xi a)] + e\frac{F}{a} = 0,$$
$$-\overline{c}\xi[CJ_1(\xi b) + DY_1(\xi b)] + e\frac{F}{b} = 0,$$
$$-\varepsilon\frac{F}{a} = 0,$$
$$-\varepsilon\frac{F}{b} = 0. \tag{19b}$$

For nontrivial solutions of C, D, F, or G, the determinant of the coefficient matrix of (19a) or (19b) must vanish, which gives the frequency equation that determines the resonant frequencies. We note that lines 1 and 3 in (19a) are not coupled to lines 2 and 4 in (19a). Therefore the frequency equation determined by (19a) can be factored into 2

$$\begin{vmatrix} \xi J'_{\nu_m}(\xi a) & \xi Y'_{\nu_m}(\xi a) \\ \xi J'_{\nu_m}(\xi b) & \xi Y'_{\nu_m}(\xi b) \end{vmatrix} = 0, \tag{20a}$$

$$\begin{vmatrix} \nu_m a^{\nu_m - 1} & -\nu_m a^{-\nu_m - 1} \\ \nu_m b^{\nu_m - 1} & -\nu_m b^{-\nu_m - 1} \end{vmatrix} = 0. \tag{20b}$$

Eq. (20b) has no solution because $m \neq 0$. In the case of (19b), we have $F = 0$, which implies a constant ψ. In practice, we are more interested in the case of an electroded plate below.

B. Electroded Transducer

When the transducer is electroded at $r = a$, b and the electrodes are shorted, the electrical boundary conditions at $r = a$, b are that $\varphi = 0$. When $m \neq 0$, we have

$$\frac{e}{\varepsilon}CJ_{\nu_m}(\xi a) + \frac{e}{\varepsilon}DY_{\nu_m}(\xi a) + Fa^{\nu_m} + Ga^{-\nu_m} = 0,$$
$$\overline{c}\xi CJ'_{\nu_m}(\xi a) + \overline{c}\xi DY'_{\nu_m}(\xi a) +$$
$$e\nu_m Fa^{\nu_m - 1} - e\nu_m Ga^{-\nu_m - 1} = 0,$$
$$\frac{e}{\varepsilon}CJ_{\nu_m}(\xi b) + \frac{e}{\varepsilon}DY_{\nu_m}(\xi b) + Fb^{\nu_m} + Gb^{-\nu_m} = 0,$$
$$\overline{c}\xi CJ'_{\nu_m}(\xi b) + \overline{c}\xi DY'_{\nu_m}(\xi b) +$$
$$e\nu_m Fb^{\nu_m - 1} - e\nu_m Gb^{-\nu_m - 1} = 0. \tag{21a}$$

When $m = 0$ we have

$$-\overline{c}\xi[CJ_1(\xi a) + DY_1(\xi a)] + e\frac{F}{a} = 0,$$
$$-\overline{c}\xi[CJ_1(\xi b) + DY_1(\xi b)] + e\frac{F}{b} = 0,$$
$$\frac{e}{\varepsilon}[CJ_0(\xi a) + DY_0(\xi a)] + F\ln a + G = 0,$$
$$\frac{e}{\varepsilon}[CJ_0(\xi b) + DY_0(\xi b)] + F\ln b + G = 0. \tag{21b}$$

The frequency equation is obtained by setting the determinant of the coefficient matrix of (21a) or (21b) to zero.

C. Numerical Results

As a numerical example, for geometric parameters we choose $a = 0.2$ m, $b = 0.21$ m, $\beta = \pi/6$. For the material, we consider PZT-7A [21] with $\rho = 7600$ kg/m^3, $c_{44} = 2.53 \times 10^{10}$ N/m^2, $e_{15} = 9.2$ C/m^2, $\varepsilon_{11} = 0.407 \times 10^{-8}$ C/Vm.

Fig. 2 shows resonant frequencies versus m; m is effectively the wave number in the θ direction. Therefore, in Fig. 2, if the dots are properly connected in the horizontal direction, the resulting curves resemble the dispersion curves of SH waves in plates or circular cylindrical shells, but here the wave number and frequencies are discrete. Frequencies with $m = 0$ are called thickness-shear frequencies whose modes have no θ dependence. When m is positive, the frequencies are called thickness-twist frequencies whose modes have θ dependence.
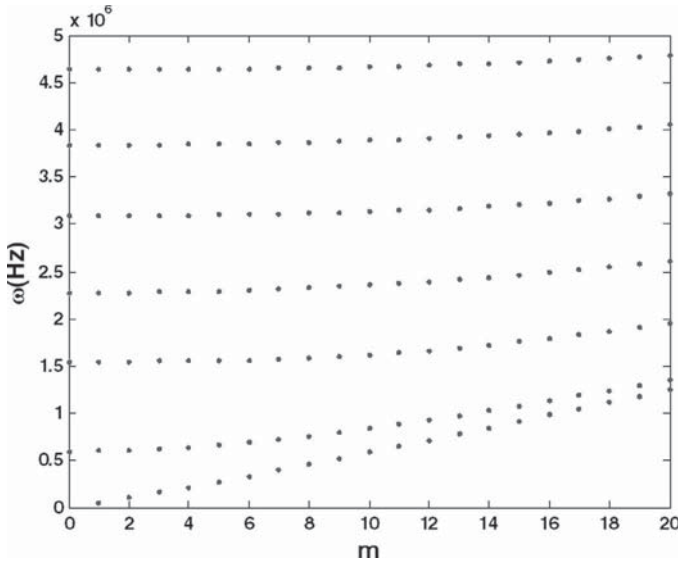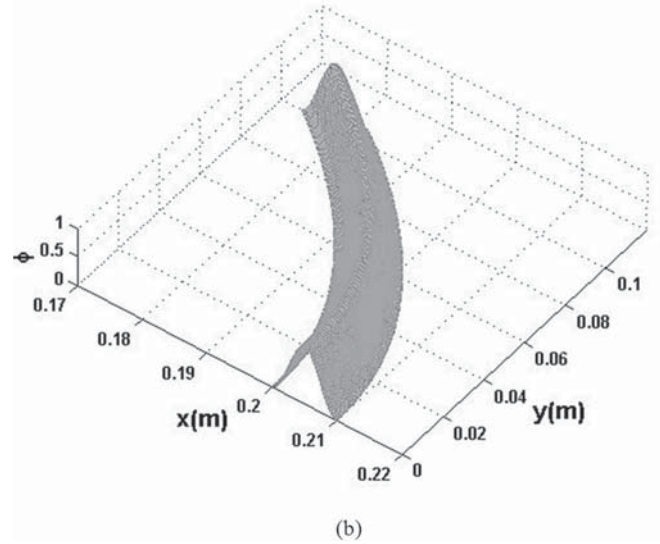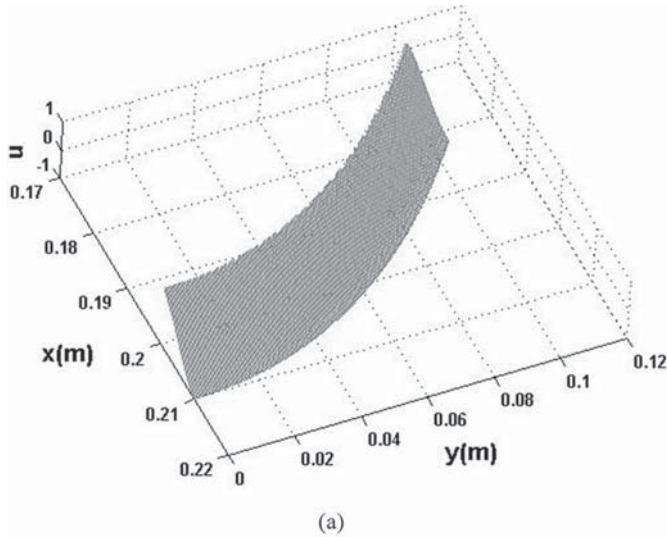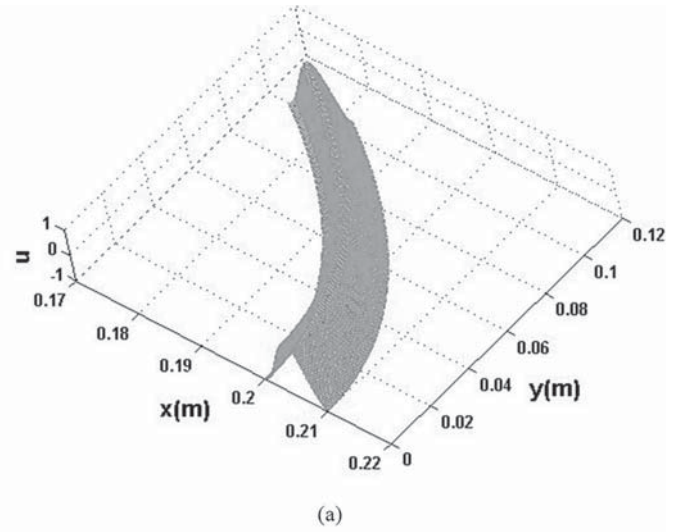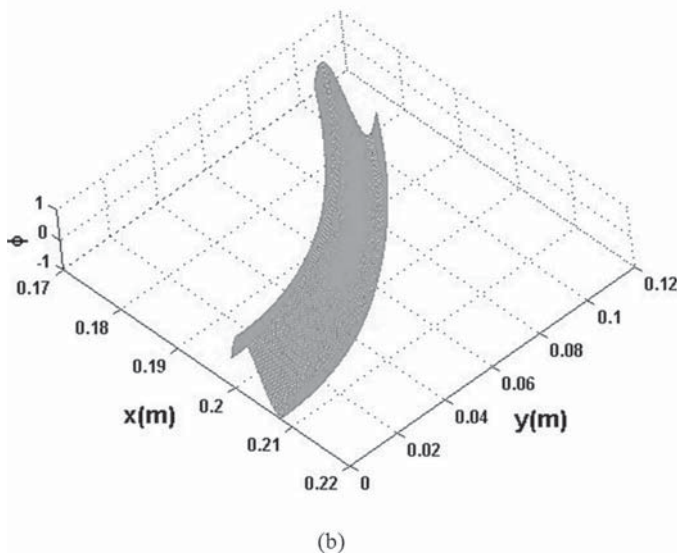
Fig. 2. Resonant frequencies.

(a)

(b)

Fig. 4. (a) Displacement and (b) electric potential for $m = 0$, $\omega = 1.55 \times 10^6$ Hz.

(a)

(b)

Fig. 3. (a) Displacement and (b) electric potential for $m = 0$, $\omega = 0.60 \times 10^6$ Hz.

Figs. 3–8 show displacement and electric potential distributions of the modes whose frequencies are near the origin of Fig. 2. Only symmetric modes with a $\cos\theta$ dependence are considered. Antisymmetric modes are of less interest because they are not electrically excitable by a radial electric field, which will be seen later in the forced-vibration analysis, and therefore are not plotted. Due to symmetry, only the fields in the first quadrant of Fig. 1 with $0 \le \theta \le \beta$ are plotted. The figures show that increasing m introduces more nodal points in the θ direction. For a fixed m, modes with more nodal points in the r direction have higher frequencies.

IV. FORCED VIBRATION

For forced vibration, we consider a time-harmonic voltage $2V$ applied across the electrodes at $r = a$, b with the electric potential as
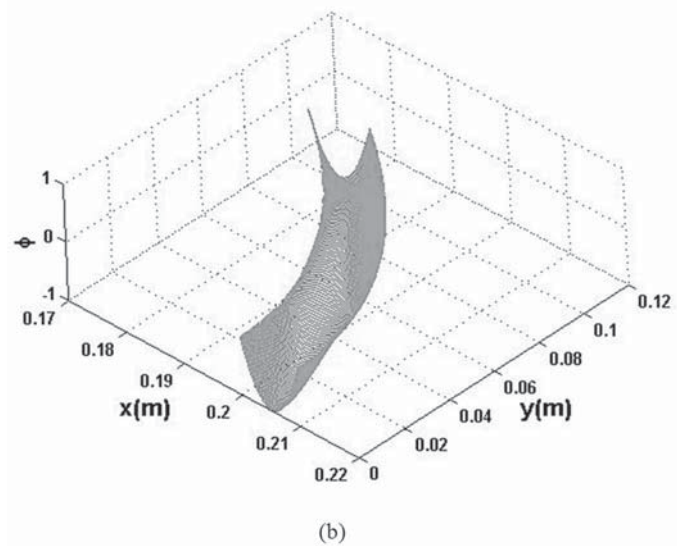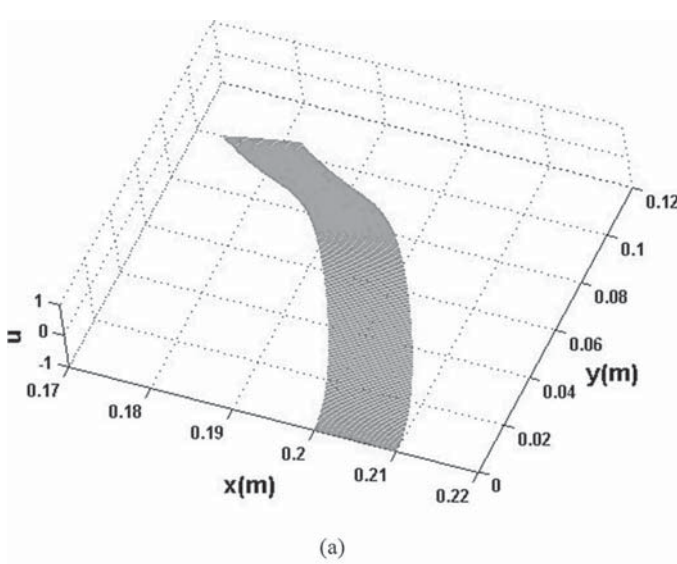
(a)

(b)
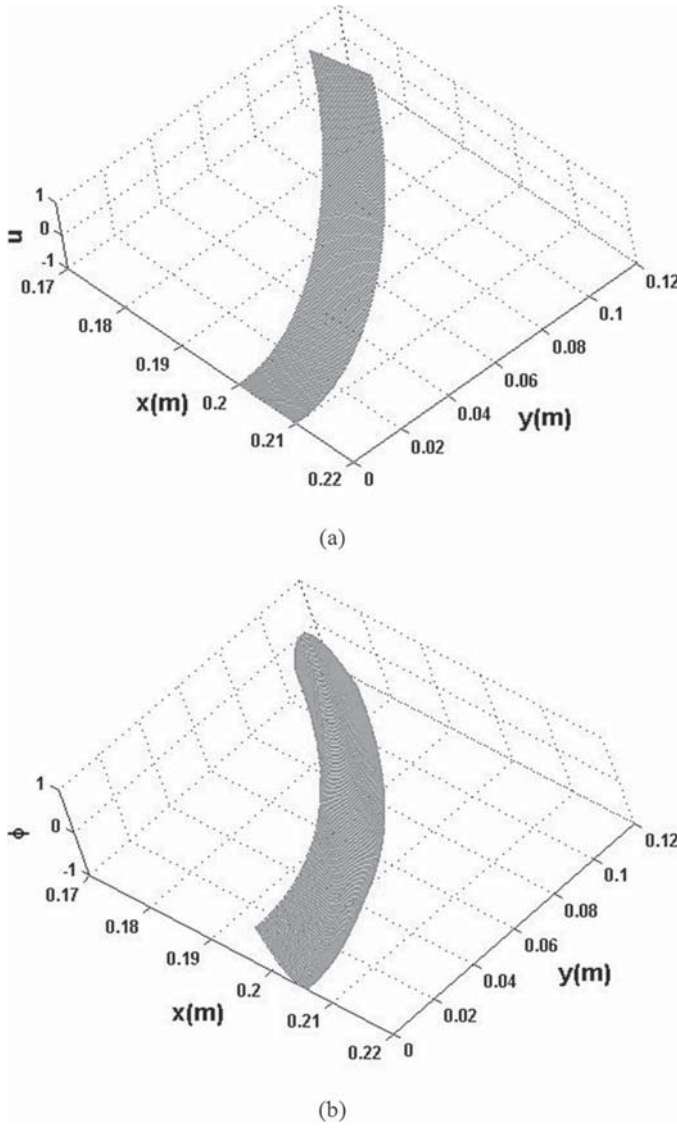
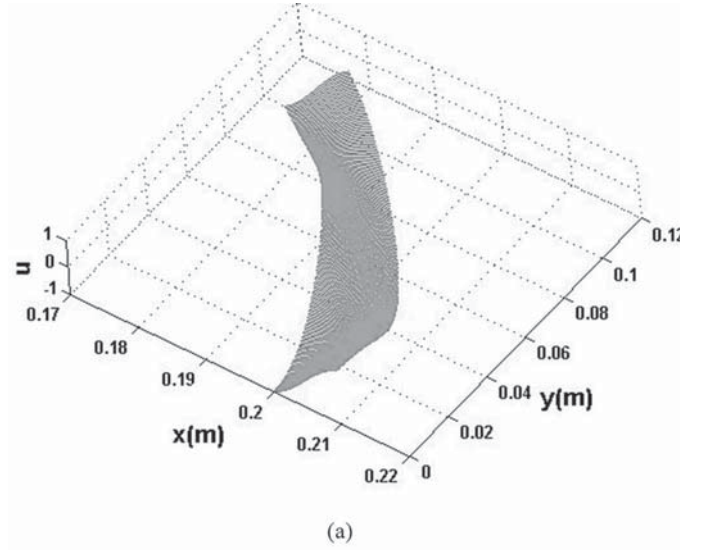Fig. 5. (a) Displacement and (b) electric potential for $m = 1$, $\omega = 0.05 \times 10^6$ Hz.

(a)

(b)

Fig. 6. (a) Displacement and (b) electric potential for $m = 1$, $\omega = 0.60 \times 10^6$ Hz.

$$\phi = \begin{cases} -V \exp(i\omega t), & r = a, \\ V \exp(i\omega t), & r = b. \end{cases} \tag{22}$$

Obviously only the symmetric modes can be excited. Therefore, a general symmetric solution satisfying the transducer edge conditions at $\theta = \pm\beta$ is constructed as

$$u = C_0 J_0(\xi r) + D_0 Y_0(\xi r)$$

$$+ \sum_{m=1}^{\infty} [C_m J_{\nu_m}(\xi r) + D_m Y_{\nu_m}(\xi r)] \cos \nu_m \theta,$$

$$\psi = F_0 \ln r + G_0 + \sum_{m=1}^{\infty} [F_m r^{\nu_m} + G_m r^{-\nu_m}] \cos \nu_m \theta. \tag{23}$$

The stress, electric displacement, and electric potential needed for boundary conditions are obtained as shown in (24) (see next page).

The boundary conditions at $r = a$, b require that the conditions in (25) (see page 2333) are met.

We multiply (25) by $\cos \nu_p \theta$ and integrate the resulting equation from $-\beta$ to β for $p = 0, 1, 2, 3, \ldots$. Then, from the orthogonality of $\cos \nu_p \theta$, the summation in (25) disappears. Only the θ-independent terms are left because the applied voltage is a constant and does not vary with θ. To calculate the charge on and the current flowing into the electrode at $r = b$, we need

$$D_r = e_{15} 2S_{rz} + \varepsilon_{11} E_r,$$

$$Q = \int_{-\beta}^{\beta} -D_r \big|_{r=b} b \, d\theta, \tag{26}$$

$$I = \dot{Q} = i\omega Q.$$

Then the impedance of the transducer is given by

$$Z = 2V/I. \tag{27}$$

$$\phi = \psi + \frac{e}{\varepsilon}u$$

$$= \frac{e}{\varepsilon}[C_0 J_0(\xi r) + D_0 Y_0(\xi r)] + F_0 \ln r + G_0 \tag{24a}$$

$$+ \sum_{m=1}^{\infty} \left[\frac{e}{\varepsilon} C_m J_{\nu_m}(\xi r) + \frac{e}{\varepsilon} D_m Y_{\nu_m}(\xi r) + F_m r^{\nu_m} + G_m r^{-\nu_m} \right] \cos \nu_m \theta,$$

$$T_{rz} = \overline{c}u_{,2} + e\psi_{,2}$$

$$= -\overline{c}\xi[C_0 J_1(\xi r) + D_0 Y_1(\xi r)] + e\frac{F_0}{r} \tag{24b}$$

$$+ \sum_{m=1}^{\infty} [\overline{c}\xi C_m J'_{\nu_m}(\xi r) + \overline{c}\xi D_m Y'_{\nu_m}(\xi r) + e\nu_m F_m r^{\nu_m - 1} - e\nu_m G_m r^{-\nu_m - 1}] \cos \nu_m \theta,$$

$$D_r = -\varepsilon\psi_{,r} = -\varepsilon\frac{F_0}{r} + \sum_{m=1}^{\infty} [-\varepsilon\nu_m F_m r^{\nu_m - 1} + \varepsilon\nu_m G_m r^{-\nu_m - 1}] \cos \nu_m \theta. \tag{24c}$$

(a)

(b)

Fig. 7. (a) Displacement and (b) electric potential for $m = 2$, $\omega = 0.11$ $\times 10^6$ Hz.

(a)

(b)
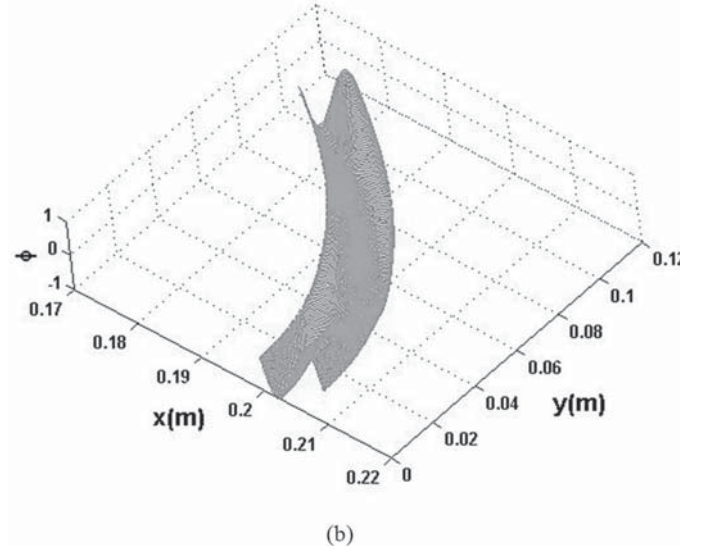
Fig. 8. (a) Displacement and (b) electric potential for $m = 2$, $\omega = 0.61$ $\times 10^6$ Hz.

$$\frac{e}{\varepsilon}[C_0 J_0(\xi a) + D_0 Y_0(\xi a)] + F_0 \ln a + G_0 + \sum_{m=1}^{\infty} \left[\frac{e}{\varepsilon} C_m J_{\nu_m}(\xi a) + \frac{e}{\varepsilon} D_m Y_{\nu_m}(\xi a) + F_m a^{\nu_m} + G_m a^{-\nu_m}\right]\cos\nu_m\theta = -V,$$

$$-\overline{c}\xi[C_0 J_1(\xi a) + D_0 Y_1(\xi a)] + e\frac{F_0}{a}$$

$$+ \sum_{m=1}^{\infty} \left[\overline{c}\xi C_m J'_{\nu_m}(\xi a) + \overline{c}\xi D_m Y'_{\nu_m}(\xi a) + e\nu_m F_m a^{\nu_m-1} - e\nu_m G_m a^{-\nu_m-1}\right]\cos\nu_m\theta = 0,$$

$$\frac{e}{\varepsilon}[C_0 J_0(\xi b) + D_0 Y_0(\xi b)] + F_0 \ln b + G_0 + \sum_{m=1}^{\infty} \left[\frac{e}{\varepsilon} C_m J_{\nu_m}(\xi b) + \frac{e}{\varepsilon} D_m Y_{\nu_m}(\xi b) + F_m b^{\nu_m} + G_m b^{-\nu_m}\right]\cos\nu_m\theta = V,$$

$$-\overline{c}\xi[C_0 J_1(\xi b) + D_0 Y_1(\xi b)] + e\frac{F_0}{b}$$

$$+ \sum_{m=1}^{\infty} \left[\overline{c}\xi C_m J'_{\nu_m}(\xi b) + \overline{c}\xi D_m Y'_{\nu_m}(\xi b) + e\nu_m F_m b^{\nu_m-1} - e\nu_m G_m b^{-\nu_m-1}\right]\cos\nu_m\theta = 0. \tag{25}$$
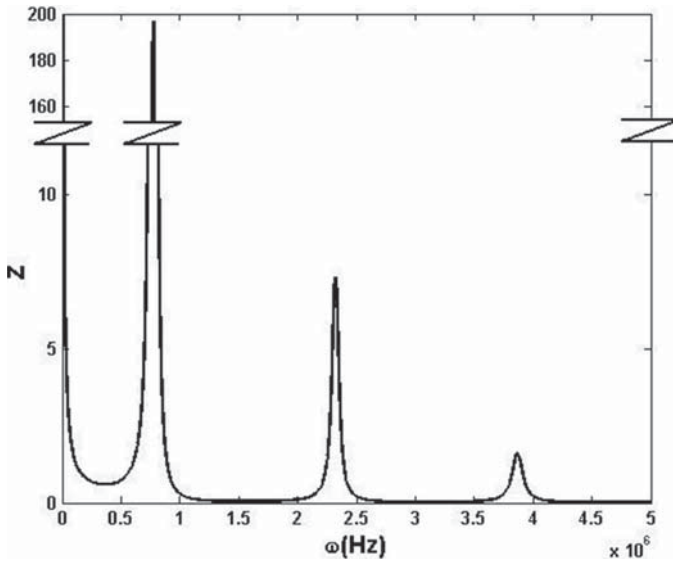
Fig. 9. Impedance versus driving frequency.

With (24c), the impedance can be written in the following form:

$$Z = \frac{2V}{i\omega \int_{-\beta}^{\beta} \varepsilon \frac{F_0}{b} b d\theta} = \frac{V}{i\omega\varepsilon F_0 \beta}. \tag{28}$$

In the numerical calculation for the forced vibration, the elastic constant c_{44} is replaced by $c_{44}(1 + iQ)$ to take viscous damping into consideration. For ceramics, Q is of the order of 10^{-3} to 10^{-2}. $Q = 0.05$ is used in the calculation.

Fig. 9 shows the real part of the impedance as a function of the driving frequency. Only the modes with $m = 0$ can be excited due to the uniformity of the applied voltage. Among the modes with $m = 0$, in the r direction, odd modes are mainly antisymmetric about the middle of
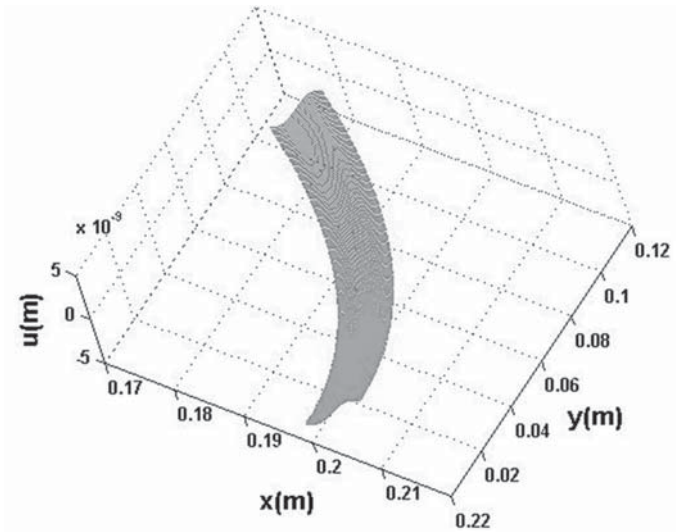
(a)
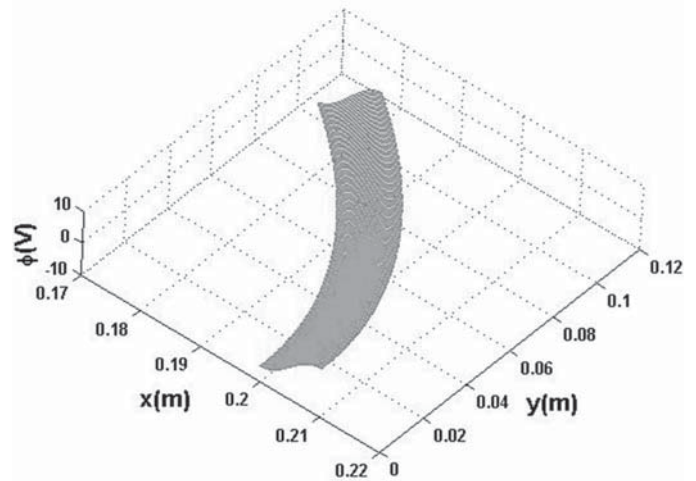
(b)

Fig. 10. (a) Displacement and (b) electric potential when $\omega = 0.774 \times 10^6$ Hz.

lem becomes much more complicated. Numerical procedures that may be needed are left for future work.
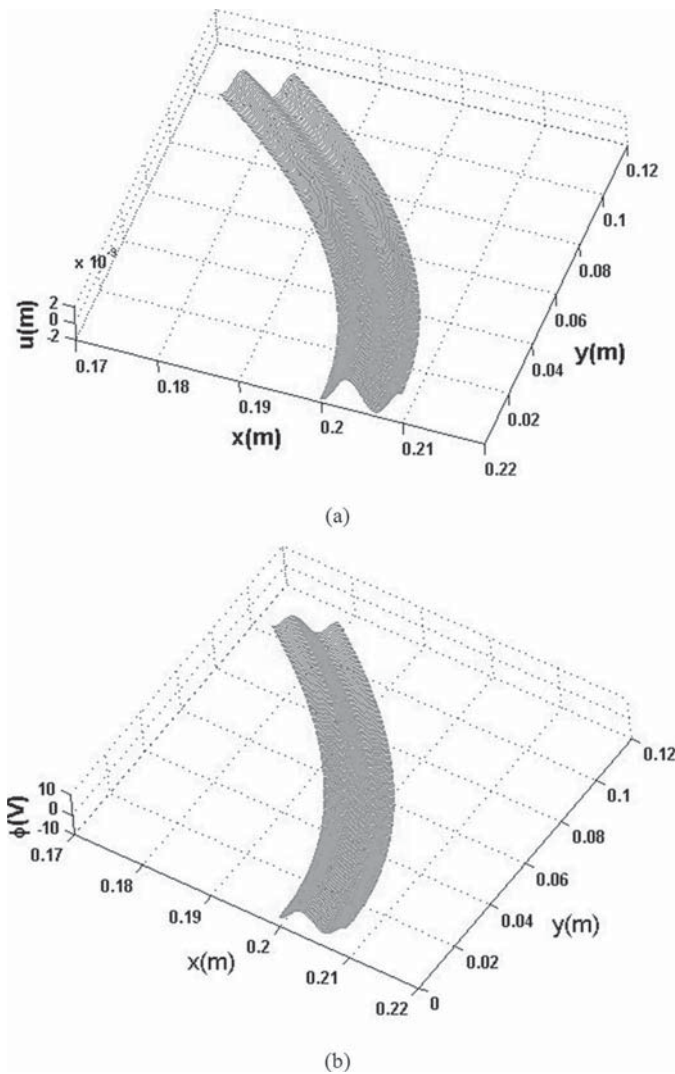
Fig. 11. (a) Displacement and (b) electric potential when $\omega = 2.32 \times 10^6$ Hz.

the transducer where $r = (a + b)/2$ and even modes are mainly symmetric. Therefore, the major peaks in Fig. 9 correspond to the first and the third resonant frequencies with $m = 0$ in Fig. 2.

Displacement and electric potential distributions at the first 2 major resonances in Fig. 9 are shown in Fig. 10 and 11. What is shown are the real parts of the complex fields. These are modes with $m = 0$. Modes with higher frequencies have more variations along r.

V. CONCLUSION

Exact solutions from the 3-D equations of linear piezoelectricity are obtained for free and electrically forced vibrations of a finite circular cylindrical panel piezoelectric transducer. The modes obtained include high-frequency modes of thickness-shear and thickness-twist. These cylindrical transducers can be used to excite SH modes and are useful for NDE of circular cylindrical structures. When they are attached to such structures, the modeling prob-

REFERENCES

[1] R. A. Langevin, "The electro-acoustic sensitivity of cylindrical ceramic tubes," *J. Acoust. Soc. Am.*, vol. 26, no. 3, pp. 421–427, 1954.
[2] H. S. Paul, "Vibrations of circular cylindrical shells of piezoelectric silver iodide crystals," *J. Acoust. Soc. Am.*, vol. 40, no. 5, pp. 1077–1080, 1966.
[3] L. O. Wilson and J. A. Morrison, "Wave propagation in piezoelectric rods of hexagonal crystal symmetry," *Q. Jl. Mech. Mech. Appl. Math*, vol. 30, no. 4, pp. 387–395, 1977.
[4] J. D. Dai, V. Winkel, J. E. B. Oliveira, and C. K. Jen, "Analysis of cladded acoustic fibers of hexagonal crystal symmetry," *IEEE Trans. Ultrason. Ferroelectr. Freq. Control*, vol. 39, no. 6, pp. 722–729, 1992.
[5] V. Winkel, J. E. B. Oliveira, J. D. Dai, and C. K. Jen, "Acoustic wave propagation in piezoelectric fiber of hexagonal crystal symmetry," *IEEE Trans. Ultrason. Ferroelectr. Freq. Control*, vol. 42, no. 5, pp. 949–955, 1995.
[6] M. Üçer and E. Akçakaya, "A new approach to the analysis of piezoelectric cladded acoustic fibers," *IEEE Trans. Ultrason. Ferroelectr. Freq. Control*, vol. 46, no. 5, pp. 1088–1093, 1999.
[7] P. Kielczynski, W. Pajewski, and M. Szalewski, "Determination of the shear impedance of viscoelastic liquids using cylindrical piezoceramic resonators," *IEEE Trans. Ultrason. Ferroelectr. Freq. Control*, vol. 50, no. 3, pp. 230–236, 2003.
[8] J. P. Wei and X. Y. Su, "Wave propagation in a piezoelectric rod of 6mm symmetry," *Int. J. Solids and Structures*, vol. 42, no. 13, pp. 3644–3654, 2005.
[9] S. N. Jiang, Q. Jiang, Y. T. Hu, X. F. Li, S. H. Guo, and J. S. Yang, "Analysis of a piezoelectric ceramic shell in thickness-shear vibration as a power harvester," *Int. J. Appl. Electromagn. Mechanics*, vol. 24, no. 1-2, pp. 25–31, 2006.
[10] J. S. Yang and R. C. Batra, "Thickness shear vibrations of a circular cylindrical piezoelectric shell," *J. Acoust. Soc. Am.*, vol. 97, no. 1, pp. 309–312, 1995.
[11] C. L. Chen, "On the electroacoustic waves guided by a cylindrical piezoelectric surface," *J. Appl. Phys.*, vol. 44, no. 9, pp. 3841–3847, 1973.
[12] N. T. Adelman and Y. Stavsky, "Radial vibrations of axially polarized piezoelectric ceramic cylinders," *J. Acoust. Soc. Am.*, vol. 57, no. 2, pp. 356–360, 1975.
[13] H. J. Ding, Y. M. Guo, Q. D. Yang, and W. Q. Chen, "Free vibration of piezoelectric cylindrical shells," *Acta Mechanica Solida Sinica*, vol. 10, no. 1, pp. 48–55, 1997.
[14] H. M. Wang, Y. M. Chen, and H. J. Ding, "Dynamic responses of a multilayered piezoelectric hollow cylinder under electric potential excitation," *J. Zhejiang Univ. Sci.*, vol. 69(A), no. 9, pp. 933–937, 2005.
[15] C. Q. Chen and Y. P. Shen, "Three-dimensional analysis for the free vibration of finite-length orthotropic piezoelectric circular cylindrical shells," *J. Vibrations Acoust.*, vol. 120, no. 1, pp. 194–198, 1998.
[16] H. J. Ding, R. Q. Xu, and W. Q. Chen, "Free vibration of transversely isotropic piezoelectric circular cylindrical panels," *Int. J. Mech. Sci.*, vol. 44, no. 1, pp. 191–206, 2002.
[17] H. S. Tzou, *Piezoelectric Shells*. Dordrecht, The Netherlands: Kluwer, 1993.
[18] J. S. Yang, *The Mechanics of Piezoelectric Structures*. Singapore: World Scientific, 2006.
[19] J. L. Bleustein, "A new surface wave in piezoelectric materials," *Appl. Phys. Lett.*, vol. 13, no. 12, pp. 412–413, 1968.
[20] J. L. Bleustein, "Some simple modes of wave propagation in an infinite piezoelectric plate," *J. Acoust. Soc. Am.*, vol. 45, no. 3, pp. 614–620, 1969.

[21] H. Jaffe and D. A. Berlincourt, "Piezoelectric transducer materials," *Proc. IEEE*, vol. 53, no. 10, pp. 1372–1386, 1965.

Zengtao Yang received his B.S. in civil engineering from Shenyang University, Shenyang, China, in 2004 and his M.S. in engineering mechanics from Jinan University, Guangzhou, China, in 2006. Currently he is a Ph.D. candidate in engineering mechanics at Central South University, Changsha, China. During 2007–2008 he is a visiting student at the Department of Engineering Mechanics of the University of Nebraska-Lincoln, Lincoln, NE. His research area is piezoelectric structures and devices.

Jiashi Yang received his B.E. and M.E. degrees in engineering mechanics in 1982 and 1985 from Tsinghua University, Beijing, China, and his Ph.D. degree in civil engineering in 1994 from Princeton University, Princeton, NJ. He was a Postdoctoral Fellow from 1993 through 1994 at the University of Missouri-Rolla, Rolla, MO, and from 1994 through 1995 at Rensselaer Polytechnic Institute, Troy, NY. He was employed by Motorola, Inc., Schaumburg, IL, from 1995 through 1997.

Since 1997 he has been an Assistant and Associate Professor at the Department of Engineering Mechanics of the University of Nebraska-Lincoln, Lincoln, NE. Dr. Yang has published over 170 journal papers on electromechanical materials and devices, and three books: *An Introduction to the Theory of Piezoelectricity*, *The Mechanics of Piezoelectric Structures*, and *Analysis of Piezoelectric Devices*.

Yuantai Hu received his B.S. degree in mining engineering in 1986 from Wuhan University of Science and Technology, Wuhan, China, and his M.S. and Ph.D. degrees in mechanics, respectively, from Harbin University of Technology, Harbin, China, in 1988 and from Shanghai Institute of Applied Mathematics and Mechanics, Shanghai University, Shanghai, China, in 1992.

From 1993 to 1997 he worked as a postdoctoral researcher at Shanghai Institute of Applied Mathematics and Mechanics and the Department of Mechanics of Huazhong University of Science and Technology, Wuhan, China, respectively. He served at the Department of Mechanics of Huazhong University of Science and Technology, Wuhan, China, as an associate professor and professor from 1997 to 2003. From April 2000 to May 2001 and from February 2004 to March 2005, he was a visiting scholar at the Department of Engineering Mechanics of the University of Nebraska-Lincoln and at the Department of Mechanical Engineering of University of California-Riverside. Now he is a professor in the Department of Mechanics, Huazhong University of Science and Technology, Wuhan, China.

His research area is piezoelectric structures and devices, ultrasonics and acoustics.
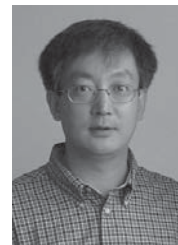
Qing-Ming Wang (M'00) is an assistant professor in the Department of Mechanical Engineering, the University of Pittsburgh, Pittsburgh, PA. He received the B.S. and M.S. degrees in Materials Science and Engineering from Tsinghua University, Beijing, China, in 1987 and 1989, respectively, and the Ph.D. degree in Materials from the Pennsylvania State University, University Park, PA, in 1998.

Prior to joining the University of Pittsburgh, Dr. Wang was an R&D engineer and materials scientist in Lexmark International, Inc., Lexington, KY, where he worked on piezoelectric and electrostatic microactuators for inkjet printhead development. From 1990 to 1992, he worked as a development engineer in a technology company in Beijing where he participated in the research and development of electronic materials and piezoelectric devices. From 1992 to 1994, he was a research assistant in the New Mexico Institute of Mining and Technology working on nickel-zinc ferrite and ferrite/polymer composites for EMI filter application. From 1994 to 1998, he was a graduate assistant in the Materials Research Laboratory of the Pennsylvania State University working toward his Ph.D. degree in the areas of piezoelectric ceramic actuators for low frequency active noise cancellation and vibration damping, and thin film materials for microactuator and microsensor applications.

Dr. Wang's primary research interests are in microelectromechanical systems (MEMS) and microfabrication; smart materials; and piezoelectric/electrostrictive ceramics, thin films, and composites for electromechanical transducer, actuator, and sensor applications.

He is a member of IEEE, IEEE-UFFC, the Materials Research Society (MRS), ASME, and the American Ceramic Society.

Property characterization of AlN thin films in composite resonator structure

Qingming Chen, Lifen Qin, and Qing-Ming Wang[a]

*Department of Mechanical Engineering and Materials Science, University of Pittsburgh,
Pittsburgh, Pennsylvania 15261*

AlN thin films with *c*-axis orientation have been investigated for fabricating thin film bulk acoustic wave resonators in the past few years. Characterization of thin film material properties including density, elastic modulus, and piezoelectric coefficient is essential in processing study and for predicting the performance of the acoustic devices. In this paper, we present our results on the fabrication of highly *c*-axis oriented AlN thin films on Pt/Ti/Si (100) substrates by dc reactive magnetron sputtering method. The crystalline structure and the surface morphology of AlN films are characterized by x-ray diffraction and scanning electron microscopy. The effective piezoelectric coefficient $d_{33\text{eff}}$ of the AlN films was measured by a laser interferometer method and the piezoelectric coefficient d_{33} was estimated. A recently developed resonance spectrum method is applied to characterize the electromechanical properties of AlN thin films based on the input electrical impedance equation derived by one-dimensional transmission line theory for composite resonators. Using the experimental impedance spectrum data, the density and elastic constant of the piezoelectric AlN thin film in the four-layer composite resonator structure are evaluated. The calculated results reveal that the piezoelectric coefficient d_{33}, density, and velocity of the *c*-axis oriented AlN thin film are 4.19 pm/V, 3187.3 kg/m^3, and 10631 m/s, respectively. © *2007 American Institute of Physics*. [DOI: 10.1063/1.2716391]

I. INTRODUCTION

With a significant progress in thin film deposition technologies for complex material systems such as AlN, ZnO, and PZT in recent years, thin film bulk acoustic wave resonator (FBAR) and filter concepts are becoming more and more attractive for microwave frequency control applications. For resonators operating in the gigahertz range, a thin film piezoelectric layer in the order of a few microns with desirable electromechanical properties is required. Among these materials, AlN is particularly attractive due to that it has a number of interesting properties such as high thermal conductivity, high electrical insulation, and chemical stability.[1] In addition, it is piezoelectric in its crystalline form and has high longitudinal acoustic velocity, ∼11 000 m/s. These characteristics make it possible to design and fabricate high frequency resonators and bandpass filters for signal processing and communication devices. It is obvious that the deposition of high quality AlN thin film with desirable material properties is needed for the fabrication of thin film bulk acoustic wave resonators and bandpass filters.

In this paper, we report our recent studies on the deposition of highly *c*-axis oriented AlN thin films on both sapphire and silicon substrates by dc reactive magnetron sputtering and the characterization of material elastic and piezoelectric properties. A single beam laser interferometer system that can detect very small displacement signals with resolution down to 10^{-3} Å in the low frequency range was first employed to measure the effective piezoelectric coefficient of the AlN thin film through converse piezoelectric

effect,[2] and a resonant spectrum method was applied to extract the other properties including density, elastic constant, and acoustic wave velocity of the AlN films based on the input electric impedance of thin film composite resonators.

Many approaches have been used to derive the input electric impedance of a thin film composite resonator. These include the equivalent circuit method[3] and transfer matrix approach. Sittig[4] and Meitzler and Sittig[5] used the transfer matrix approach to calculate the impedance of the multilayer piezoelectric transducers used in ultrasonic digital delay lines. Zhang *et al.* utilized the input electric impedance spectrum for a four-layer composite resonator to characterize the material properties of ZnO thin film on the quartz substrate.[6] Here, we follow a similar approach by applying the resonance spectrum method to characterize the material properties of the AlN thin film in a composite resonator.

II. METHODS FOR PROPERTY CHARACTERIZATION

A. Measurement of effective piezoelectric coefficient $d_{33\text{eff}}$ of AlN thin film

In order to measure the piezoelectric coefficient of the AlN thin film, both the direct and converse piezoelectric effects can be employed.[2,7–9] It is in general more convenient to use the converse piezoelectric effect to characterize the piezoelectric coefficient of thin film or bulk materials by measuring the displacement of the surface of the materials subjected to the external ac electric field or voltage. Since the thin film AlN is deposited on the substrate, which can be regarded as a thin layer clamped on the substrate, the strain and electric field ratio $d_{33\text{eff}} = x_3/E_3 = \Delta d/V$ where Δd is the displacement induced by applied voltage V, does not represent the real piezoelectric coefficient d_{33} of the thin film in

---

[a] Author to whom correspondence should be addressed; electronic mail: qmwang@engr.pitt.edu

free mechanical boundary conditions but an effective value. The piezoelectric coefficient of AlN is relatively small, the resulting deformation excited by the electric field is correspondingly very small. Thus how to measure the small deformation signal of the AlN accurately is important for the measurement of the d_{33eff}. For the characterization of the piezoelectric property of AlN film, a very sensitive single beam laser interferometer system with displacement resolution down to 10^{-3} Å in the low frequency range was employed in the measurement.[2]

B. Resonance spectrum method

In the past decades, several methods have been developed to determine the coefficients of piezoelectric materials in order to better characterize and describe the electromechanical properties and performance of materials and devices. The measurement methods for low loss materials have been summarized in IEEE standards.[10] Those methods have been successfully used to determine the coefficients of materials with high mechanical quality factors such as lead titanate zirconate ceramics.[11,12] In order to characterize the material properties of the piezoelectric composite resonators, the resonance spectrum method has also been developed,[4–6] which includes the effect of electrodes and substrate. Using the information contained in the impedance or admittance spectrum for piezoelectric resonators such as parallel and series resonance frequencies, the elastic and electromechanical properties of the piezoelectric thin film layer can be obtained. The resonance spectrum method is particularly suitable for the characterization of material properties of piezoelectric thin films that are used for microdevice applications. We have also applied the transfer matrix approach to derive the one-dimensional input electric impedance for three-layer and four-layer thin film composite resonators and the input electric impedance has been used for the discussion of the effect of electrodes and the temperature compensation in composite resonators.[6,13,14] The input electric impedance of the four-layer resonator is

$$Z_{in} = \frac{V}{I} = \frac{1}{j\omega C_0}\left[1 - \frac{k_t^2}{\gamma}\frac{(z_1 + z_2)\sin\gamma + j2(1 - \cos\gamma)}{(z_1 + z_2)\cos\gamma + j(1 + z_1 z_2)\sin\gamma}\right],$$
(1)

where $z_1 = Z_1/Z_0$ and $z_2 = Z_2/Z_0$ are the normalized acoustic loading impedances on both sides of the piezoelectric layer. $C_0 = \varepsilon_{33}^S S/t$ is the clamped capacitor of the resonator with area S and dielectric permittivity ε_{33}^S. $Z_0 = S\rho v$ is the acoustic impedance of the piezoelectric layer with density ρ, v is the longitudinal acoustic wave velocity in the piezoelectric layer along the direction normal to the resonator surface, $\gamma = \omega t/v$ is the phase delay of the acoustic wave in the piezoelectric film in which $\omega = 2\pi f$. It is noted that a three-layer thin film resonator is a special case of four-layer resonators with zero substrate thickness. Using Eq. (1), the electric impedance spectrum of the thin film composite resonator can be simulated by using appropriate material property data.

It is known that parallel resonances correspond to maximums of the resistance of the composite resonator. In a lossless resonator, parallel resonance corresponds to the infinite

impedance Z_{in}. Thus, by setting the denominator equal to zero, we can get the determination equation for parallel resonance frequencies:[6]

$$(z_1 + z_2)\cos\gamma + j(1 + z_1 z_2)\sin\gamma = 0.$$
(2)

At the center of the first normal region, where $\gamma \approx \pi$, we can get the space between two adjacent parallel resonant frequencies which can be derived from Eq. (2):

$$\Delta f_N = \Delta f_0\left(1 + \frac{\rho_{e1}t_{e1} + \rho_{e2}t_{e2} + \rho t}{\rho_{sb}t_{sb}}\right)^{-1},$$
(3)

where $\Delta f_0 = v_{sb}/(2t_{sb})$, and the subscripts $e1$, $e2$, and sb represent the top electrode, bottom electrode, and substrate. Similarly, at the center of the first transition region, where $\gamma \approx \pi/2$, we can get the space between two adjacent parallel resonant frequencies:[6]

$$\Delta f_T = \Delta f_0\left(1 + \frac{\rho_{sb}v_{sb}^2 t}{\rho v^2 t_{sb}} + \frac{\rho_{sb}v_{sb}^2 t_{e2}}{\rho_{e2}v_{e2}^2 t_{sb}} + \frac{\rho_{sb}\rho_{e1}v_{sb}^2 t_{e1}}{\rho^2 v^2 t_{sb}}\right)^{-1}.$$
(4)

The density and the acoustic velocity of the AlN thin film can be calculated from Eqs. (3) and (4). The value of the stiffened elastic constant of the film can then be calculated by

$$c^D = v^2\rho.$$
(5)

C. Nanomechanical property characterization by nanoindentation

Indentation has been widely used to measure the mechanical properties of thin film materials and a host of nanoindentation methods is available, which employ various tip shapes and rely on different model assumptions.[15–18] The two mechanical properties measured most frequently using indentation techniques are the hardness H and the elastic modulus E. As the indenter is pressed into the sample, both elastic and plastic deformation occurs, which results in the formation of a hardness impression conforming to the shape of the indenter. During indenter withdrawal, only the elastic portion of the displacement is recovered, which facilitates the use of an elastic solution in modeling the contact process. Thus in a typical nanoindentation test, data from a complete loading and unloading cycle are collected to generate a force-distance curve, which is then used for the estimation of nanomechanical properties. Nanoindentation hardness is defined as the indentation load divided by the projected contact area of the indentation. It is the mean pressure that a material can support under load. From the load-displacement curve, hardness can be obtained at the peak load, $H = P_{max}/A$, where A is the projected contact area. The elastic modulus of the indented sample can be obtained from the initial slope of the unloading curve, $S = dP/dh$. A geometry-independent relation has been derived for contact stiffness, contact area, and elastic modulus as follows:[19–21]

$$S = 2\beta\sqrt{\frac{A}{\pi}}E_r,$$
(6)

where β is a constant that depends on the geometry of the indenter ($\beta = 1.034$ for a Berkovich indenter) and E_r is the

TABLE I. Sputtering parameters for AlN thin films.

Target (99.999% purity)	ϕ50 mm aluminum
dc power (W)	200–275
Substrate temperature (°C)	450–550
Target-substrate distance (mm)	40
Base pressure (torr)	$<10^{-6}$
Sputtering pressure (mtorr)	2–4
Ar gas flow rate (SCCM)	5–10
N_2 gas flow rate (SCCM)	12–20

FIG. 1. (Color online) The schematic four-layer structure of the thin film composite resonator.

reduced elastic modulus, which accounts for the fact that elastic deformation occurs in both the sample and the indenter. E_r is given by

$$E_r = \frac{1-\nu_f^2}{E_f} + \frac{1-\nu_i^2}{E_i}, \qquad (7)$$

where E_f and E_i are the elastic modulus of the thin film sample and the indenter, and ν_f and ν_i are the Poisson ratios of the film and the indenter, respectively. For diamond, E_i =1141 GPa and ν_i=0.07.

In this study, fixed probe nanoindentation method was employed to characterize the nanomechanical properties of the AlN thin films. The load-displacement curves were obtained at different load conditions, and the hardness and the elastic modulus of the thin films can be mapped at different locations of the films. Comparing with other indentation methods that use cantilever indenters, fixed probe nanoindentation has a few advantages. First, since there is a tilting angle for cantilever indenter, the indentation made by the indenter is usually not totally perpendicular to the sample surface. However, the probe for the fixed probe nanoindenter is normal to the sample surface. Second, the maximum load for a fixed nanoindenter can be up to 10 mN, which is much larger than the cantilever indenter's maximum load, which is normally below 100 μN. It should be pointed that in the determination of elastic modulus and hardness of supported thin films, complicated substrate influences may be introduced due to finite sample thickness and/or the presence of multiple layers.[22–24] To avoid this complication, it is usually required that the indentation depth is less than one-tenth of the film thickness.

III. EXPERIMENTAL PROCEDURES

A. Deposition of the AlN thin film

The AlN thin films were deposited by using dc reactive magnetron method (ATC-1300 dc and rf magnetron sputtering systems, AJA International, MA) from an Al target of high purity (99.999%) in the high purity nitrogen (99.999%) and argon (99.999%) gas mixture. Before the sputtering, the silicon (100) and sapphire (0001) substrates were cleaned.

The (100) direction of silicon is the more common wafer orientation for microelectromechanical devices. Unfortunately, the c-axis orientation growth of the AlN film on the silicon substrate with this direction is very difficult. There are also a large lattice mismatch and a large difference in the coefficient of thermal expansion between the AlN film and the Si (100) substrate. The Pt (111) is an ideal buffer layer
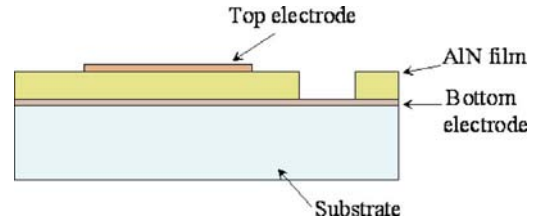
for the c-axis oriented AlN film growth where the AlN crystal grains grow quasiepitaxial on Pt (111) substrate.[25,26] Thus, before sputtering the AlN (002), the bottom electrode Pt/Ti was grown first on the substrate. Here, Ti thin film was used as the adhesive layer between Pt thin film and Si substrate. The Ti thin film should have an adequate thickness to bond the Pt and Si together but not affect the electromechanical properties of the resonator. Table I lists the processing parameters used in the deposition process for AlN film. The deposition time of the AlN thin film varied from 3 to 6 h.

B. Fabrication of the four-layer composite resonator

After the deposition of the piezoelectric AlN layer, hot H_3PO_4 acid is used to etch the AlN film to expose the bottom electrode. Then the top electrode Al was deposited and patterned to form the four-layer composite resonator (Fig. 1).

The AlN thin film composite resonator on sapphire substrate was used to characterize the effective piezoelectric coefficient d_{33eff} of AlN film, and that with thin silicon substrate (100 μm) was utilized to characterize the density and stiffened elastic modulus and acoustic wave velocity of the AlN thin film by the resonance spectrum method.

C. Measurement of effective piezoelectric coefficient d_{33eff}

The setup for the single beam laser interferometer is shown in Fig. 2. The laser beam from the He–Ne laser-light source is split into two equal components by the beam splitter. One of the beams is incident on the reference mirror and the other on the sample to be tested where both lasers travel
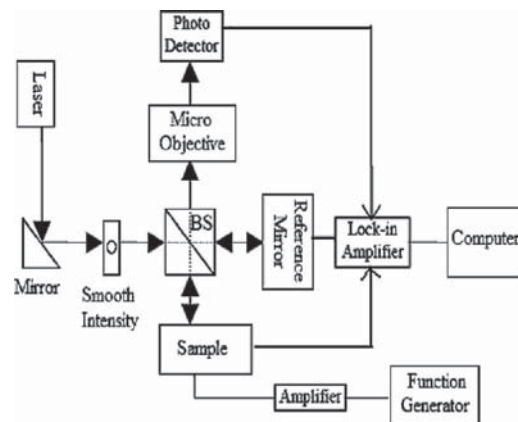

FIG. 2. Experimental setup of laser interferometer for the measurement of piezoelectric coefficient.

paths of equal length. There is a reflected beam from each surface and the beams are then combined in the beam splitter and the intensity is gathered at the photodetector. The absolute phase of each beam in turn depends on the distance between the beam splitter and the respective reflecting surface. If the surface of the test sample moves due to the external voltage applied, the absolute phase of the combined probe beam will change. By detecting the electric signal variation induced by the phase change, the displacement of the sample surface can be obtained. To eliminate possible electric and mechanical noise at the measurement frequency (1 or 10 Hz), a lock-in amplifier was used to detect the signal at the measurement frequency; thus measurement sensitivity can be improved.

D. Measurement of the scattering parameters S_{11}

When an electric device operates at the low frequency range, the dimensions of the elements in the circuit are much smaller than the wavelength and thus the circuit can be treated as the interconnection of lumped elements. The voltage and current are unique at any point in the circuit. Therefore, we can use electric impedance and admittance parameters to describe the circuit network. However, when the operating frequency is up to the radio frequency (rf) or microwave wave range, the dimensions of the elements are larger than the wavelength. The impedance and admittance are not well defined in such situation. Normalized wave variables (a and b) are more suitable for the characterization of the circuit at microwave or higher frequencies. The scattering parameters or S parameters are used to express the relationship of the normalized wave variables. Unlike other parameters, the S parameters relate to the traveling waves that are scattered or reflected when a network is inserted into a transmission line with certain characteristic impedance Z_0. For a two-port network, there are totally four scattering parameters S_{ij} ($i, j = 1, 2$). Each S parameter has two subscripts, i and j, where i refers to the port number at which power emerges and j refers to the port number at which power enters. Thus S_{11} and S_{22} are the reflection coefficients and S_{12} and S_{21} are the transmission coefficients. Specifically, reflection scattering parameter S_{11} is defined as

$$S_{11}^2 = \frac{\text{power reflected from the network input}}{\text{power incident on the network input}}. \tag{8}$$

It reflects the impedance Z_{in} and admittance Y_{in} of the resonator through the following equations:

$$Z_{in} = Z_0 \frac{1 + S_{11}}{1 - S_{11}}, \tag{9}$$

$$Y_{in} = \frac{1}{Z_0} \frac{1 - S_{11}}{1 + S_{11}}, \tag{10}$$

where $Z_0 = 50 \ \Omega$ is the standard normalized impedance for the network analyzer. Measurement of the S parameter is usually performed using a vector network analyzer (VNA). In the measurement of the S parameter, a careful calibration of the VNA is very important to get accurate results for the devices under test. VNA calibration is the process of mea-
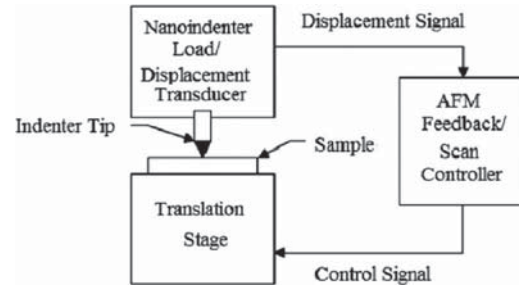

FIG. 3. Schematic of a fixed probe nanoindenter with *in situ* imaging capability.

suring devices with known characteristics and using these measurements to establish the measurement reference planes. Calibration also corrects for the imperfections of the measurement system. These imperfections include not only the nonideal nature of cables and probes but also the internal characteristics of the VNA itself. A VNA uses multiple standards, typically open circuit, short circuit, loads, and through connections, to perform the calibration.

The S_{11} of AlN thin film composite resonator was measured by an Agilent network analyzer (Agilent 8510C vector network analyzer, 45 MHz to 50 GHz, Agilent Technologies, Palo Alto, CA). Calibrations were first performed using open, short, and standard (50 Ω). In the measurement, the four-layer thin film composite resonator was placed on the probe station (Summit 9101 manual probe station, Cascade MicroTech, OR), which contacted the sample bottom surface only at the edge so that the resonator could vibrate with free boundary condition in the thickness direction. A proper SG probe, which has two pins on the tip, was used to contact the electrodes of the composite resonator electrically. The other end of the probe was connected to the network analyzer through a cable.

The reflection scattering parameter S_{11} was measured from 400 to 2500 MHz. The entire frequency span of 2100 MHz was divided into tens of narrow subspans to achieve higher resolution in the resonance spectrum measurement.

E. Nanomechanical test of AlN thin films

The nanoindentation tests were performed in a Hysitron TriboScope (Minneapolis, MN) attached to a Quesant (Agoura Hills, CA) atomic force microscope (AFM). Figure 3 is a schematic of the working principle for the Hysitron nanoindenter. *In situ* imaging capability allows the indenter probe to be positioned to any desired material feature within 10 nm. A Berkovich diamond indenter with a nominal tip radius of 40 nm is used. AlN films with thicknesses of 0.6, 1.2, and 1.5 μm deposited on sapphire substrate were used for this study. The maximum loads are varied from 500 to 4000 μN. The results of the loads and displacements during the test offer us a lot of information including the reduced elastic modulus and hardness.
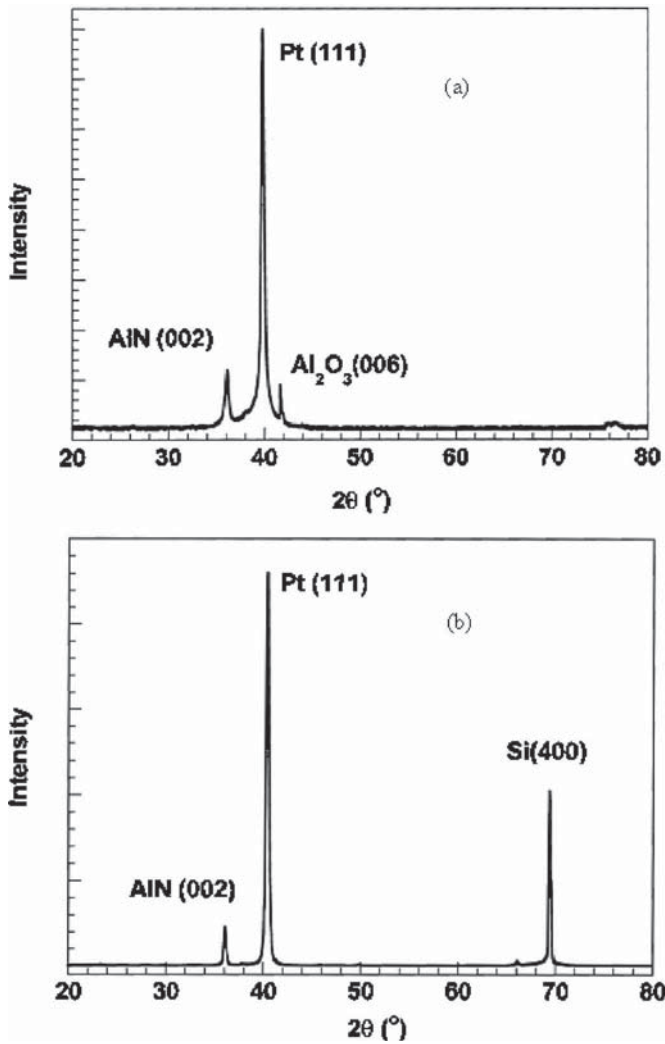
FIG. 4. X-ray diffraction patterns of AlN films deposited at 550 °C on different substrates: (a) sapphire (0001) and (b) silicon (100).

IV. RESULTS AND DISCUSSIONS

A. Surface morphology and crystal structure of AlN film

After the deposition of the bottom electrode and AlN thin films, the thin film crystalline structures were characterized by x-ray diffraction (XRD) and scanning electron microscopy (SEM). Figure 4 shows the XRD patterns of the AlN thin films deposited on different substrates with Pt/Ti bottom electrode layers. Only AlN (002) and Pt (111) peaks are observed, indicating that highly c-axis oriented AlN films have been achieved. Figures 5(a) and 5(b) show the SEM images of the cross section of the AlN thin films deposited on the sapphire (0001) and silicon (100) substrates, respectively. The SEM images reveal that the AlN films have dense column grains that are perpendicular to the surface of the substrates. Figure 6 shows the surface morphology of the AlN thin film on silicon substrate. The results indicate that under the processing conditions, AlN thin films deposited are smooth, crack-free, and with a good uniformity.

B. Piezoelectric coefficient d_{33} of AlN film

With quasistatic driving voltage at 1 Hz and peak to peak voltage from 0 to 5 V, the voltage induced dynamic
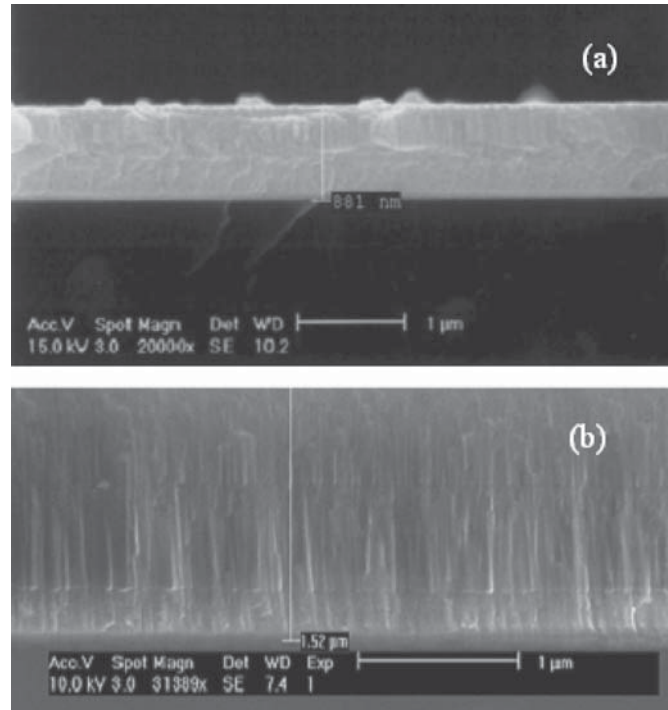

FIG. 5. SEM micrographs of AlN films deposited at 550 °C on (a) sapphire (0001) substrate and (b) silicon (100) substrate.

displacement of the piezoelectric AlN thin film was measured using the single beam laser interferometer. An effective piezoelectric strain coefficient of $d_{33\text{eff}}=2.9$ pm/V was detected for AlN film in the multilayer composite resonator structure (electrode/AlN thin film/electrode/sapphire). Since the piezoelectric coefficient is measured under the fact that the AlN film is always clamped to the sapphire substrate, the displacement and driving voltage ratio $\Delta d/V$ does not reflect the true piezoelectric coefficient d_{33} of the AlN film under free boundary condition. In the converse piezoelectric effect, the effective piezoelectric coefficient $d_{33\text{eff}}$ of thin film materials can be related to the true piezoelectric coefficient by the following relationship[27]

$$d_{33\text{eff}} = d_{33} - 2d_{31}s_{13}^E/(s_{11}^E + s_{12}^E), \tag{11}$$

where s_{11}, s_{12}, and s_{13} are the mechanical compliances of the piezoelectric film and d_{31} is the transverse piezoelectric coefficient. Since $d_{33} \approx -2d_{31}$, we have
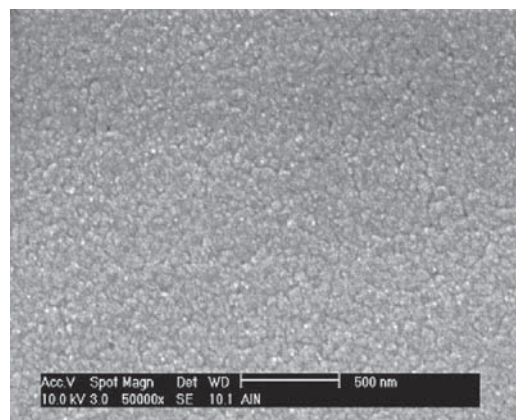

FIG. 6. Surface morphology of the AlN thin film on silicon substrate.

TABLE II. Properties of electrode and substrate materials used in the calculation.

Electrode	Density (kg/m^3)	Acoustic velocity (m/s)	Mechanical Q
Al	2 700	6418	2000
Pt	21 450	2823	500
Si	2 320	8270	3000

$$d_{33} = d_{33\text{eff}}(s_{11}^E + s_{12}^E)/(s_{11}^E + s_{12}^E + s_{13}^E). \qquad (12)$$

Substituting the values of s_{11}, s_{12}, and s_{13} into Eq. (12), the true piezoelectric coefficient $d_{33}=4.17$ pm/V can be calculated, which is in fairly good agreement with the reported values in literatures.[28–31]

C. Density and acoustic velocity of AlN film

Based on the one-dimensional input electric impedance [Eq. (1)], the electric impedance spectra for a four-layer thin film composite resonator and a three-layer resonator can be simulated. Listed in Tables II and III are the material properties used in the calculation. Figures 7(a) and 7(b) show the typical simulation results of the electric impedance spectra for composite resonators, in which material properties of each layer are plugged in the equation for calculation. It should be mentioned that a small imaginary part of the acoustic velocity for each material has been introduced in the calculation, which can stand for the mechanical quality factor of the material. The mechanical quality factor Q in the table represents half of the real part to imaginary part ratio of the acoustic velocity.[13,14] The impedance of the composite resonator follows a hyperbolic decrease that is the presentation of the static capacitance C_0 of the piezoelectric layer. There are multiple sharp peaks corresponding to the resonance "modes." At a resonance mode, a standing wave is established in the thickness direction of the composite resonator. Since the substrate is much thicker than the piezoelectric layer, the mode frequencies are mainly determined by the substrate and modulated by the piezoelectric layer. Therefore, both the piezoelectric layer and the substrate will affect the distribution of multiple resonance modes of the resonator. By analyzing the space of the adjacent resonance frequency at special regions, for instance, the first normal and transition regions, we can derive the material properties of the piezoelectric layer.

The experimental results for the S_{11} parameter and the converted impedance spectrum with three consecutive peaks for a four-layer composite resonator are shown in Figs. 8(a) and 8(b). By measuring the parallel resonance frequency of these modes, we can obtain the space of two adjacent parallel resonance frequencies Δf_P over the measurement frequency
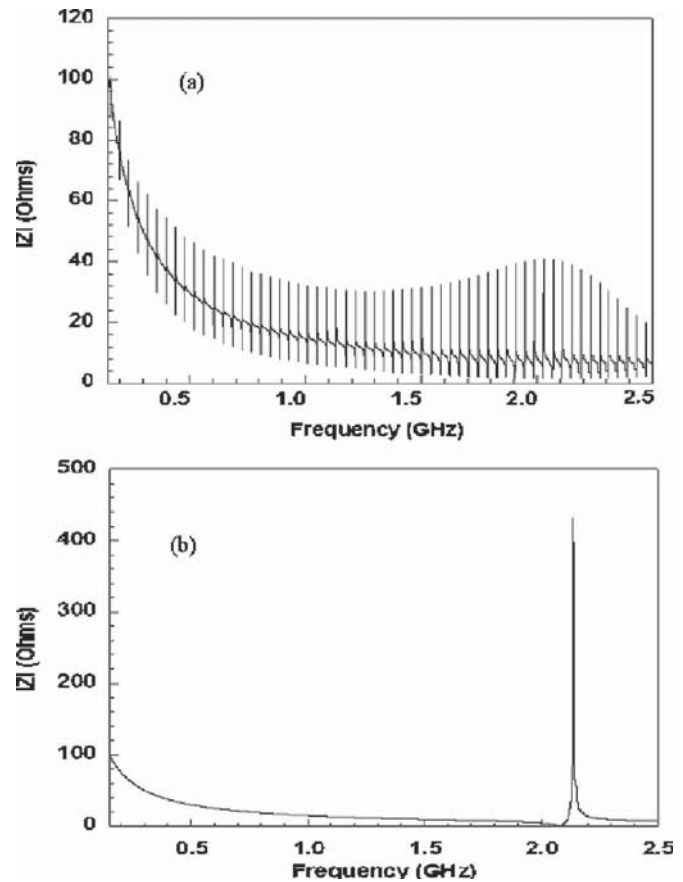

FIG. 7. Simulated electric impedance spectra of (a) a four-layer AlN thin film composite resonator and (b) a three-layer AlN thin film composite resonator.

range. Figure 9 shows the experiment results and the simulation results of Δf_P. Although the experimental data are a little dispersive, the periodic shape of the curve is in good agreement with the simulation results. By averaging the measurement data around the center of the first normal and transition regions, we can obtain values of Δf_T and Δf_N of 40.81 and 39.86 MHz, respectively.

Using Eqs. (3) and (4), the density and acoustic velocity of the thin film are attained as 3187.3 kg/m^3 and 10631 m/s. From Eq. (5), the stiffened elastic constant of the AlN thin film is 341.2 GPa.

D. Elastic modulus and hardness of the *c*-axis oriented AlN film

Using the nanoindentation, the load-displacement curves were obtained. Figure 10 shows the nanoindentation load-displacement curves for the AlN thin films with thicknesses of 0.6 and 1.5 μm that are deposited on sapphire substrates. Maximum loads P_{max} for the indentation are varied from

TABLE III. Properties of the piezoelectric thin film used in the simulation in the calculation.

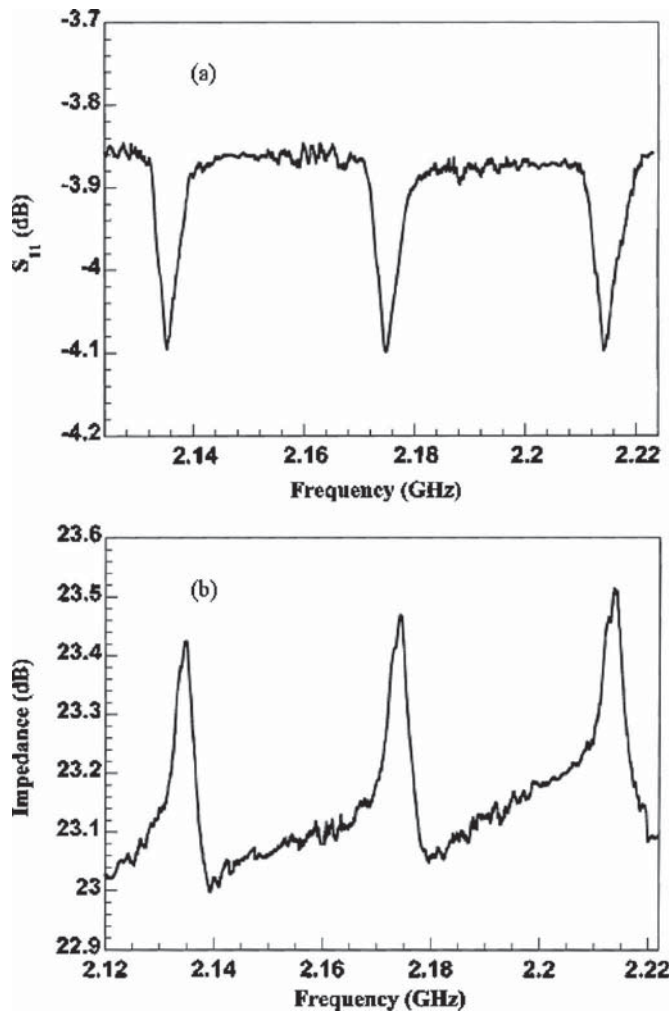| Piezoelectric film	Density (kg/m^3)	Acoustic velocity (m/s)	k_t^2 (%)	Thickness (μm)	Area (m^2)	Q	ε_r
AlN	3300	11 000	6.25	1.9	2.5×10^{-9}	500	8.5

FIG. 8. (a) Scattering parameter S_{11} measured by the network analyzer and (b) impedance spectrum for a four-layer AlN composite resonator.
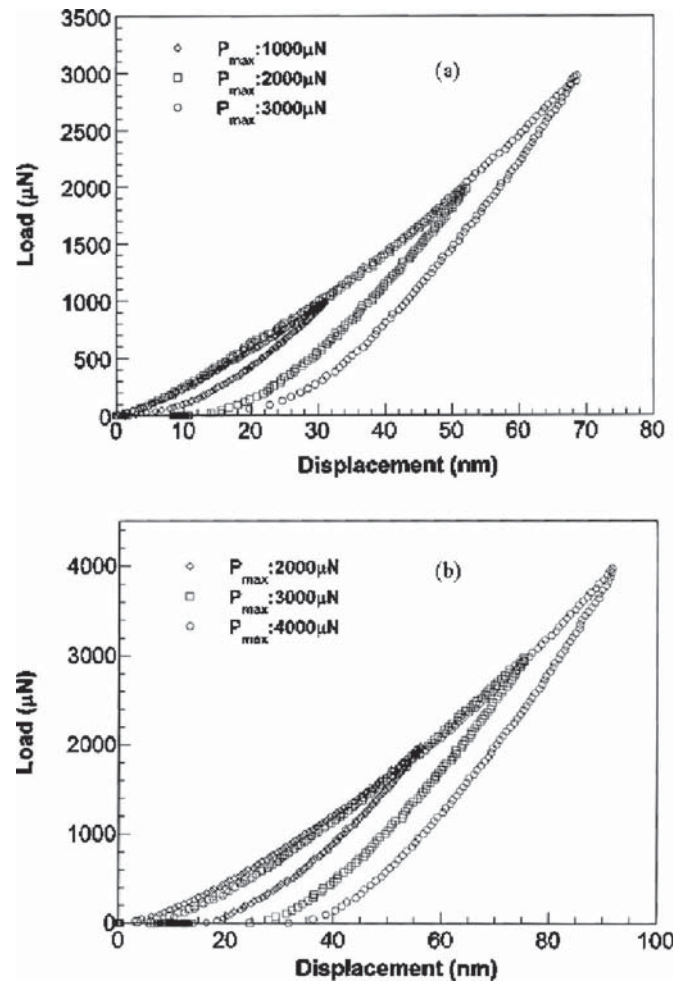

FIG. 10. Nanoindentation load-displacement curves on AlN thin films with different thicknesses and under different load conditions: (a) thickness of the AlN thin film $t_f=0.6$ μm; (b) thickness of the AlN thin film $t_f=1.5$ μm.

500 to 4000 μN during the tests. All the load-displacement curves are smooth and regular without discontinuities, which indicate that no cracking occurred in the penetration process. From the load-displacement curves for various applied maximum loads, the reduced elastic modulus E_r and hardness H can be obtained.

Figures 11(a) and 11(b) show the reduced elastic modulus E_r and hardness of AlN thin films with different thick-

FIG. 9. (Color online) Space of the parallel resonance frequency as a function of parallel resonance frequency.

nesses under different maximum loads at room temperature. No significant difference is observed for values of the elastic modulus and hardness of AlN thin films with different thicknesses. For all samples under test, the thickness of AlN film is quite thick as compared with the indentation depth; the effect of the substrate is thus insignificant. The variation of the properties could be due to the surface conditions such as roughness at different indentation locations on the films. In addition, indentation at or close to the grain boundaries may lead to lower values of elastic modulus and hardness as can be expected. The average reduced modulus of all thin film samples is about 250 GPa and the average hardness of the thin films is about 18 GPa.

The elastic modulus is related to the reduced elastic modulus by Eq. (7). Substituting the Poisson ratio of 0.2 for AlN,[32] the elastic modulus and Poisson ratio for diamond indenter, and with the average reduced elastic modulus into the equation, the average elastic modulus of the AlN thin films can be estimated to be about 307 GPa.

V. SUMMARY

Smooth piezoelectric AlN thin films were grown on the sapphire and silicon substrates by the dc reactive magnetron
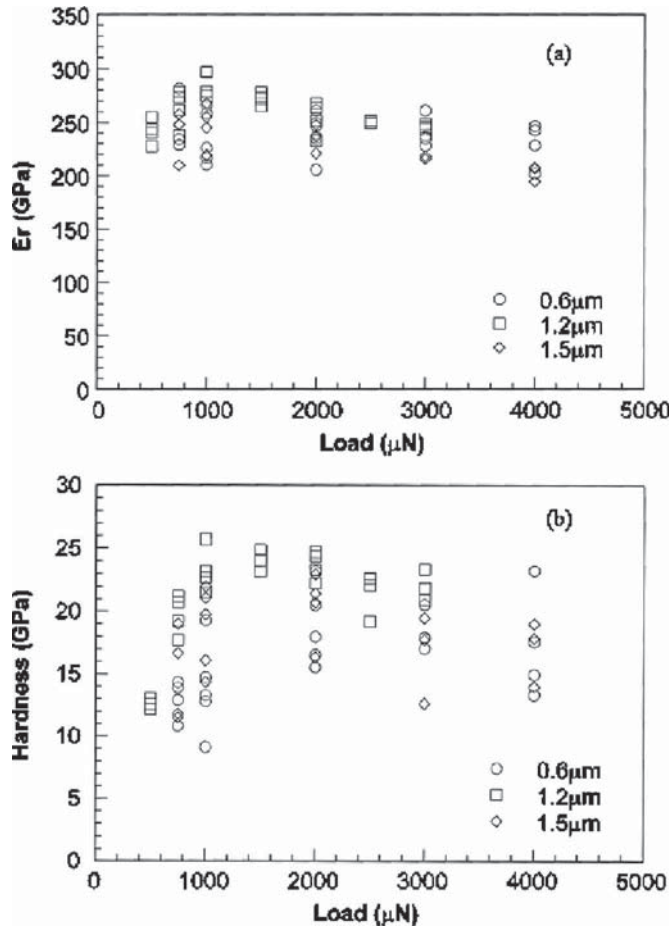
FIG. 11. (a) Reduced elastic modulus and (b) hardness of the AlN thin films with different maximum loads at room temperature.

341.2 GPa. The results obtained from the experiments are in good agreement with those for bulk AlN crystals.

sputtering. SEM and XRD characterization results show that the films show highly c-axis orientation. Single beam laser interferometer system was used to measure the effective piezoelectric coefficient of the AlN thin film deposited on sapphire substrate. The effective and true piezoelectric strain coefficients d_{33eff} and d_{33} of the AlN thin films are 2.9 and 4.17 pm/V, respectively. Thin film composite resonators have also been fabricated on silicon substrate for the characterization of electromechanical properties. The S-parameter (S_{11}) spectrum of the composite resonator was first measured at a wide frequency range and converted into electric impedance spectrum. Using the space of two adjacent parallel resonance frequencies at the first normal and transition regions in the electric impedance, the density and acoustic velocity of the AlN thin film were calculated to have values of 3187.3 kg/m^3 and 10631 m/s, respectively. Consequently the stiffened elastic modulus c^D of the AlN film is

[1] P. M. Martin, Thin Solid Films **379**, 253 (2000).
[2] Q. M. Zhang, W. Y. Pan, and L. E. Cross, J. Appl. Phys. **63**, 2492 (1988).
[3] S. Lin, IEEE Trans. Ultrason. Ferroelectr. Freq. Control **51**, 1280 (2004).
[4] E. K. Sittig, IEEE Trans. Sonics Ultrason. **16**, 2 (1969).
[5] A. H. Meitzler and E. K. Sittig, J. Appl. Phys. **40**, 4341 (1969).
[6] Y. Zhang, Z. Wang, and J. D. N. Cheeke, IEEE Trans. Ultrason. Ferroelectr. Freq. Control **50**, 321, (2003).
[7] A. L. Kholkin, Ch. Wuthrich, D. V. Taylor, and N. Setter, Rev. Sci. Instrum. **67**, 1935 (1996).
[8] K. Lefki and J. M. Dormans, J. Appl. Phys. **76**, 1764 (1994).
[9] G.-T. Park, J.-J. Choi, J. Ryu, H. Fan, and H.-E. Kim, Appl. Phys. Lett. **80**, 4606 (2002).
[10] ANSI/IEEE Standard No. 176-1987, *IEEE Standard on Piezoelectricity* (IEEE, New York, 1987).
[11] M. Onoe, H. F. Tiersten, and A. H. Meitzler, J. Acoust. Soc. Am. **35**, 36 (1963).
[12] D. Berlincourt, *Piezoelectric Crystals and Ceramics, in Ultrasonic Transducer Materials* (Plenum, New York, 1971), pp. 63–124.
[13] Q. Chen and Q.-M. Wang, Appl. Phys. Lett. **86**, 022904 (2005).
[14] Q. Chen, T. Shun, and Q.-M. Wang, Proceedings of the 2004 IEEE International Frequency Control Symposium and Exposition (unpublished), pp. 11–17.
[15] X. Li and B. Bhushan, Mater. Charact. **48**, 11 (2002).
[16] W. D. Nix, Mater. Sci. Eng., A **234–236**, 37 (1997).
[17] J. R. Withers and D. E. Aston, Adv. Colloid Interface Sci. **120**, 57 (2006).
[18] Q.-M. Wang, Y. Ding, Q. Chen, M. Zhao, and J. Cheng, Appl. Phys. Lett. **86**, 162903 (2005).
[19] I. N. Sneddon, Int. J. Eng. Sci. **3**, 47 (1965).
[20] W. C. Oliver and G. M. Phar, J. Mater. Res. **7**, 1564 (1992).
[21] K. Geng, F. Yang, T. Druffel, and E. A. Grulke, Polymer **46**, 11768 (2005).
[22] J. S. Jourdan, S. J. Cruchon-Dupeyrat, Y. Huan, P. K. Kuo, and G. Y. Liu, Langmuir **15**, 6495 (1999).
[23] Y. Sun, B. Akhremitchev, and G. C. Walker, Langmuir **20**, 5837 (2004).
[24] M. Cekada and P. Panhan, Vacuum **61**, 235 (2001).
[25] M.-A. Dubois, P. Muralt, and V. Plessky, Proc.-IEEE Ultrason. Symp. **2**, 907 (1999).
[26] M.-A. Dubois and P. Muralt, Appl. Phys. Lett. **74**, 3032 (1999).
[27] K. Lefki and G. J. M. Dormans, J. Appl. Phys. **76**, 1764 (1994).
[28] I. L. Guy, S. Muensit, and E. M. Goldys, Appl. Phys. Lett. **75**, 4133 (1999).
[29] K. Tsubouchi and N. Mikoshiba, IEEE Trans. Sonics Ultrason. **SU-32**, 634 (1985).
[30] C. M. Lueng, H. L. W. Chan, C. Surya, and C. L. Choy, J. Appl. Phys. **88**, 5360 (2000).
[31] G. Bu, D. Ciplys, M. Shur, L. J. Schowalter, S. Schujman, and R. G. Aska, Appl. Phys. Lett. **84**, 4611 (2004).
[32] I. Yonenaga, T. Shima, and M. H. F. Sluiter, Jpn. J. Appl. Phys., Part 1, **41**, 4620 (2002).